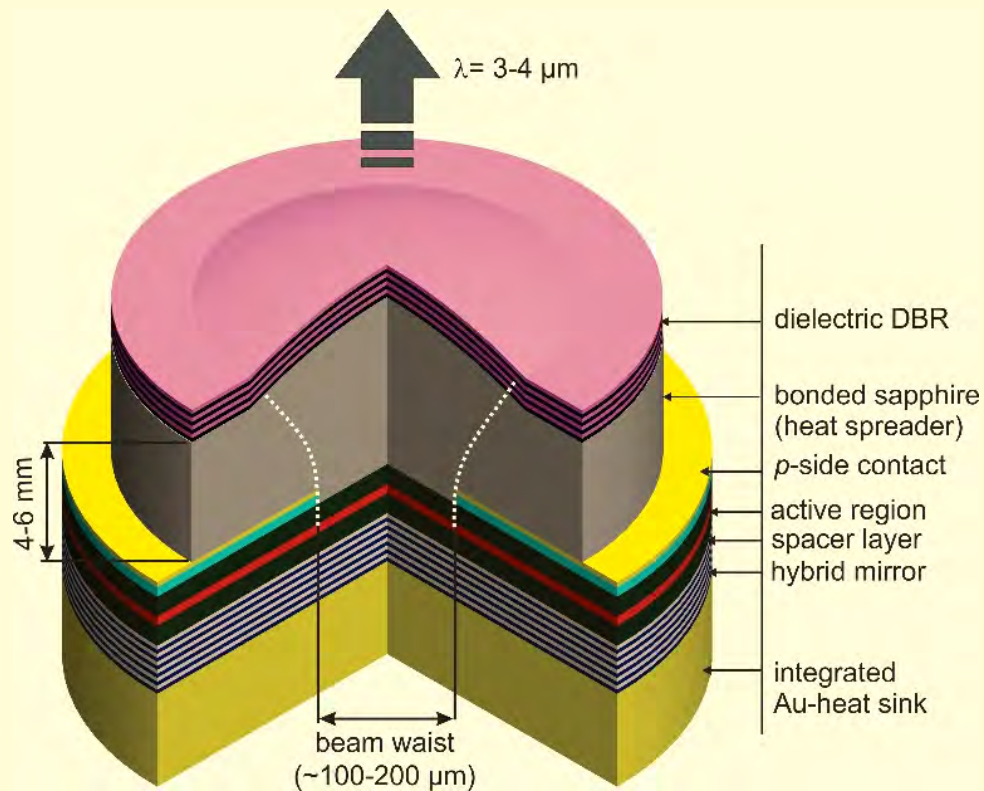


Research in Optoelectronics (A)



2019 Reprints of
Professor Larry A. Coldren
and Collaborators

ECE Technical Report 20-01
Department of Electrical & Computer Engineering
University of California, Santa Barbara

Research in Optoelectronics (A)

Reprints published in 2019

by

Professor Larry A. Coldren

and Collaborators

Published as

Technical Report # ECE 20-01

of

The Department of Electrical & Computer Engineering

The University of California

Santa Barbara, CA 93106

Phone: (805) 893-4486

Fax: (805) 893-4500

E-mail: coldren@ece.ucsb.edu

<http://www.ece.ucsb.edu/Faculty/Coldren/>

III. Collaborating Students

H. Zhao	UCSB, Klamkin Group
B. Song	UCSB, Klamkin Group
Y. Liu	UCSB, Klamkin Group
F. Sang	UCSB, Klamkin Group
S.T.S. Brunelli	UCSB, Klamkin Group
J. Fridlander	UCSB, Klamkin Group
V. Rosborough	UCSB, Klamkin Group
K. T. Cook	UC Berkeley
J. Qi	UC Berkeley
B. Paul	Ohio State University
S. M. N. Hasan	Ohio State University
J. Tang	University of Ottawa

I. Photonic Integrated Circuits

A. Reviews and Overviews

L.A. Coldren, "Technology Transfer at UCSB (for successful startups)" *Proc. IEEE Photonics Conference (IPC)*, paper MG 3.1, San Antonio, TX (September, 2019) INVITED PAPER 1

B. GaSb-based PICs

S. Arafin, Anthony P. McFadden, Banaful Paul, Syed M. N. Hasan, James A. Gupta, Chris J. Palmstrøm, and Larry A. Coldren, "Study of wet and dry etching processes for antimonide-based photonic ICs," *Opt. Mater. Express*, vol. 9, no 4, pp. 1786-1794 (April, 2019) 16

S. Arafin, L. A. Coldren and S. Dwivedi, "Design of High-Power Electrically-Pumped VECSELs for the 3–4 μm Wavelength Range," *Proc. 2019 IEEE Research and Applications of Photonics in Defense Conference (RAPID)*, Miramar Beach, FL, USA, paper WA1-5 (August, 2019). 25

C. PICs for Free-Space Links and LIDAR

H. Zhao, S. Pinna, F. Sang, STS Brunelli, L. A. Coldren, and J. Klamkin, "High-Power Indium Phosphide Photonic Integrated Circuit Platform," *Proc. 77th Device Research Conference (DRC)*, Ann Arbor, MI, paper III-B-2 (June, 2019) 28

B. Isaac, Y. Liu, S. Pinna, L. A. Coldren, and J. Klamkin, "Waveguide Uni-Traveling-Carrier Photodiodes for mmW Signal Generation: Space-Charge Impedance and Efficiency Limitations" *Proc. 77th Device Research Conference (DRC)*, Ann Arbor, MI, paper P-45 (June, 2019) 30

M. Stephen, J. Klamkin, L. A. Coldren, J. Fridlander, V. Rosborough, F. Sang, J. R. Chen, K. Numata, and R. Kawa, "Integrated Micro-Photonics for Remote Earth Science Sensing (Impress) Lidar," *Proc. IGARSS 2019 - 2019 IEEE International Geoscience and Remote Sensing Symposium*, Yokohama, Japan, pp. 4853-4856 (July, 2019). 32

S. Pinna, S. Dwivedi, L. A. Coldren, C. Schow, and J. Klamkin, "Power Optimization for Datacenter Optical Transmitters," in *OSA Advanced Photonics Congress (AP) 2019 (IPR, Networks, NOMA, SPPCom, PVLED)*, OSA Technical Digest (Optical Society of America), paper NeM4D.2 (July-Aug., 2019). 36

V. Rosborough, F. Sang, J. Fridlander, H. Zhao, B. Song, S. T. Š. Brunelli, J. R. Chen, M. A. Stephen, L. Coldren, and J. Klamkin, "Monolithic Integration of Widely-Tunable DBR and DFB Lasers with One-Step Grating Formation," in *OSA Advanced Photonics Congress (AP) 2019 (IPR, Networks, NOMA, SPPCom, PVLED)*, OSA Technical Digest (Optical Society of America), paper IM2A.5 (July-Aug., 2019). 38

H. Zhao, S. Pinna, F. Sang, S. T. Š. Brunelli, L. A. Coldren and J. Klamkin, "High Power Indium Phosphide Photonic Integrated Circuit for Pulse Position Modulation Free Space Optical Communications," *Proc. 2019 IEEE International Conference on Space Optical Systems and Applications (ICSOS)*, Portland, OR, USA, paper S11.1 (October, 2019) 40

B. J. Isaac, B. Song, S. Pinna, L. A. Coldren and J. Klamkin, "Indium Phosphide Photonic Integrated Circuit Transceiver for FMCW LiDAR," in *IEEE Journal of Selected Topics in Quantum Electronics*, vol. 25, no. 6, Art no. 8000107 (Nov.-Dec. 2019) 43

H. Zhao, S. Pinna, F. Sang, B. Song, STS Brunelli, L. A. Coldren, and J. Klamkin, "High-Power Indium Phosphide Photonic Integrated Circuits," in *IEEE Journal of Selected Topics in Quantum Electronics*, vol. 25, no. 6, Art no. 4500410 (Nov.-Dec. 2019). INVITED PAPER 50

D. Signal Processing

J. Tang, M. Li, R. S. Guzzon, L. A. Coldren and J. Yao, "Wideband and Continuously Tunable Microwave Photonic Phase Shifter Based on an Active InP/InGaAsP Microring Resonator," *Proc. 2019 International Topical Meeting on Microwave Photonics (MWP)*, Ottawa, ON, Canada, pp. 1-4 (October, 2019) 60

II. Widely-Tunable VCSELs

Kevin T. Cook, Pengfei Qiao, Jipeng Qi, Larry A. Coldren, and Connie J. Chang-Hasnain, "Resonant-antiresonant coupled cavity VCSELs," *Opt. Express*, vol. 27, no 3, pp. 1798-1807 (February, 2019) 63

I. Photonic Integrated Circuits

A. Reviews and Overviews



Technology Transfer at UC-Santa Barbara [for successful start-ups]



Larry A. Coldren
ECE & Materials, UC-Santa Barbara



Technology &
Industry Alliances

Start-Ups: Some Context

UC Santa Barbara

- University technology is early stage (embryonic, even)
 - A lot of risk in developing products
- Established companies prefer relatively “de-risked” opportunities
 - Challenging to find interested established companies if technology needs significant investment
- Startups, formed specifically to further develop one key technology, can fill that gap very effectively – or continue to expand into a mature, long-term company

And while they are doing it....

- Create jobs
- Attract funding to region
- And if they are lucky...
become the next Google??





- 1989: Digital Instruments (atomic force microscope), acquired by Veeco Instruments (now Bruker Instruments)
 - Digital Instruments' spin-off, Asylum Research, formed in 1999
- 1989: *Computer Motion, Inc (robotic surgery) , acquired by Intuitive Surgical
- 1990: Uniax (organic LEDs), acquired by DuPont
- 1992: Optical Concepts (VCSELs), acquired by W.L. Gore
- 1994: *Software.Com/Openwave (Internet messaging) → Sonos
- 1995: Terabit Technologies (InGaAs/Si APDs), acquired by Ciena
- 1996: *Indigo Systems (IR imaging)
- 1996: Nitres (GaN LED lighting), acquired by Cree
- 1998: Agility (widely-tunable lasers), acquired by JDS Uniphase
- 1998: Expertcity/Citrix Online
- 2000: *Calient Networks (photonic switching), acquired by Suzhou Chunxing Prec. Mech.
- 2003: Aeries Photonics (VCSELs, SBIRs, IR imaging, etc.), acquired by FLIR
- 2008: Aurion (InGaAsP/SOI—Int. Silicon Photonics), acquired by Juniper Networks
- 2008: *Freedom Photonics (1300nm tunables, SBIRs, etc.)



All of these companies maintain a footprint in Santa Barbara.
 Many of these have early entrepreneurs who are still actively building second- and third-generation start-up companies from technology developed at UCSB.

*Not a direct spin out of UCSB technology

Entrepreneurial Engineering at UCSB

+ 230 companies started from campus

Average of 14 companies formed every year



UC SANTA BARBARA
College of Engineering

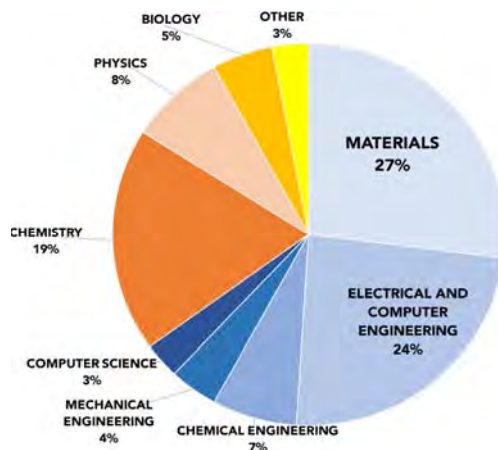


- According to recent research, UCSB tech start-ups raised \$53M in 2017 and \$124M in 2018 (to-date) from angels and VCs.
- Recent Successful Startup Exits:
 - August, 2016: Aurrion – Acquired by Juniper Systems (\$165M)
 - July, 2016: ShadowMaps – Acquired by Uber
 - October, 2016: CytomX IPO (currently trading at approx. \$23)
 - February, 2014: Inogen IPO (currently trading at approx. \$247)
 - December, 2014: Eucalyptus – Acquired by Hewlett Packard
 - December, 2012: Asylum Research – Acquired by Oxford Instruments (\$80M)
 - August, 2012 Sirigen – Acquired by Becton Dickinson (\$90M)



FY18 TIA Portfolio Activity for UCSB

IPC 2019



Invention Portfolio 90 New in FY18

- 664 Active Inventions
- 474 Active US Patents*
- *Inventions can be subject to more than one patent*
- 261 Active Foreign Patents

License Agreements

37 New in FY18

- 134 Active

65% of New Invention Portfolio Involves CoE

Typical Situation (small funding levels):

- **Industry request (Existing large company)**
 - Royalty-free license to all inventions generated in project
- **University position**
 - Depending upon funding level, provide right of first refusal to obtain a non-exclusive, royalty-bearing license
 - Filing and maintenance costs to be born by licensee and fair and reasonable royalties to be negotiated, based upon value of invention
 - Preferential exclusive licenses may also be negotiated at fair and reasonable terms; if not desired, non-exclusive licenses to other parties may be negotiated with up-front fees required

For larger funding levels (where all project costs are covered):

- **More favorable pre-negotiated IP terms can be obtained**

- **Move useful advances into the private sector**
 - Why not just publish and let existing companies select what they want?
 - Professional pride may inhibit process in companies
 - Start-up costs in companies compete with existing priorities
 - Inventors (from universities) more driven to make ideas succeed
 - Start-ups more willing to license IP, because they need protection
 - Start-ups may be best avenue to mature IP with Angel, VC or government funding. Then, companies can decide what to select (acquire) after start-up proves feasibility (or not)

- **Fulfills a primary role of a University**
 - Technology developed benefits society
 - Rewards faculty and student entrepreneurs (attracts/retains/supplies quality)
 - Provides resources to enable further teaching and research
 - (Indirectly→ SBIRs, gifts, etc.; supports university facility costs. A modest percentage of patent royalties are returned to departments)

- Keep a good lab notebook (regardless)
- Educate yourself in Entrepreneurism (TMP @ UCSB)
- When your viable idea for a high-demand product occurs:
 - Submit all University developed IP to University IP office (TIA)
 - Develop plan to create product: who are customers; how to market; what team is required; what resources are needed; timeline; how costly; how to finance
 - Find separate space/facility to work and develop new company IP
 - Look into finance options—SBIRs; Angel investors, friends and family, VCs
 - License University IP if desirable
 - Manage costs: e.g., outsource expensive fabrication costs
 - Select quality team members, and only those needed

Entrepreneurism:

UCSB Technology Management Program



New Venture Competition:
TMP's flagship entrepreneurial program



Established 2001

Campus-wide, year-long

Transformative Educational Experience

Strong Network of Mentors and Advisors

Track Record of Successful Startups

TMP Academic Programs:

- **Technology Management Certificate** (for current undergraduate students)
- **Graduate Program in Management Practice Certificate** (for current graduate students)
- **Master of Technology Management** (professional masters degree)
- **PhD in Technology Management**



Student Entrepreneur Success Stories



inogen

- Winner 2001 NVC
- 2014 IPO
- Market value \$2.5 B



APEEL SCIENCES

- Winner 2012 NVC
- \$70M+ capital raised



TrackR

- Winner 2009 NVC
- \$63M capital raised
- Revenue \$50M-\$100M

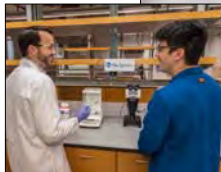


Sirigen

- Winner 2003 NVC
- Acquired by BD, 2012

Find separate space/facility:

CNSI Technology Incubator – Laboratory Resource for Startups



- Mission – Bring scientific and technological innovation into the **economy** and society
 - 900 sq. ft. of wet-lab / dry-lab space set aside for Incubator
 - Collaboration with UCSB I&E Ecosystem
- Eligibility
 - Active corporate licensees of UCSB intellectual property
 - Companies founded by UCSB faculty, staff, or students
 - Local pre-production community start-ups

Current residents

Milo Sensors

bioProtonics

MENTIUM

Loamli Therapeutic Devices

FLUENCY LEADING TECHNOLOGIES

NEXUS Photonics

Former members

NEXT

APEEL SCIENCES

(Incubator prize, Summer 2018)

Outsource expensive fabrication/testing:

UCSB Shared Facilities

Nanotech Labs



MRL Labs



47 Facilities
304 Instruments

Part of what makes UCSB - and Santa Barbara in general - a good place to start a company

Nanotech Facility Overview

UCSB

- ~12,000 sq. ft. of cleanroom space (class 1000, 100)
- Full set of nanofabrication tools for thin film patterning, deposition, etching, integration, modification, characterization, metrology
- ~\$50M of fabrication equipment (replacement cost)
- Operates as a highly accessible user facility
- Highly skilled staff for supporting process development, tool training, maintenance
- ~ \$6M/yr in yearly recharges. ~\$4M/yr from industrial use (\$3.5M small company)
- No State subsidy for the facility. Runs on recharges only.

Main corridor for access to 7 Bays/6 Chases



Bay 3
Class 1,000 - Deposition



Bay 6
Class 100 - Lithography



www.nanotech.ucsb.edu

UC SANTA BARBARA
engineering

Nanofabrication Equipment - Overview

The convergence of research and innovation.

- **Lithography**– Steppers (i-line(2) and DUV), EBL, Contact, Nanoimprint
- **Etching** – ICP(3), CAIBE, RIE(3), SiDRIE, vaporHF, XeF₂, CMP



ASML-DUV-248nm
Only 3 at Universities
Sub-200nm Full Wafers
Si-Photonics
Quantum Computing



JEOL 6300 EBL
Sub-10nm Patterning
<5nm Stitching errors
Full Wafers
THz electronics
Advanced Photonics



Panasonic ICP Etcher/Asher
Dielectrics, Metals, Semiconductors
Workhorse systems – often >18 Hrs/day
nm-scale control - reproducible

UCSB

UC SANTA BARBARA
engineering

A Proven State and National Resource:

The convergence of research and innovation.

Map of Institutions Served 2006-2018




- **Regional (CA) Reach**
 - ◆ 185 in state external industrial institutions (and 18 Academic)
 - ◆ Includes: Google, HP, Apple, Raytheon, Lockheed Martin, Cree, JDSU, Juniper Networks, Bruker, HRL, Teledyne, Northrop Grumman, Intel, KLA-Tencor, JPL, Tyco, Dupont, FLIR, Myriads of small and start-up companies
 - ◆ 46 SB/Goleta Area
- **National Reach**
 - ◆ 58 out-of-state External Industrial Institutions out of state
 - ◆ 41 External Academic Institutions out of state

UCSB

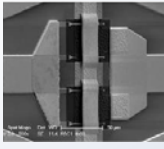
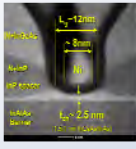
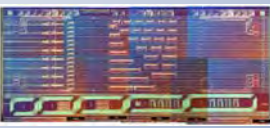
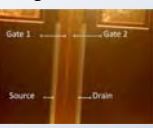
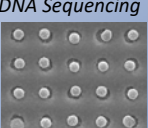
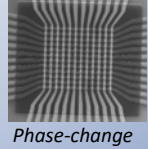
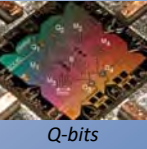
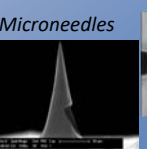
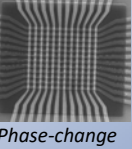
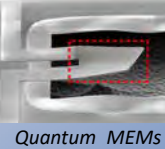
UC SANTA BARBARA engineering **105 Companies Over Last 2 Years**
 The convergence of research and innovation.

<p>Fluency Lighting Nexus Photonics Ultra-low Loss Technologies 3DCD Applied Materials Bruker Metrology Continental Advanced Lidar Solutions, Inc Corning Technology Center Cree Facebook Technologies, LLC FLIR Commercial Systems FLIR EOC Garmin International, Inc. General Atomics Google Inc. HP Labs Hughes Research Laboratories Infinera Juniper Networks KLA-Tencor Inc Lam Research Corporation Lockheed Martin, Missiles & Fire Control Raytheon Vision Systems Space Exploration Technology Corp. SRI International Technicolor HES Teledyne Scientific & Imaging The Aerospace Corporation Toyon Research Corporation 3D-Sensir Inc (Acqubit) AdTech Photonics Advanced Modular Systems</p>	<p>Advanced Nanostructures AdvR Aeonian Semiconductor Technology AISthesis Products, Inc. Angstrom Science Apic Corporation Applied Nano Applied Nanostructures, Inc Aptitude Medical Systems Inc Astrileux Corporation Asylum Research Atollo Engineering, LLC Ayar Labs Calient Networks CBrite Christian Gutleben Complete Genomics Inc. Crossbar Inc. Crystalline Mirror Solutions LLC Crystalline Mirrors (Vixar) Drinksavvy Inc. Duet Microelectronics ELR Systems LLC Freedom Photonics, LLC Genapsys Inc GenXComm Inc Ideal Power Inc Innovative Micro Technology Innovativelll-V.Solutions Laser Components DG Inc Laxense, Inc. Laxmi Therapeutic Devices Magic Leap</p>	<p>Milo Sensors Inc. Momentum Optics, LLC Nano Precision Medical Numerical Design, Inc. Omniome, Inc. Owl Biomedical Inc. Parthian Energy Pendar Technologies PiMEMS Inc. Praevium Research Promerus LLC QmagIQ RLC Solutions Rodman Scientific Royole Corporation Sensor Creations SensorMatrix Sientra Inc Silicon Designs, Inc. Solar Junction Corporation Solution Deposition Systems Soraa Laser Diode, Inc Soraa, Inc. Spectradyne LLC SurForce Corporation TelAztec Terray Therapeutics Transphorm Tribogenics Ultima Genomics VoxelNano Westar Automation LLC Xerial Sciences Zephyr Photonics</p>
--	---	---

UCSB

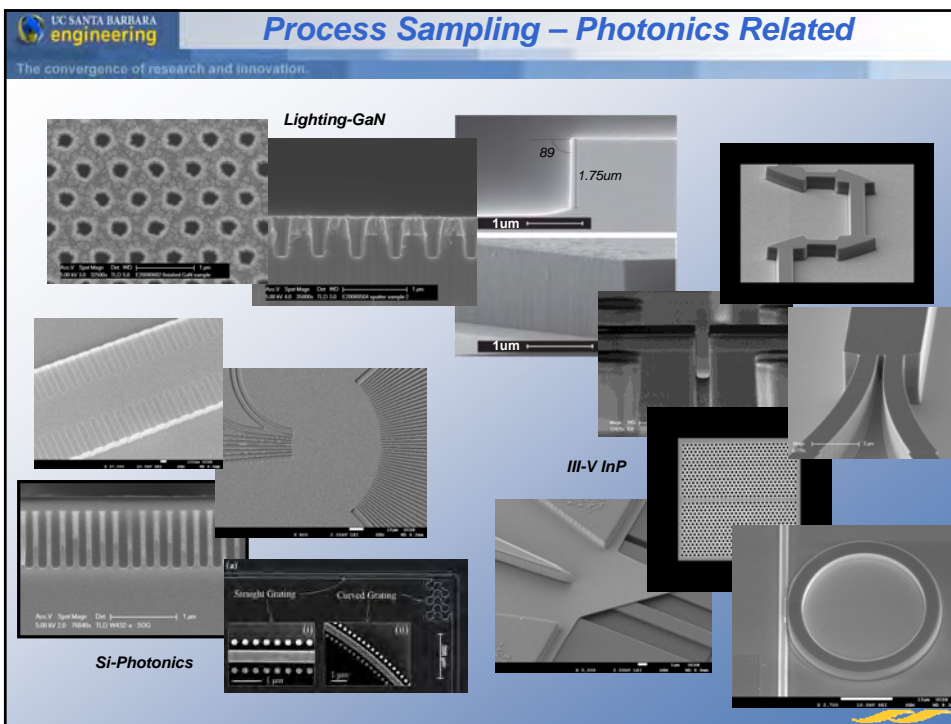
UC SANTA BARBARA engineering **Project Sampling from UCSB Nanofab Users**
 The convergence of research and innovation.

Electronics, Photonics, MEMs, Microfluidics, Materials, Physics

<p>GaN HEMTs</p> 	<p>III-V MOS</p> 	<p>LEDs for Lighting</p> 	<p>Si photonics Heterogeneous III-V Si Integration</p> 
<p>Organic FETs</p> 	<p>Nitride-based lasers</p> 	<p>VCSELS</p> 	<p>DNA Sequencing</p> 
<p>THz transistors</p> 	<p>InP-Photonic ICs</p> 	<p>Q-bits</p> 	<p>Microneedles</p> 
<p>Phase-change memory</p> 	<p>Quantum MEMS</p> 	<p>Micro-Nanofluidics</p> 	

Solid-State Lighting, Photovoltaics, Thermoelectrics, Oxide Electronics

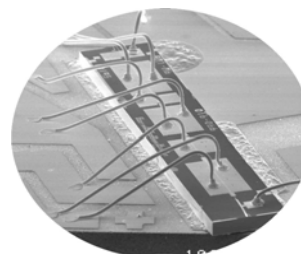
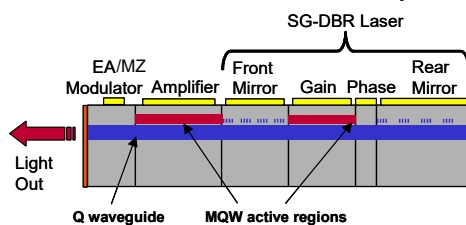
UCSB



Example 1:

Agility Communications (Acq. JDSU 2005 → Lumentum)

- Formed 1998 by Coldren students + Coldren; based on fundamental 1988 UCSB patent filing
- Widely-tunable (full C-band) sampled-grating-DBR lasers with integrated SOAs and modulators; use of off-set quantum-wells for active-passive



Advantages:

- smaller space
- lower cost
- lower power consumption
- high reliability



Agility's Unique Platform—2001-2005

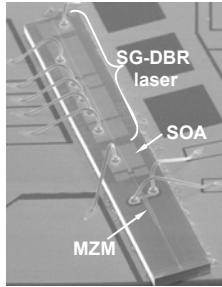
Integration Replaces Discretes



Laser Source



LN Modulator



Optical Amplifier



VOA

Higher Reliability, Smaller Size, and Lower Cost:

- Significant Part Count Reduction for DWDM
- Eliminates Multiple Packaging
- Single Chip Reliability
- Only Tunable Integration Platform in the Market

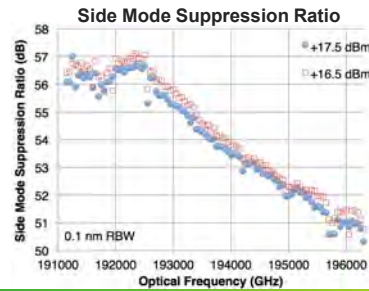
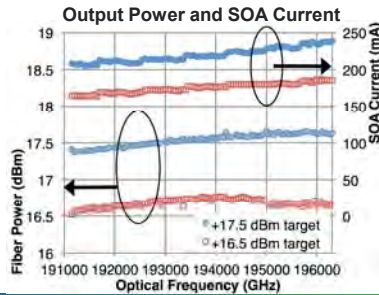
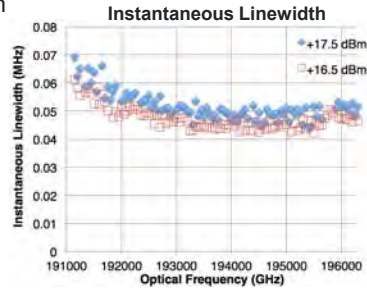
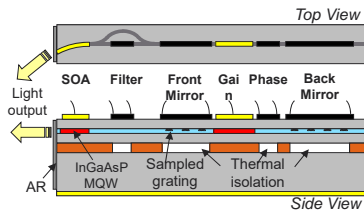
Tunable Tx/Rx Transponder with all control electronics primary product —2002→

Integrated MZM after 2004

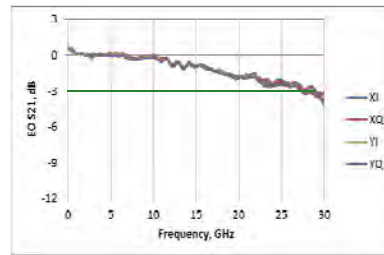
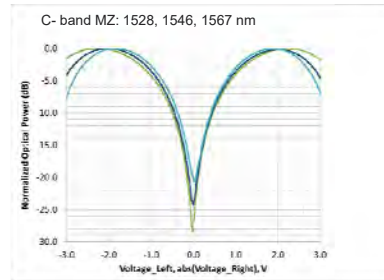
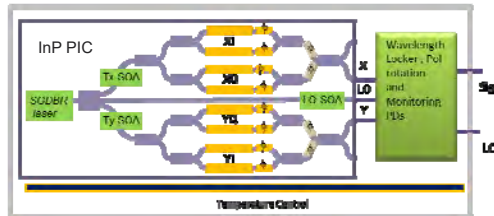


Narrow linewidth thermally-tuned SGDBR Laser—2015

- 70kHz linewidth and 50dB SMSR at +17dBm fiber power over 41nm range in C-band



C-band Tunable Integrated Coherent Transmitter PIC

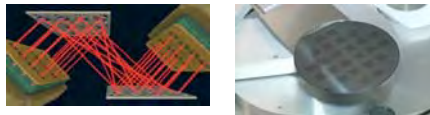
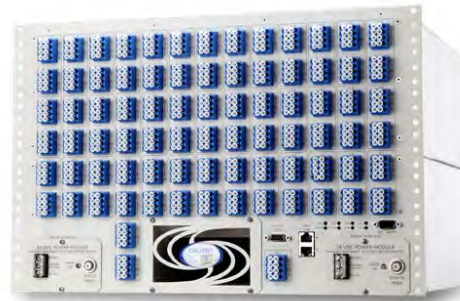


- Narrow Linewidth Sampled-Grating DBR laser
- Two quadrature Mach-Zehnder modulators
- High power LO output
- 3 SOAs
 - Independent power control for LO and each Tx polarization
 - VOAs
- InP PIC technology is employed for 32 Gbaud 100 and 200 Gb/s coherent pluggable modules

Example 2:

CALIENT's S-Series Optical Circuit Switch (OCS)

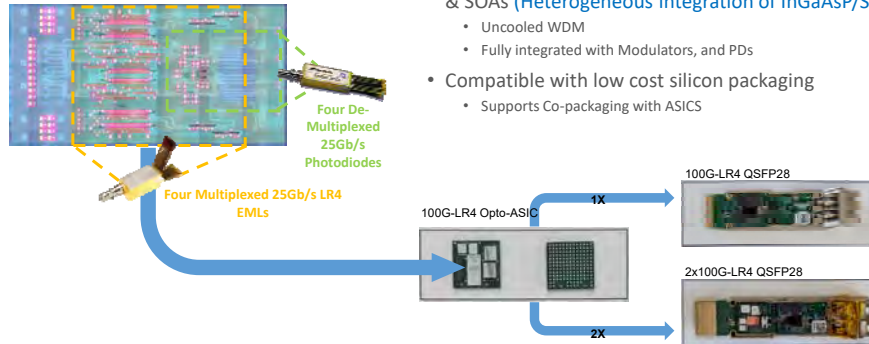
- **Up to 320 User Ports – 640 Single Mode Fiber Terminations**
 - 320x320, 160x160 options
- **10, 40, 100 Gbit/s per port and beyond**
- **25ms typical setup time (<50ms Max)**
- **Less than 30ns latency**
- **Ultra low power (<45w), small size (7RU)**
- **TL1, SNMP, OpenFlow, REST APIs**
- **Less than 3.0 dB Insertion Loss**



Founded by Bowers, et al, 2000
Acquired 2017, Suzhou Chunxing Prec. Mech.

Example 3:

Aurion - Fully integrated Silicon Photonics



- Founded by Alexander Fang and John Bowers out of UCSB in 2008
- Acquired by Juniper Networks – 2016
- The Only Silicon Photonics Platform with WDM Lasers & SOAs (Heterogeneous integration of InGaAsP/SOI)
 - Uncooled WDM
 - Fully integrated with Modulators, and PDs
- Compatible with low cost silicon packaging
 - Supports Co-packaging with ASICs

Aurion - Photonic Integrated Circuits (PICs)

• Leveraging the economies of scale pioneered by the silicon industry

- Photonic Integrated Circuit (PIC) fabrication leverages silicon design, process, test, package, and foundry infrastructure for complete photonic systems
- **Impact:** Fundamental and permanent improvements in cost per bit-per-second

• Uncooled WDM technology

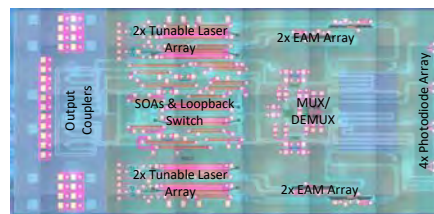
- No TEC required to operate over temperature
- Integrated micro heaters keep wavelength sensitive components tuned to the wavelength grid
- **Impact:** Higher capacities for networking interfaces

• Packaged like an ASIC

- Packaged along side other ASICs on the same substrate
- **Impact:** Greater flexibility in how bandwidth carried on light is processed inside the electronic portions of networking systems.

• ASIC like Reliability

- Single-chip, solid state devices vs discrete components
- **Impact:** Photonics that scale with the system



PIC stats

- 100Gb/s LR4 compliant
- Area = 34 mm²
- 67 photonic components interconnected with waveguides
- Many components contain subcomponents (laser = 8)



Examples 4 & 5:

GaN Start-ups from UCSB

- **Case Study 1: 1996—2000 Nitres (LED)**
 - Prof. Mishra & DenBaars start Nitres Inc.-GaN LED and FET company in U.S.-Acquired by CREE Inc.
 - LED lightbulbs commercialized
- **Case Study 2: 2013→ SLD Laser**
 - Prof. Nakamura, Speck, DenBaars, et al spin-out GaN laser leader SLD Laser (from Soraa formed in 2008).
 - LaserLight commercialized
- **Case Study 3-Transphorm**
 - Prof. Mishra spins-out power switching company
 - GaN based Power supplies commercialized



SSLEEC Solid State Lighting and Energy Electronics Center
UNIVERSITY OF CALIFORNIA, SANTA BARBARA



Cree, Inc. to Acquire Nitres, Inc., a Leader in Nitride Semiconductor Device Development; Company to Launch Solid State Lighting Subsidiary

Apr 11, 2000, 01:00 ET from [Cree, Inc.](#)

DURHAM, N.C., April 11 /PRNewswire/ -- Cree, Inc. (Nasdaq: Cree), the world leader in the development and manufacture of semiconductor materials and electronic devices made from silicon carbide (SiC), today announced it has signed a definitive agreement to acquire privately held Nitres, Inc., a leader in research and development of nitride-based semiconductor devices. Under the terms of the agreement, Cree will acquire all of the outstanding and vested shares of Nitres stock in exchange for approximately 1.5 million shares

Nitres founded in 1996 by DenBaars and Mishra



SSLEEC Solid State Lighting and Energy Electronics Center
UNIVERSITY OF CALIFORNIA, SANTA BARBARA





SLDLASER

LASERLIGHT: THE NEXT GEN SSL SOURCE

- Low Luminance
- Droop/Auger
- Safe

- High Luminance
- >10k brighter vs LED
- >20X power per chip
- Not Safe

- High Luminance
- 100X brighter vs LED
- 500lm from 300um
- Safe

- Incoherent emission provides safety & regulatory acceptance versus direct LD **(Sora continues in the first two boxes)**



SSLEEC Solid State Lighting and Energy Electronics Center
UNIVERSITY OF CALIFORNIA, SANTA BARBARA



SLDLASER



“Laser diodes are lighting’s future.”

Nobel Laureate Physics & SLD Laser Co-Founder
Shuji Nakamura

30



SSLEEC Solid State Lighting and Energy Electronics Center
UNIVERSITY OF CALIFORNIA, SANTA BARBARA



I. Photonic Integrated Circuits

B. GaSb-based PICs



Study of wet and dry etching processes for antimonide-based photonic ICs

SHAMSUL ARAFIN,^{1,2,*} ANTHONY P. MCFADDEN,³ BANAFUL PAUL,² SYED M. N. HASAN,² JAMES A. GUPTA,⁴ CHRIS J. PALMSTRØM,^{1,3} AND LARRY A. COLDREN^{1,3}

¹Department of Electrical and Computer Engineering, University of California at Santa Barbara, Santa Barbara, CA, USA

²Department of Electrical and Computer Engineering, The Ohio State University, Columbus, OH, USA

³Department of Materials, University of California at Santa Barbara, Santa Barbara, CA, USA

⁴National Research Council of Canada, Ottawa, ON, Canada

*arafin.1@osu.edu

Abstract: We report on the dry etch process parameters and the associated etch rates for target and mask materials, as well as surface roughness in an inductively coupled plasma (ICP) for the (AlGaIn)(AsSb)-compounds. The essential chemistry is based on Cl₂ with the addition of N₂ for sidewall passivation. The optimized ICP etch process is capable of producing high aspect ratio structures with smooth sidewalls. *In situ* reflectance monitoring with a 670-nm-wavelength laser was used to enable stop-etching at a material interface with high accuracy. Given the additional need for highly selective wet chemical etchants in the fabrication of GaSb based electronic and optoelectronic devices, an extensive investigation was also performed to examine numerous etch solutions. These etchants were listed with etch rates, selectivities, and surface roughness in order to validate their suitability for intended applications. Despite the frequent use of GaSb or InAsSb materials for etch stop layers against each other, devices where their unique type-II broken bandgap alignment is undesired require new selective wet etchants between GaSb and AlGaAsSb with good selectivity. All of the wet chemical and dry etching processes described here were optimized using an *n*-type GaSb substrate.

© 2019 Optical Society of America under the terms of the [OSA Open Access Publishing Agreement](#)

1. Introduction

Dry and wet etch processes are important and widely used for the fabrication of electronic and optoelectronic devices. Recently, there has been an increasing interest in many micro and nanoscale short-wave (SW-) and mid-wave (MW) infrared (IR) devices including transistors [1,2], photodiodes [3], light emitting diodes (LEDs) [4] and diode lasers [5] due to a wide range of emerging applications. Development of these devices at this wavelength regime requires the novel (AlGaIn)(AsSb) material system on GaSb substrates.

As opposed to III-Vs such as phosphides and arsenides, antimonide materials exhibit a few unusual etching behaviors such as undesired weak etching by commonly used developers with an etch rate of up to 0.6 nm/sec and very fast oxidation rate with atmospheric oxygen. It is also observed that hydrofluoric acid (HF) etches plasma-exposed antimonides unlike other III-Vs. Moreover, GaSb and its alloys show poor selectivities in commonly used wet and dry etchants that are typical in other III-V's device processing. Due to the strong and fast oxidation, Al-containing materials are not useable as etch-stop layers [6].

As a standard practice, for fabricating many optoelectronic devices including widely-tunable lasers, e.g. sampled-grating distributed-Bragg-reflector (SG-DBR) [7] and vertical-cavity surface-emitting lasers (VCSELs) [8], one usually uses etch-stop layers in order to control the etch depth with high accuracy of nanometer order. In such a way, it is possible to selectively remove the desired materials against another layer. In the case of widely-tunable

lasers, leading to photonic ICs (PICs) where active and passive regions are defined by selective wet chemical etching, multi-quantum well (MQW) regions are selectively removed from the top of the waveguide layer, defining low-loss passive waveguides [9]. This is usually done by the wet etch with an etch stop layer, since the wet etch makes no intrinsic damage in the laser structure. Not only this, a good wet etch process is also needed to create smooth surfaces and to etch to the correct depth to prevent exposure of the Al-containing layers, which would make regrowth difficult because of the difficulty in removing Al_2O_3 . Therefore, developing viable etch processes to make PIC compatible widely-tunable lasers in the GaSb-based materials, is of utmost importance.

For antimonide-based SG-DBR lasers, one has to find a good etch-stop layer underneath the MQW region. A lattice-matched InAsSb or InAs layer could be a good choice [10]. However, insertion of such a thin layer of InAsSb under the MQW region introduces a type-II band alignment in the structure, prohibiting a good flow of carriers into the well. Therefore, developing a dry etch process is extremely important so that the etch can be stopped on a material change using an optical etch-stop monitor, which uses the different index or bandgap properties of the stopping layer rather than its chemical properties.

Despite the fact that dry etching performed by ionized gases is almost always anisotropic and leaves smooth surfaces, it always creates some damages (leading to non-radiative recombination centers) on the etched surface and its underlying layers to a certain depth [11]. Having an understanding on the damage depth leads us to calculate the ionization energy. In this work, we used an inductively-coupled-plasma (ICP) reactive-ion-etching (RIE) which can produce a high density of reactive etching species at relatively low ion energy for low damage.

For the GaSb-based PICs, a surface-ridge waveguide will be required to connect the lasers, amplifiers, modulators and other photonic components together monolithically. The surface-ridge waveguide has a good current confinement, low-loss for single mode waveguides, which makes it uniquely suitable for lasers [12]. In GaSb-based PICs, quaternary AlGaAsSb with 50% or higher aluminium compositions could be used as a top cladding layer. In order to make a low-loss surface ridge waveguide, it is extremely important to find and optimize a dry etching recipe. The optimization of the process is focused on the sidewall verticality, surface smoothness and flat bottom in the etched profile.

There are a few studies that report only wet etch processes for antimonide materials [10,13–15]. However, the etchant lists presented in these studies are not complete because of the lack of information on a few useful wet and dry etchants and their suitability, etch stop layers except InAsSb against GaSb and etching of quaternary alloys. As a result, developing robust processes for widely tunable lasers and PICs by relying on these studies will not be possible, requiring a more systematic and thorough study.

Despite of the frequent use of lattice-matched InAsSb as an etch stop layer, its use in SG-DBR laser is not appropriate due to the type-II band alignment with GaSb. This forces to explore alternative etch-stop materials. In this paper, we performed detailed study not only on several unreported but useful wet etchants but also on dry etching with real-time, *in situ* laser etch depth monitoring and the corresponding etch results are summarized. In fact, our etching efforts were extended from binary to quaternary and even quaternaries alloys, their etching rates, selectivities as well as usability. Finally, the GaSb substrate removal process is described. The comprehensive detailing on the selective dry and wet etching for antimonides and its alloys will be beneficial for the fabrication of next-generation high-quality optoelectronic and electronic devices.

2. Experimental procedure

2.1 Sample preparation

To study and develop the dry and wet etch processes, we used four different samples with epistacks on GaSb:Te substrates grown by molecular beam epitaxy. Figure 1 shows the

schematic of the epilayers of the etching test structure used in this dry and wet etching study. The samples with Al-containing layers were covered with a 8-10 nm GaSb cap layer to prevent oxidation.

Standard photolithography was used to define the arbitrary patterns in the photoresist. In all of the wet etching tests, photoresist as etch masks were used. In cases of dry etching, especially when surface-ridge waveguides were defined, a 100-nm layer of SiO₂ is deposited via plasma-enhanced chemical vapor deposition on the as-grown sample at first. The lithographically-defined arbitrary patterns were then transferred to the SiO₂ by a CF₄/CHF₃/O₂ ICP-RIE etch. Finally, the photoresist was removed by the appropriate solvents in an ultrasonic bath. The target antimonide materials were then etched with SiO₂ as an etch mask. Note that the etch depth of the target materials was measured using a Dektak profilometer.

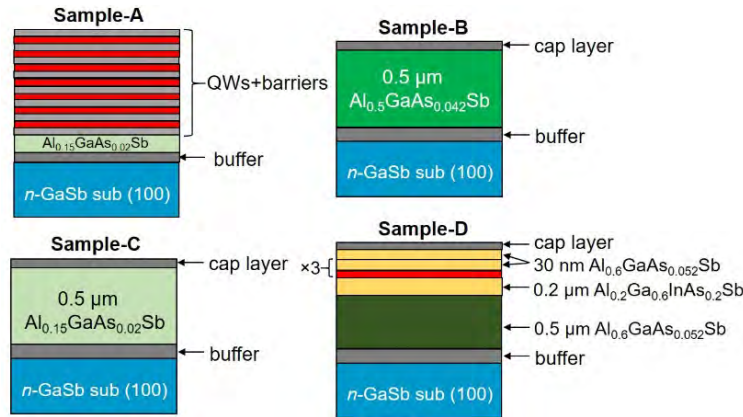


Fig. 1. Schematics of different test samples with epilayers used in this dry and wet etching study.

While processing InP-based lasers, the surface-ridge waveguide needs to be aligned to the $\langle 011 \rangle$ crystal direction of InP, because the top InP cladding etch is normally finished with an HCl-based crystallographic wet etch [16]. It is extremely important to investigate whether a similar behavior is applicable for the GaSb-based material system. Considering this, a mask was designed with narrow stripes at different angles. Figure 2 shows the microscope images of the 5 μm wide patterns obtained after photolithography using image reversal photoresists on a 100 nm blanket SiO₂ layer.

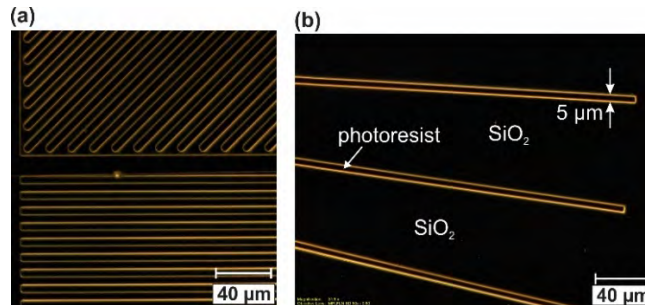


Fig. 2. Microscope images of the test samples with 5- μm surface ridges obtained after development and ready for dry etching in order to transfer the patterns into the hard mask.

Surface-ridge profiles obtained in this study involved first applying the Ti/Au metal stack over the entire epi-surface, and then performing a lithographic step to protect the metal where ridges were desired, followed by an etch step to remove the metal layers everywhere except

on the ridge tops to be. The photoresist/Ti/Au was then used as a mask for the ridge etching with Cl_2/N_2 chemistry using ICP-RIE.

2.2 Preparation of etch solutions

The preparation methods used in this wet etching study is different from the techniques described in ref [10]. The “Transene’s” premix solutions were often used in order to obtain consistent etch results. Such premixes are also easier to deal with since one does not need to mix up solid crystals with water every time prior to etching. Some of the premixes used in this study were as follows:

1. The tartaric acid-based premix is called “Rochelle” etch solution. This is 15 g of $\text{C}_4\text{H}_4\text{KNaO}_6$ crystals, dissolved in 200 ml of DI- H_2O , similar to ref [10]. In order to perform etching using this premix, one has to just add HCl and H_2O_2 to match the solution [10].
2. The citric acid premix, similar to mentioned in ref [10], is also used and it is better than mixing a supersaturated solution.
3. Sirtl etch is a mixture of HF and CrO_3 in DI water. This premix was also used in this study at two different dilutions, i.e., 1:5 = Sirtl: H_2O and 1:100 = Sirtl: H_2O .

2.3 Etch reactor with etch depth monitor

A Cl_2/N_2 ICP-RIE was used for dry etching performed in this study. The ICP has a laser monitor installed for getting real-time data during etching. Using this *in situ* etch monitoring system, one can observe the oscillation fringes, primarily between the surface and the first interface, and stop the etch exactly at the point needed. Later the etch rate and etch depth in real time enabling control of process termination were calculated using the 670 nm visible laser. Therefore, it is important to have the reliable material data. i.e.; refractive index and extinction coefficient for the material of interest at this wavelength. Based on the simulations of laser reflectance from a proposed sample, the etching process can be controlled to provide an endpoint depth precision within ± 10 nm.

3. Etching results and discussion

3.1 Dry etching

The etch parameters, and the associated etch results including etch-rate and etch-mask selectivity are listed in Table 1.

Table 1. ICP Dry Etching Parameter* and the Corresponding Results for Sample-B

RF bias (W)	ICP (W)	Pressure (Pa)	Gas flow (sccm)		Etch rate (nm/sec)	Selectivity vs SiO_2
			Cl_2	N_2		
75	900	0.2	20	10	8.7	8

*ICP plasma etching was performed using the Panasonic E640 system that is not capable of displaying induced self-DC bias voltage during the etching process and therefore it is not mentioned.

Although we have not obtained an accurate number for the ionization energy in our ICP system, the low RF chamber bias of 75 W suggests that it is relatively low. Importantly, by the addition of nitrogen to the etching RF plasma, our etch process resulted in smooth and less damaged surface. The presence of N_2 gas flow during the etching process helps to reduce the surface roughness and consequently smooth surface could be obtained. In addition, we did

not use argon in the gas chemistry in order to avoid physical etching. Therefore, the developed etch recipe based on Cl_2/N_2 is expected to work for even high Al content layers with good surface morphology. In fact, one of the major attributes of ICP is supposed to be the low ion damage imparted to the surface. Given the fact that the sample will be subsequently annealed in the MBE chamber prior to regrowth, we do not expect this damage to be an issue. Moreover, in a DBR laser, the etching is never over the MQW active region, so we did not pursue this matter further.

In order to obtain the etch rate, the etching was performed on etching test sample-B for three different times. After the dry etching, a smooth surface morphology on the etched surface was observed. Quaternary lattice-matched $\text{Al}_{0.5}\text{GaAs}_{0.04}\text{Sb}$ cladding layer was the layer of interest in this case. The measured data is fitted with the transfer matrix method in order to extract the refractive index and extinction coefficient values of the quaternary cladding layer. The reflectivity of a thin-film stack was continuously calculated as the stack was progressively thinned by etching from one side. Finally, the reflectivity vs. etch depth plot is used to determine end-points during etching.

Figure 3 shows the measured reflectivity data vs etch depth of the etching test structure. The intensity of the oscillations in the reflectivity data gradually increases as the material is being etched more; hinting that there is less absorption of light within the material of interest. The discontinuity at the end of the 500 nm lattice-matched $\text{Al}_{0.5}\text{GaAs}_{0.04}\text{Sb}$ layer is due to the transition to GaSb, and the slight mismatch may be due to the imaginary part being incorrect. The discontinuity seems to occur right at the layer transition according to the fits. So by eye, one can see the termination of each layer in the laser monitor plot itself, and one should be able to clearly see the first dip with lower extinction than the AlGaAsSb dips, and start counting from this point.

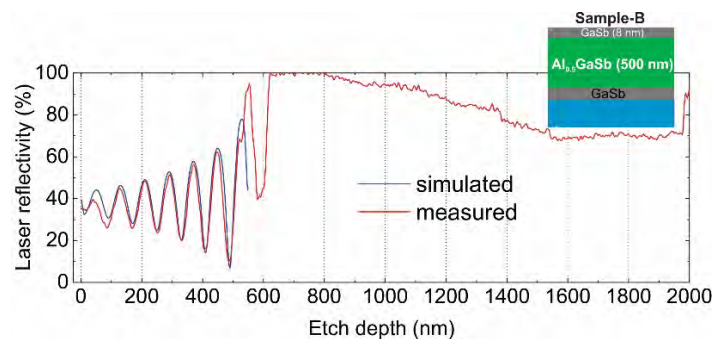


Fig. 3. Measured reflectivity data vs etch depth of etching test structure-B. Simulated laser monitor signal is superimposed to extract the refractive index and extinction coefficient values of the quaternary cladding layer.

Ridge processing was ended with a clean-up wet-etch to remove damage at the etched surface and the sidewalls. In other words, after the first waveguide dry etch, the surface ridge waveguide was then etched by an HCl-based isotropic wet etch. Figure 4 shows the ridge waveguide with a vertical etch profile and smooth surface morphology after clean-up etching. Rough sidewall, mostly due to a wavy SiO_2 mask edge defined by contact lithography, and possibly also enhanced by defects in epilayers, can also be seen here. In spite of the ridge-edge roughness in the waveguide, this is not a concern since a better lithography with a stepper should solve this issue. Although no undercut of mask was observed for dry etching, some undercut for the HCl wet etching was observed, which does selectively attack the AlGaAsSb epilayer. Most importantly, no crystallographic etching was observed for various orientations. A porous sidewall was noticed in the sample which could be attributed to the defects in epilayers. The defects revealed after the clean-up etch were not a surprise as there was some lattice mismatch in this AlGaAsSb epilayer. Figures 4(c) and 4(d) present the SEM

images of 50 μm wide ridges obtained after performing ICP etching using resist/Ti/Au as an etch mask. As may be noted, one of the potential drawbacks is the side-wall roughness that results from a replication of the roughness of the combined photoresist/etched-gold mask into the semiconductor.

Figure 5(b) shows simulated and measured (smoothed) reflectivity data vs etch depth of test sample-A with MQWs. There is general agreement. The test sample was patterned with a 1 mm \times 1 mm region unmasked so that it could be etched to remove the MQW (passive). Figure 5(c) shows the original measured reflectivity data vs etch depth of the etching test structure. There are two humps in the profile. As soon as the 2nd dip is observed, it starts to rise, and finally gets flat, the etch needs to be stopped, indicating that the waveguide layer is reached. Figure 5(d) shows a microscope image of this test structure after etching, showing the active (unetched since covered with photoresist) and passive (etched) regions.

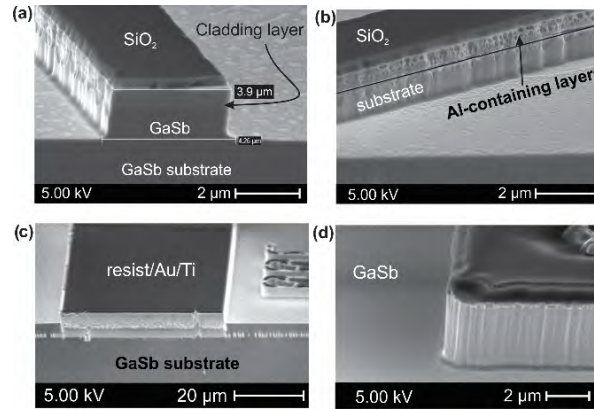


Fig. 4. SEM images of the test samples with 5- μm surface ridges obtained after (a) Cl_2/N_2 dry etching, (b) dry etching followed by 5 sec cleanup etching by HCl. Sidewalls can also be seen here after, (c) 50- μm wide stripes covered with resist and Ti//Au metal layer underneath after dry etching in Cl_2/N_2 plasma and (d) the close-up view of the ridges are shown at the bottom.

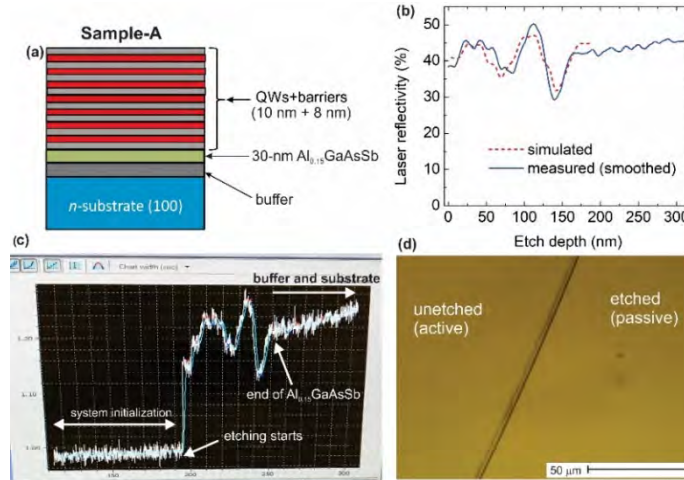


Fig. 5. (a) Schematic of the test structures for active/passive definition test, (b) simulated and measured (smoothed out) reflectivity data as a function of etch depth are superimposed; (c) system's original raw data for the detection of endpoint during dry etching using Cl_2/N_2 plasma; and (d) microscope image of the test structure after the etching, showing active/passive regions.

In order to assess the effect of the developed plasma etch process on our material structure, Fabry P rot broad-area lasers with a wide ridge using this ICP dry etch were fabricated. I - V characteristics of the device were then measured under both forward and reverse biases. Laser devices exhibit reasonable dark current and threshold current at room temperature, hinting that the plasma etch did not affect the device performance.

3.2 Wet chemical etching

A number of etchants along with the etch rates for different materials are listed in Table 2. One of the most-used wet etchants is Solution-1. Using this etchant, GaSb, InAs, and InGaAsSb are etched with a smooth surface and a good reproducibility. For Al-containing layers, this etchant shows fast etching rate when the Al-content is low (Al<30%). For the Solution-2, we found the same etch rates as reported by Dier *et al.* [10]. Most importantly, selective removal of InAsSb from GaSb can be done by this solution.

Table 2. Wet-Etchants for Antimonide Materials Used in This Study

#	Wet etchants	Etching rate (nm/sec)				
		GaSb	In _{0.43} GaAsSb	Al _{0.5} GaAs _{0.04} Sb	InAs _{0.91} Sb	Al _{0.2} In _{0.2} GaAs _{0.19} Sb
1	C ₄ H ₄ KNaO ₆ :HCl:H ₂ O ₂ = 50 : 40 : 3.5	12	6	5	0.4	4
2	C ₆ H ₈ O ₇ :H ₂ O ₂ = 2 : 1	0.01	0.23	-	1.5	-
3	HCl:H ₂ O ₂ :H ₂ O = 100 : 1 : 100	4.2	-	10	0.8	1
4	H ₃ PO ₄ : H ₂ O ₂ : C ₆ H ₈ O ₇ : H ₂ O = 3 : 5 : 55 : 22	2.5-3 (fairly unselective)				
5	AZ726 MIF developer	0.17 (GaSb/InAs superlattice)				
6	Buffered HF	570 (plasma exposed GaSb, AlGaAsSb and InAs)				

HCl-based etchant (Solution-3) could also be used in removing antimonide materials. However, the surface morphology of GaSb and low-Al containing materials usually gets rough with this etchant. Figure 6 presents the microscope image of the Al_{0.5}GaAsSb surface after being etched by this etchant, showing the surface roughness is about 8 nm, as measured by the surface profilometer. However, this etchant is useful because it shows good selectivity between lattice-matched quinary AlGaInAsSb and AlGaAsSb with 80% Al-composition. In fact, one could obtain a selectivity higher than 30 between the Al_{0.85}GaAs_{0.07}Sb and Al_{0.2}In_{0.25}GaAs_{0.23}Sb layer with a reproducible etch rate and smooth surface after the etching [17]. The etching rate for the etch stop layer is accurate and reproducible. The HCl etchant shows fast etching rate for Al-rich (Al>50%) layers. This high degree of selectivity confirmed that the Al_{0.2}In_{0.25}GaAs_{0.23}Sb alloy could be suitable for the etch stop layer [17].

Solution-4 can be used to etch antimonides with a moderate etching rate in an unselective way. It could be used for processing interband cascade laser [18] devices where several hundred to over a thousand epilayers of short-period antimonide-based superlattice with different constituents are grown as a part of the device structure. Solution-5 and 6 are not that useful as etchants. However, the device manufactures should be aware of these two etchants as well as their etch rates.

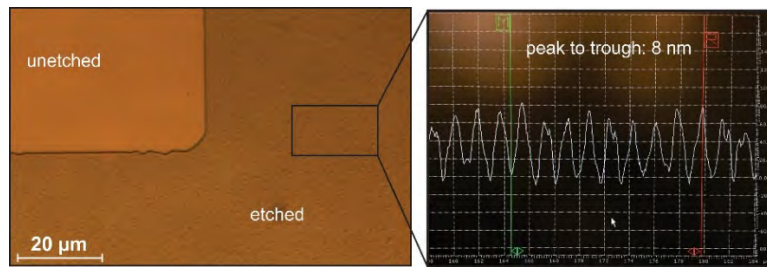


Fig. 6. Optical microscope image of the etched surface after wet chemical etching (left) of $\text{Al}_{0.5}\text{GaAsSb}$ by HCl-based etchant. Roughness measurement of the etched surface is also shown by the profilometer (right).

3.3 GaSb substrate removal

The substrate removal procedure is described in detail in ref [19]. This could be done by the SIRTl etchant which is referred to the mixture of HF/CrO_3 . Transene Inc. stocks two premixes, 1:5 and 1:10 Sirtl: H_2O . The former solution shows a very high etch rate of GaSb material, which one could begin with to remove the bulk of the material. Given that, this etchant exhibits very high selectivity between GaSb and InAsSb, 1:100 Sirtl: H_2O could be used to stop etching on thin layers of InAsSb. Thus, a smooth, mirror-like light-blue colored thin InAsSb layer can be obtained at the end of the removal process.

4. Conclusion

Selective wet and dry etching processes have been explored for the quaternaries lattice-matched to GaSb. Useful wet etchants and dry etching processes are given. In particular, materials and processes relevant to establishing a fabrication procedure for widely-tunable SG-DBR lasers in the SW/MW-IR wavelength regime using antimonide materials system have been defined. By employing an MQW InGaAsSb/AlGaAsSb/GaSb gain material and necessary processing steps, one could develop a PIC technology in the GaSb material system that contains a MQW active region, which is selectively removed either by a wet or dry etch using an etch stop layer or by a time-controlled etch, aided by a laser monitor if done by dry ion-etching. This makes the integration platform the simplest way to combine active and passive components on a chip. In fact, the fabrication of many other optoelectronic devices could benefit from the etching and processing technology outlined in this paper.

Acknowledgments

The authors gratefully acknowledge the help of Dr. Demis John for *in situ* dry etching of antimonides.

References

1. B. R. Bennett, R. Magno, J. B. Boos, W. Kruppa, and M. G. Ancona, "Antimonide-based compound semiconductors for electronic devices: A review," *Solid-State Electron.* **49**(12), 1875–1895 (2005).
2. M. Mohapatra, A. Mumtaz, and A. K. Panda, "Performance evaluation of GaSb/AlGaAs based high electron mobility transistors," in 3rd International Conference on Advances in Recent Technologies in Communication and Computing (ARTCom), Bangalore, India, 2011, pp. 249 – 252.
3. R. Chao, J. Wun, Y. Wang, Y. Chen, J. E. Bowers, and J. Shi, "High-speed and high-power GaSb based photodiode for 2.5 μm wavelength operations," in IEEE Photonics Conference (IPC), Waikoloa, HI 2016, pp. 472–473.
4. S. Suchalkin, S. Jung, G. Kipshidze, L. Shterengas, T. Hosoda, D. Westerfeld, D. Snyder, and G. Belenky, "GaSb based light emitting diodes with strained InGaAsSb type I quantum well active regions," *Appl. Phys. Lett.* **93**(8), 081107 (2008).
5. K. Kashani-Shirazi, K. Vizbaras, A. Bachmann, S. Arafin, and M.-C. Amann, "Low-threshold strained quantum-well GaSb-based lasers emitting in the 2.5- to 2.7- μm wavelength range," *IEEE Photonics Technol. Lett.* **21**(16), 1106–1108 (2009).
6. O. Blum, M. J. Hafich, J. F. Klem, K. Baucom, and A. Allennan, "Wet thermal oxidation of AlAsSb against As/Sb ratio," *Electron. Lett.* **33**(12), 1097–1099 (1997).

7. S. Arafin, A. P. McFadden, M. Pendharkar, C. J. Palmström, and L. A. Coldren, "Recent progress on GaSb-based photonic integrated circuits," in 14th International Conference on Mid-Infrared Optoelectronics, (MIOMD), Flagstaff, AZ, USA, 2018, pp. 1–2.
8. S. Arafin, A. Bachmann, K. Kashani-Shirazi, and M.-C. Amann, "Electrically-pumped continuous-wave vertical-cavity surface-emitting lasers at 2.6 μm ," *Appl. Phys. Lett.* **95**(13), 131120 (2009).
9. J. W. Raring, M. N. Sysak, A. Tauke-Pedretti, M. Dummer, E. J. Skogen, J. S. Barton, S. P. DenBaars, and L. A. Coldren, "Advanced integration schemes for high-functionality/high-performance photonic integrated circuits," in *SPIE* **6126**, 61260H (2006).
10. O. Dier, C. Lin, M. Grau, and M.-C. Amann, "Selective and non-selective wet-chemical etchants for GaSb-based materials," *Semicond. Sci. Technol.* **19**(11), 1250–1253 (2004).
11. S. J. Pearton, F. Ren, T. R. Fullowan, A. Katz, W. S. Hobson, U. K. Chakrabarti, and C. R. Abernathy, "Plasma etching of III–V semiconductor thin films," *Mater. Chem. Phys.* **32**(3), 215–234 (1992).
12. L. A. Coldren, S. C. Nicholes, L. Johansson, S. Ristic, R. S. Guzzon, E. J. Norberg, and U. Krishnamachari, "High Performance InP-Based Photonic ICs—A Tutorial," *J. Lightwave Technol.* **29**(4), 554–570 (2011).
13. X. Zhang, Y. Li, X. Wang, Y. Li, G. Yue, Z. Wang, J. Xie, J. Zhang, and Y. Hao, "Study on etch process of GaSb-based VCSEL," *Guangdian Gongcheng* **44**(12), 1225–1229 (2017).
14. M. You, Q. Sun, S. Li, L. Yin, X. Li, and J. Liu, "Study on HCl system wet-etching process of GaSb-based materials," in 4th International Conference on Machinery, Materials and Information Technology Applications, Atlantis Press, 2016.
15. H. Hong-Yue, X. Wei, W. Guo-Wei, X. Ying-Qiang, R. Zheng-Wei, H. Xi, H. Zhen-Hong, L. Yong-Ping, W. Si-Hang, and N. Zhi-Chuan, "Wet chemical etching of antimonide-Based infrared materials," *Chin. Phys. Lett.* **32**(10), 107302 (2015).
16. L. W. Stulz and L. A. Coldren, "Orientation of (100) InGaAsP/InP wafers by HCl chemical etching," *J. Electrochem. Soc.* **130**(7), 1628–1630 (1983).
17. S. Jung, "Mid infrared III-V semiconductor emitters and detectors," PhD dissertation, Stony Brook University, New York, USA, (2012).
18. S. M. S. Rassel, L. Li, Y. Li, R. Yang, J. Gupta, X. Wu, and G. Aers, "High-temperature and low-threshold interband cascade lasers at wavelengths longer than 6 μm ," *Opt. Eng.* **57**(1), 011021 (2018).
19. S. Arafin, "Electrically-pumped GaSb-based vertical-cavity surface-emitting lasers," PhD dissertation, Technical University of Munich, Munich, Germany, (2012).

Design of High-Power Electrically-Pumped VECSELs for the 3-4 μm Wavelength Range

Shamsul Arafin
Department of Electrical and Computer
Engineering
The Ohio State University
Columbus, OH 43210, USA
arafin.1@osu.edu

Larry A. Coldren
Department of Electrical and Computer
Engineering
University of California Santa Barbara
Santa Barbara, CA 93106, USA
coldren@ucsb.edu

Sarvagya Dwivedi
IMEC
Kapeldreef 75
Leuven, Belgium
Sarvagya.dwivedi@imec.be

Abstract—We report the design of electrically-pumped high-power vertical-external-cavity surface-emitting lasers emitting at the mid-wave infrared wavelength regime. The device is designed with a monolithic configuration that can provide multiwatts of continuous-wave output power in a single transverse mode with an excellent beam quality.

Keywords—mid-wave infrared, cw output power, vertical-external cavity surface-emitting laser (VECSEL), interband cascade laser, brightness

I. INTRODUCTION

Given that the mid-wave infrared (MWIR) region has a superior transmission through atmosphere and better penetration through fog, dust and smoke comparing to visible, and NIR wavelength regime [1], the development of MWIR lasers and the associated systems are of significant interests for advanced military operations. At the same time, there is also a pressing need to develop low-size, weight, power and cost (SWaP-C) lasers with a few watts of output power and high brightness for enabling a wide range of defense applications including countermeasure and night vision [2]. Among several types of semiconductor diode lasers, electrically-pumped (EP) vertical-external-cavity surface-emitting laser (VECSEL) is one of the most suitable light sources that provide excellent beam quality and relatively high optical powers.

In order to obtain even more power that is not possible from a single emitter, two-dimensional (2D) arrays for this type of semiconductor lasers offer an attractive solution for power scaling without degrading the beam quality. Another important requirement of this defense application that needs to be met is that the high-power light source should involve minimal to no free-space optics in order to reduce the effects of shock, vibration and extreme temperature variations, necessitating a highly-integrated solution. Also, given that a VECSEL's cavity can be very well modeled by planar mirror and a spherical mirror spaced by many beam waists, its fundamental mode is given by a Gaussian, and thus it is natural to have $M^2 \sim 1.1$. As a consequence, its brightness can be ~ 3 times that of other schemes with $M^2 \sim 3$. That is, a VECSEL with an output of 4 Watts can have a brightness greater than a 10 Watt laser with an M^2 of 3.

In this work, we have studied the design, epitaxy, and fabrication process of high-power MWIR VECSELs with the objective of a few watts of output power and a circular near-diffraction limited (Gaussian) output beam at the same time. By varying the constituent semiconductor materials and the structural design parameters, the VECSEL emission wavelength can be varied from 3 μm to 4 μm . However, the overall design reported in this study is applicable for covering even wider wavelength ranges.

II. DEVICE DESIGN

The targeted wavelength range is accessible by the GaSb material system. Molecular beam epitaxy (MBE) is still considered to be the only viable growth technology for this material system required in such a very-long wavelength VECSEL structure. Figure 1 shows our proposed EP-VECSEL design for efficient, high brightness operation. Heat is extracted through the integrated Au-heat sink as well as through the top bonded sapphire substrate, which forms the external cavity, and serves as the external mode-controlling output coupler.

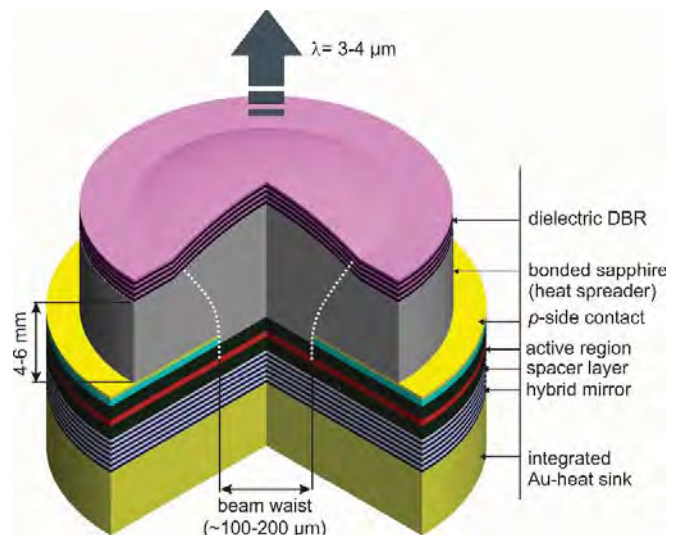


Fig. 1 Sketch of an electrically-pumped VECSEL with an episcide down configuration for the 3-4 μm wavelength range. Several device components are indicated.

One could think of growing this either with the VECSEL-epitaxial DBR on top or on the bottom of the first growth. Here we consider that the epitaxial growth of the VECSEL-DBR is grown on top so that it is positioned at the bottom after removing the substrate and the device mesa is bonded face down to an integrated Au heat sink. We will then form the contacts to the laterally positioned contacts, attach the sapphire external-cavity chip to the top of the epi-stack on the GaSb wafer, and then remove the GaSb substrate, metalize the bottom DBRs for more reflection, and finally attach the heat sinks at the bottom. The gold layer thickness should be increased up to about 50-60 μm by electroplating. The electro-plated gold pseudo-substrate provides mechanical stability and serves as an excellent heat-sink.

EP-VECSELS require larger gain and incorporate as many quantum wells as practical, consistent with the resonant periodic gain principle [3]. To maximize overlap between the quantum wells and the optical standing wave, the cavity can be extended to a few wavelengths in length with the quantum wells clustered around the standing wave peaks.

A. Current Aperture

In conventional EP-VECSELS with a large-area, current injection from the top annular p -contact and uniform current distribution around the active region is always a big concern. Due to non-uniform current injection from annular contact and the resulting spatial hole burning, EP VECSELS are much rarer. This problem can be naturally overcome by incorporating the cascaded active region typically used in lasers for $\lambda > 3 \mu\text{m}$. As a matter of fact, EP-VECSELS are improved by interband cascade laser (ICL) active regions with short-period superlattices (SLs) at several stages that induces 100-200 μm of current spreading, which is highly advantageous unlike edge emitters. Current spreading along the transverse plane (i.e. perpendicular to growth direction) is very significant in a cascaded structure with thousands of thin layers that magnify resistance anisotropy [4]. In other words, a large ratio between in-plane and vertical conductivity in the cascaded layer structure ensures excellent lateral carrier injection through metal contacts with the intra-cavity configuration.

Excessive lateral current spreading in such cascaded structures also creates a problem in making current confinement of the devices. As it is known that V(E)CSELS require an aperture close to the active region for current confinement. Unfortunately, the buried tunnel junction (BTJ) concept [5] cannot be used to confine the current at the center of EP-VECSELS with a multi-stage ICL active region. Even monolithic aperture-VECSELS based on the selective, lateral under-etching of the tunnel-junction to define carrier confinement cannot solve the problem in VECSELS with multi-stage ICL active region [6]. Most importantly, the apertureless device becomes power-hungry since they experience higher optical loss due to the interaction between top annular contact and transverse modes emerging from the resonator. The n -mirror is probably the place to form a potential aperture. Ion implantation is one possibility to explore [7].

B. Highly-Reflective Mirror

The bottom epitaxial Bragg reflector consists of a few-pairs of $1/4\lambda$ thick n -doped AlAsSb/GaSb layers grown on an n -doped GaSb substrate. Unlike GaSb-based VCSELS with 24-26 layer pairs to get reflectivity approximately $>99.8\%$, we consider to utilize a hybrid mirror that consists of a combination of only 10.5-12.5 pairs of AlAsSb/GaSb layers with refractive index contrast $\Delta n = 0.6$ at 4 μm , a GaSb phase matching layer and a terminating Au layer, yielding reflectivity $\sim 99.98\%$. With these extreme high reflectivities, this kind of mirror is qualified as a substrate-side mirror of the VCSEL, where no light is coupled out. The mirror structure will be followed by an n -type GaSb current spreading layer and an active region. The growth will be continued by depositing a phase adjustment n -type current spreading layer and a contact layer. The components were processed on the wafer by etching a mesa structure and fabricating necessary passivation layers and metal contacts as shown in Figure 1.

The top dielectric DBR consists of only 5-pairs of ZnS and Ge layers. These two dielectric mirror materials can be deposited by e-beam evaporation on the sapphire spacer which contains the spherical mirror. Despite of the poor thermal conductivity of these dielectric materials, the peak reflectivity of this mirror can be as high as 99.8% by considering Δn between these two materials to be approximately ~ 2.0 at around 4 μm .

C. Active region

Type-II QWs based active region utilized in GaSb based VECSELS with $\lambda > 3 \mu\text{m}$. A single-stage (non-cascaded) active region consists of type-II QWs can be used [8]. This can be made of a $\text{Ga}_{0.9}\text{In}_{0.1}\text{Sb}$ hole confining QW sandwiched between two InAs electron confining QWs, as commonly used in ICLs. The photon energy corresponding to the lasing wavelength can be changed by changing the thickness of the constituent QWs. The thickness of the AlGaSb barriers between the QWs can be chosen in a way that prevent excess energy broadening of the mini-bands and allow homogeneous filling of the QWs by tunneling at the same time. A multi-stage type-II QW-based active region can also be employed [9]. Such a higher stage multiplicity in these VCSEL devices assures sufficient gain to overcome the cavity loss. The layering and right doping configurations of the active stages with carrier rebalancing may be important to significantly reduce the threshold current density of the device [10].

REFERENCES

- [1] N. S. Prasad, "Optical Communications in the mid-wave IR spectral band," in *Free-Space Laser Communications: Principles and Advances*, Springer New York : New York, 2008, pp. 347-391.
- [2] S. Arafin, "Recent progress on GaSb-based electrically-pumped vertical cavity surface emitting lasers emitting above 4 μm ," 2019 SPIE Defense and Commercial Sensing, Baltimore, MD, USA, April 2019, paper 10980-16.
- [3] L. Fan, J. Hader, M. Schillgalies, M. Fallahi, A. R. Zakharian, J. V. Moloney, et al., "High-power optically pumped VECSEL using a double-well resonant periodic gain structure," in *IEEE Photon. Technol. Lett.*, vol. 17, no. 9, pp. 1764-1766, Sept. 2005.

- [4] R. Q. Yang, "Interband Cascade (IC) Lasers. in Semiconductor Lasers: Fundamentals and applications," Woodhead Publishing : Oxford, UK, 2013.
- [5] S. Arafin, A. Bachmann, K. Kashani-Shirazi, and M.-C. Amann, "Electrically-pumped continuous-wave vertical-cavity surface-emitting lasers at $\sim 2.6\mu\text{m}$," Appl. Phys. Lett. vol. 95, no. 13, p. 131120, Dec. 2009.
- [6] D. Sanchez, L. Cerutti, and E. Tournié, "Mid-IR GaSb-based monolithic vertical-cavity surface-emitting lasers," J. Phys. D: Appl. Phys. vol. 46, no. 49, p. 495101, Nov. 2013.
- [7] Private Communication with Jerry Meyer at Naval research Lab.
- [8] G. K. Veerabathran, S. Sprengel, A. Andrejew, and M. C. Amann, "Room-temperature vertical-cavity surface-emitting lasers at $4\mu\text{m}$ with GaSb-based type-II quantum wells," Appl. Phys. Lett. vol. 110, no. 7, p. 071104, Jan. 2017.
- [9] W. W. Bewley, C. L. Canedy, C. S. Kim, C. D. Merritt, M. V. Warren, I. Vurgaftman, J. R. Meyer, and M. Kim, "Room-temperature mid-infrared interband cascade vertical-cavity surface-emitting lasers," Appl. Phys. Lett. vol. 109, no.15, p. 151108, Oct. 2016.
- [10] I. Vurgaftman, , W. W. Bewley, C. L. Canedy, C. S. Kim, M. Kim, C. D. Merritt, J. Abell, J. R. Lindle, and J. R. Meyer, "Rebalancing of internally generated carriers for mid-infrared interband cascade lasers with very low power consumption," Nat. Commun., vol. 2, p. 585, Dec. 2011.

I. Photonic Integrated Circuits

C. PICs for Free-Space Links and LIDAR

High Power Indium Phosphide Photonic Integrated Circuit Platform

Hongwei Zhao, Sergio Pinna, Fengqiao Sang, Simone Tommaso Šuran Brunelli,
Larry A Coldren, Jonathan Klamkin

*Electrical and Computer Engineering Department, University of California Santa Barbara,
Santa Barbara, CA 93106, USA*

Email: hwzhao@ece.ucsb.edu / Phone: (805)8935955

High-power photonic integrated circuits (PICs) are of interest for a variety of applications including microwave photonics, free space optical communications and coherent LiDAR systems [1, 2]. Indium phosphide (InP) is the most advanced platform for high-performance PICs. InP PICs are particularly attractive for free space optical communications, which requires low cost, size, weight and power (CSWaP) [3-5]. In conventional InP PICs, saturation power of semiconductor optical amplifiers (SOAs) is limited by small modal size and high confinement factor (>5%). To improve the SOA saturation power, one approach is to increase the modal size with a flared waveguide, but the large beam dimension in the horizontal direction imposes challenges on the coupling to single-mode fiber [6]. A second approach is to reduce the confinement factor. Slab-coupled optical waveguides (SCOW) with small confinement factor have been investigated for high-power SOAs and lasers. However, it is very challenging to monolithically integrate the SCOW SOAs with other optical elements required for a PIC such as a seed laser and modulator [7]. In this work, we have proposed a novel platform enabling the monolithic integration of low-confinement SOAs with other high-confinement components including a distributed Bragg reflector (DBR) laser and high-speed electro-absorption modulator (EAM).

The epitaxial structure was grown by metal organic chemical vapor deposition (MOCVD) on n-type (001) InP substrates. As shown in Fig. 1(a), two waveguide layers (WG 1 and WG 2) were deposited on the substrate. The lower waveguide layer (WG2) is a low-index dilute waveguide. The active region, on top of the waveguide layers, consists of 5 pairs of indium gallium arsenide phosphide (InGaAsP) quantum wells. The corresponding fundamental TE modes in ridge waveguides are shown in Fig. 1(b) and (c). For a single-ridge waveguide, the ridge width is 3 μm and the vertical etch was stopped above the active region, resulting in a modal area of 3.4 μm^2 and confinement factor of 3.7%. To achieve higher saturation power in SOAs, a larger modal area and lower confinement factor would be preferred. With this epitaxial structure, large modal area can be achieved by engineering the waveguide geometry. As shown in Fig. 1(c), a double-ridge waveguide design enables a modal area up to 11.4 μm^2 while the confinement factor is only 0.35%.

Figure 2 (a) shows the microscope image of fabricated PIC transmitter with the above epitaxial structure. It consists of a DBR laser, a high-speed SOA (SOA 1), an EAM, and a high-power two-section output booster SOA (SOA 2). All components in the transmitter were designed with single-ridge waveguide structure and integrated by quantum well intermixing technique. The bangap of the gain, modulator and passive sections are 1550 nm, 1490 nm and 1450 nm, respectively. The LIV characteristic of the DBR laser is demonstrated in Fig. 2(b), which shows a threshold of 65 mA. Off-chip power versus the current density in the second section of the booster SOA (SOA 2) is shown in Fig. 2(c). The current of the laser gain section, the SOA 1, and the first section of the SOA 2 are 150 mA, 90 mA and 140 mA, respectively. The maximum output power with the above DC biasing is 19.4 dBm (87 mW). The PIC transmitter was solder mounted to ceramic carriers. The P pad of the EAM was wire bonded to a 50- Ω RF feeding transmission line to characterize the high-speed performance. Eye diagrams for NRZ OOK modulation up to 20 Gbps are shown in Fig. 2(d).

With the same epitaxial structure, double-ridge waveguide SOAs were fabricated, which is shown in Fig. 3(a). The length of the SOAs is 4 mm and the waveguides are angled to reduce reflection at the facets. The output optical power of the double-ridge SOA at different input optical power levels is demonstrated in Fig. 3(b). The driving current was increased up to 1 A. The output optical power was measured by a germanium detector, which was placed next to the output facet. With 17-dBm input power, the output power is up to 23.8 dBm (240 mW).

In future work, we will integrate the high-confinement transmitter (Fig. 2(a)) with the low-confinement SOA (Fig. 3(a)). Since they are designed with the same epitaxial structure, it only requires a transition stage between the single-ridge and double-ridge waveguides, where usually a linear width taper is sufficient. Besides, in future measurements with AR coated devices, higher output optical power is expected.

- [1] D. O. Caplan, *J. Opt. Fiber Commun.* 4, p. 225-362, 2007. [2] B. Isaac *et al. IEEE Int. Semi. Laser Conf. 2018*, paper MC.7.
[3] H. Zhao *et al. IEEE J. Quant. Elec.*, 24, 6, 2018. [4] H. Zhao *et al., Proc. Adv. Photon. 2018*, paper. ITu4B.6.
[5] V. Rosborough *et al., Proc. Adv. Photon. 2016*, paper ITu2A.3. [6] G. Bendeli *et al., IEEE Photonic Letter*, 3, 1, 1991.
[7] J. J. Plant *et al. IEEE Photon. Technol. Lett.*, 17, 4, p.735-737, 2005.

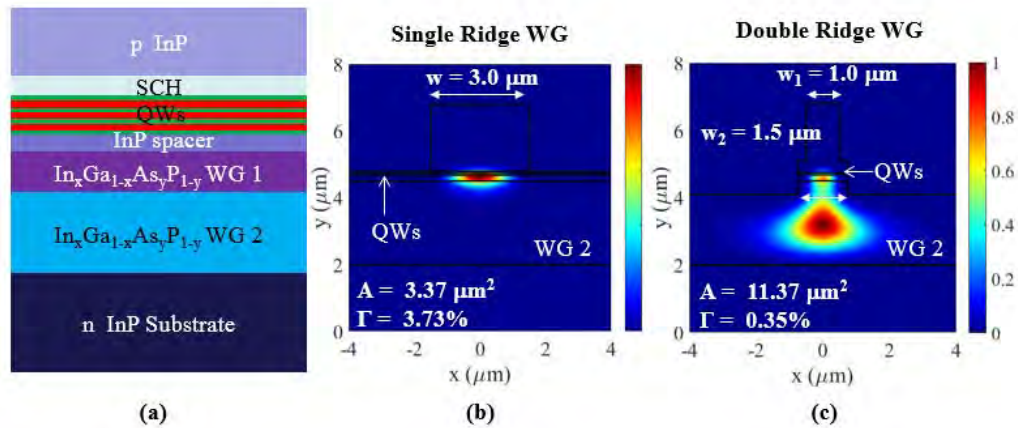


Fig. 1. (a) Epitaxial structure (not to scale); (b) Fundamental TE mode in a single-ridge waveguide; (c) Fundamental TE mode in a double-ridge waveguide.

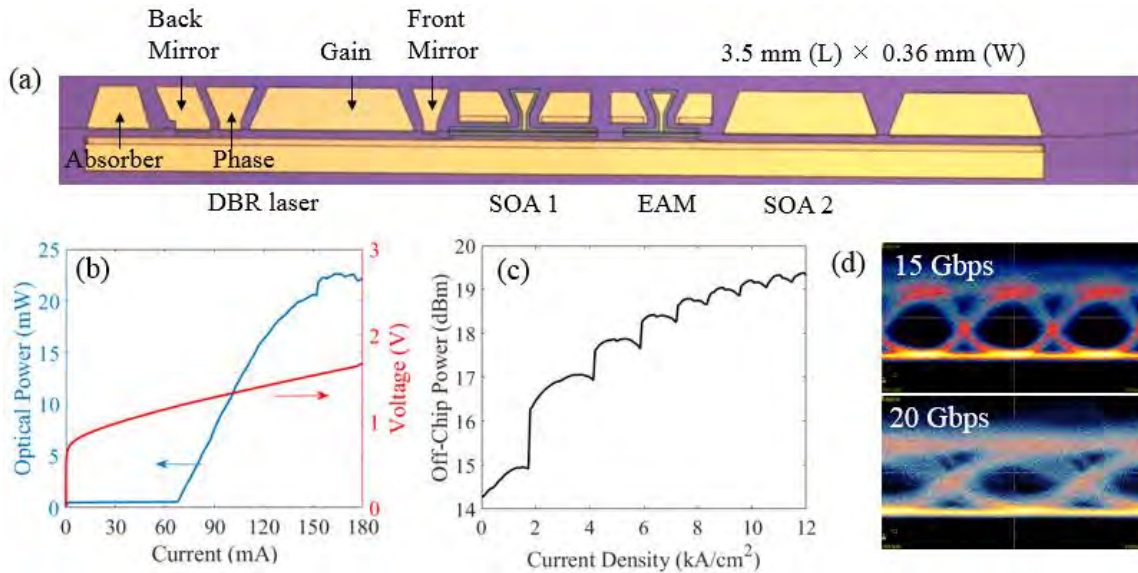


Fig. 2. (a) Microscope image of fabricated InP PIC transmitter consisting of a DBR laser, an electro-absorption modulator and two SOAs, all elements are designed with single-ridge waveguide structure; (b) DBR laser LIV curve (with CW current source); (c) Off-chip optical power of the PIC transmitter versus the current density in the second section of the booster SOA; (d) Eye diagrams with NRZ OOK modulation.

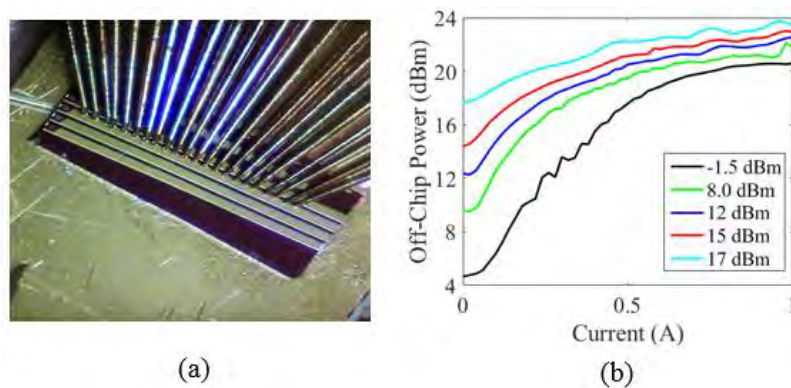


Fig. 3. (a) Fabricated double-ridge waveguide SOAs (4-mm long); (b) Output optical power of the double-ridge waveguide SOA with different fiber-coupled input power levels.

Waveguide Uni-Traveling-Carrier Photodiodes for mmW Signal Generation: Space-Charge Impedance and Efficiency Limitations

Brandon Isaac¹, Yuan Liu², Sergio Pinna², Larry Coldren^{1,2} and Jonathan Klamkin²

¹Materials Department, University of California, Santa Barbara, California 93106, USA

²Electrical and Computer Engineering Department, University of California, Santa Barbara, California 93106, USA

Email: Brandonjisaac@ucsb.edu / Phone: (859)-801-2263

Overview

Photonic generation of mmW signals using high-speed photodiodes is promising due to the potential for ultra-wide bandwidth [1-3]. Uni-traveling carrier photodiodes (UTC-PDs) based on the InGaAs/InP material system have demonstrated measured RF output powers of 10 dBm, 6 dBm, and -2.2 dBm at frequencies of 100 GHz, 170 GHz, and 300 GHz respectively [4-6]. However, the power conversion efficiency (PCE) is a metric that has seen relatively little investigation and is important for practical applications [7]. The PCE is given by the output RF power, $\frac{1}{2} R_L I_{RF}^2$, divided by the sum of the input optical power, P_{opt} , and the DC power, $I_{ph} \cdot V_{Bias}$, applied to the diode. For the results in Refs. 4-6, the PCE is in the range of 1% to 10%. To investigate the efficiency limitations, we utilize the assumptions from Ref. 7 to write the PCE as $\eta_{RF} = \frac{1}{2} \cdot \frac{m^2 R_L}{I_{DC}^{-1}(V_{th} + 1/\mathcal{R}) + \alpha^{-1} + m(R_L + \alpha^{-1})}$ (1), where R_L is the load impedance, m is the optical modulation index, I_{DC} is the average photocurrent, V_{th} is the minimum bias to operate at high frequencies for low photocurrent, α^{-1} is the device series resistance, and \mathcal{R} is the optical to electrical responsivity (A/W). The series resistance term, α^{-1} , includes resistances of the device such as contact resistance and sheet resistance, as well as an effective space-charge impedance. The space-charge impedance results from the electrical field of the photo-generated carriers in the junction that reduce the built-in field. Waveguide (WG) UTC-PDs were fabricated and here we characterize their space-charge impedance to demonstrate that this is the limiting factor for PCE and an important metric to quantify in state-of-the-art UTC-PDs.

Experimental Results

Fig. 1(a) shows a false colored SEM of the fabricated WG UTC-PD. A simulation of the optical mode along with the epitaxial structure is shown in Fig. 1(b) and 1(c). RF characterization of the device was completed using a 67 GHz Lightwave Component Analyzer. The frequency response of the device is shown in Fig 2(a) at a low (blue) and high (red) photocurrent level with a bias of -2 V. The 3-dB bandwidth under various photocurrents and bias voltages is shown in Fig. 2(b), demonstrating bandwidths of 45 GHz under low photocurrent ($\sim 90 \mu\text{A}$) and increasing to 50 GHz under large photocurrent ($\sim 6 \text{mA}$). We also measured S_{11} under low photocurrent for extracting the junction capacitance and series resistance of 27 fF and 5Ω using the RC model shown at the inset of Fig. 2(b).

To extract the effective series resistance included in Eq. 1, the relative power measured at 60 GHz as a function of input photocurrent at different reverse biases is plotted in Fig. 3(a) along with the RF compression relative to the 50- Ω line (black dashed line in Fig. 3(a)) shown in Fig. 3(b). For each reverse bias, the photocurrent at which the compression reaches -1 dB is plotted in Fig. 3(c). The slope of this curve, 275 Ω , provides the total series resistance, $\alpha^{-1} + m(R_L + \alpha^{-1})$. For this measurement, the modulation index is around 0.1 resulting in a series resistance, α^{-1} , of 245 Ω . Comparing this to the series resistance obtained from fitting S_{11} shows that the major contribution to the effective series resistance is the space-charge impedance. Inserting the effective series resistance into Eq. 1 gives a maximum achievable efficiency of 4.6% for a modulation index of 1.

Conclusion

We fabricated and characterized a WG UTC-PD designed for mmW generation. The device characteristics were investigated to understand the effect of space-charge impedance on the PCE. This was shown to be the dominant factor in limiting the maximum achievable PCE. This result emphasizes the need for state-of-the-art photodiodes to be characterized for space-charge impedance in addition to bandwidth and RF output power at mmW frequencies. As was shown in Fig. 1(b), there is strong optical overlap with the absorbing region. The epitaxial and waveguide design are two important parameters that can be engineered to potentially obtain lower space charge impedance.

[1] T. Nagatsuma et al., Laser and Phot Rev. (2009) [2] Y. Liu et al., IEEE JSTQE 2018 [3] S. Iezekial et al., IEEE Micro. Mag. 2015 [4] E. Rouvalis et al., Optics Express, (2010) [5] J. W. Shi et al., IEEE PTL, Vol. 24, (2012) [6] P. Patzel et al., 11th Euro. Conf. on Ant. and Prop. (2017) [7] D. A. Tulchinsky et al., JLT, Vol. 26 (2008) [8] B. Isaac et al. OFC 2019

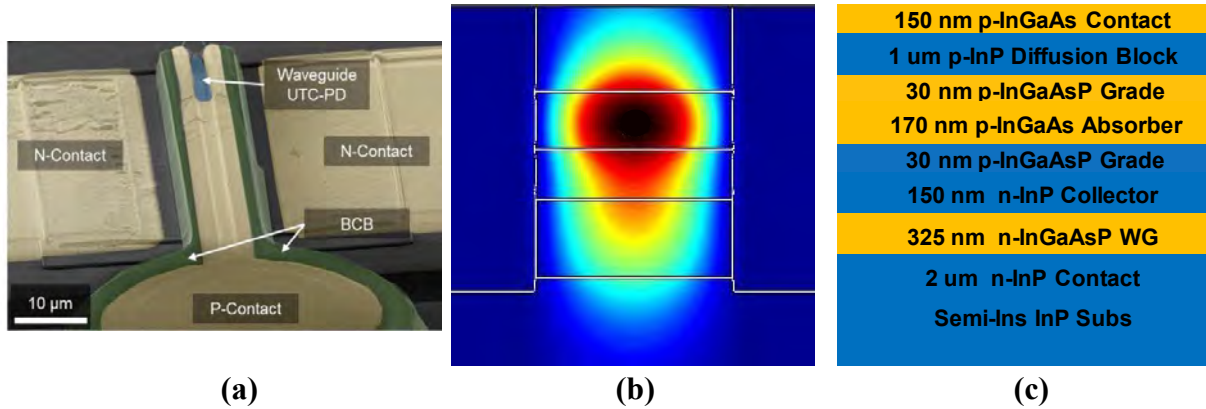


Fig. 1. (a) False colored SEM image of fabricated device. BCB was used to reduce parasitic capacitance. (b) Optical mode of the waveguide. (c) Epitaxial structure. The waveguide design, including both the physical layout and layer compositions, can be engineered to reduce the space-charge impedance.

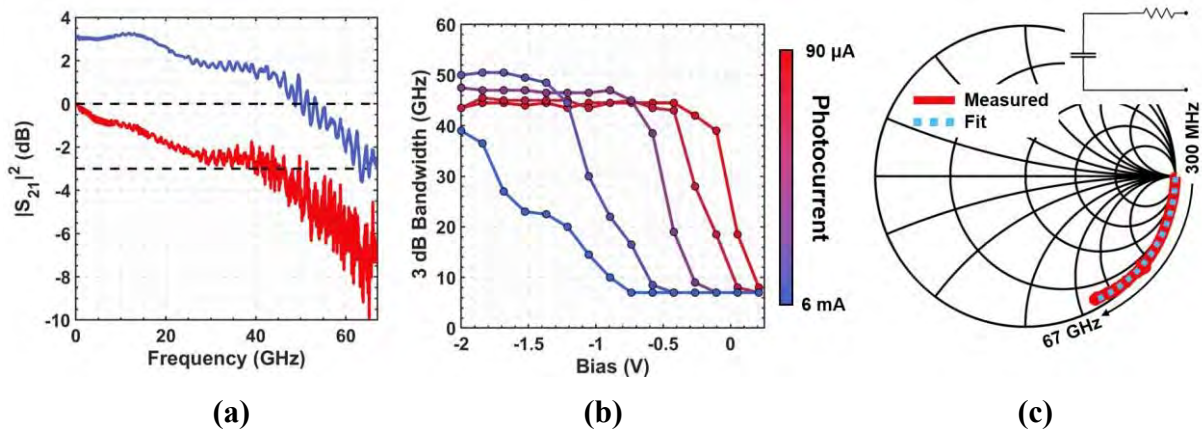


Fig. 2. (a) Frequency response of device at -2 V bias showing 3-dB bandwidth of 45 GHz under low (red) and 50 GHz under high (blue) optical illumination. (b) 3-dB bandwidth for increasing photocurrent and bias ranging from 90 μ A to 6 mA and 0.25 V to -2 V. (c) S_{11} from 300 MHz to 67 GHz at -2 V bias. Fitting to the model shown in the inset gives a total capacitance of 27 fF and series resistance of 5 Ω .

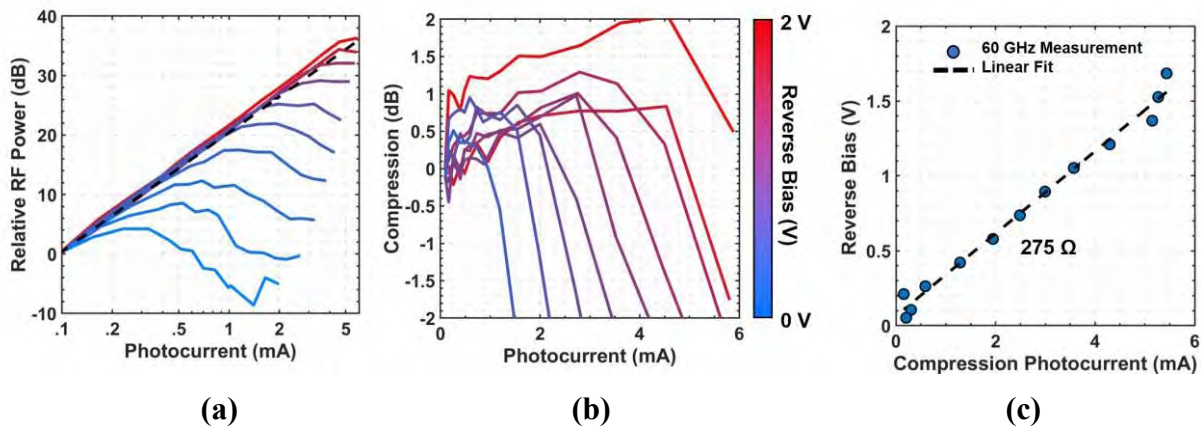


Fig. 3. (a) Relative RF power at 60 GHz as a function of DC photocurrent under various reverse biases. Black dashed line is 50 Ω line. (b) Compression from 50 Ω line as a function of photocurrent. The color legend applies to both (a) and (b). (c) Bias voltage at -1 dB compression for various photocurrents. The slope of the line, 275 Ω , gives the total series resistance.

INTEGRATED MICRO-PHOTONICS FOR REMOTE EARTH SCIENCE SENSING (IMPRESS) LIDAR

Mark Stephen¹, Jonathan Klamkin², Larry Coldren², Joseph Fridlander², Victoria Rosborough², Fengqiao Sang², Jeffrey Chen¹, Kenji Numata¹, Randy Kawa¹

¹NASA-GSFC – Greenbelt, MD 20771

²UCSB - Electrical and Computer Engineering Department, Santa Barbara, CA 93106

ABSTRACT

We present recent progress on a wavelength tunable, pulsed laser source for laser spectroscopy of CO₂ at 1572 nm. An integrated photonics design in indium phosphide (InP) is presented and compared to a fiber-component-based implementation. Significant improvement in size, weight and complexity is demonstrated.

Index Terms— Lasers, photonics, environmental monitoring, remote sensing,

1. INTRODUCTION

Photonics integrated circuit (PIC) technology has seen significant investment from the communications and data center industries. As a result, a highly functional set of photonic components exist which can find use in a much wider set of applications like automotive sensors, medical devices, defense and science instrumentation. NASA's desire for small, lightweight, rugged, efficient and highly functional optical sensors makes PIC technology an excellent choice for the next generation of hardware. NASA is working with several partners on developing integrated photonics technology for future space missions [1-5].

Goddard Space Flight Center has spent several years developing an atmospheric carbon dioxide (CO₂) sensor based on laser absorption spectroscopy that uses a tunable laser to scan through a CO₂ gas absorption line centered at 1572 nm [6-9]. The current laser transmitter implementation uses mature technologies and meets all the optical performance requirements [10] but is relatively bulky and inefficient compared to an integrated photonic solution. UCSB and GSFC have initiated a program to replace the tunable seed laser with a PIC version to significantly improve the implementation for a resource constrained space-flight mission platform.

We expect to improve the implementation of this particular application and demonstrate the efficacy of the technology for an array of future applications.

2. DESIGN AND RESULTS

The seed laser being developed is a pulsed laser with tunable wavelength output. Consecutive pulses are emitted at different wavelengths that step across the absorption feature of interest. The wavelength of each pulse is individually locked to an exact value. This is achieved by using a master laser locked to the center of the CO₂ absorption as an absolute reference and using offset locking to tune a slave laser by means of an optical phase-locked loop (OPLL). Details on the previous wavelength tuning and locking techniques can be found in [11, 12]. The requirements for the laser seed system are tabulated below:

TABLE 1: Target performance for laser output

Parameter	Value
Center wavelength	1572.3 nm
Pulse Width	1 μ s
Repetition rate	7.5 KHz
Pulse modulation extinction	35 dB
Optical power (peak)	10 mW
Polarization (linear) extinction	20 dB
SMSR	40 dB
Linewidth (over 1 μ s)	<50MHz
Center wavelength drift (over 1s)	< 100 MHz
Standard deviation of center wavelength	<3 MHz
Wavelength tuning	\pm 15 GHz

The photonics block diagram for achieving this functionality is shown in Figure 1. The main integrated design elements include a distributed feedback (DFB) master laser diode, a phase modulator, a sampled grating distributed Bragg reflector (SG-DBR) slave laser diode, a Mach-Zehnder modulator (MZM), a semiconductor optical amplifier (SOA), and a high-speed photodiode. The DFB frequency is stabilized to a reference CO₂ gas cell using a frequency modulation technique. The frequency of the DFB is modulated using the integrated phase modulator. Closely integrated electronic circuitry will then generate a frequency discriminating error signal

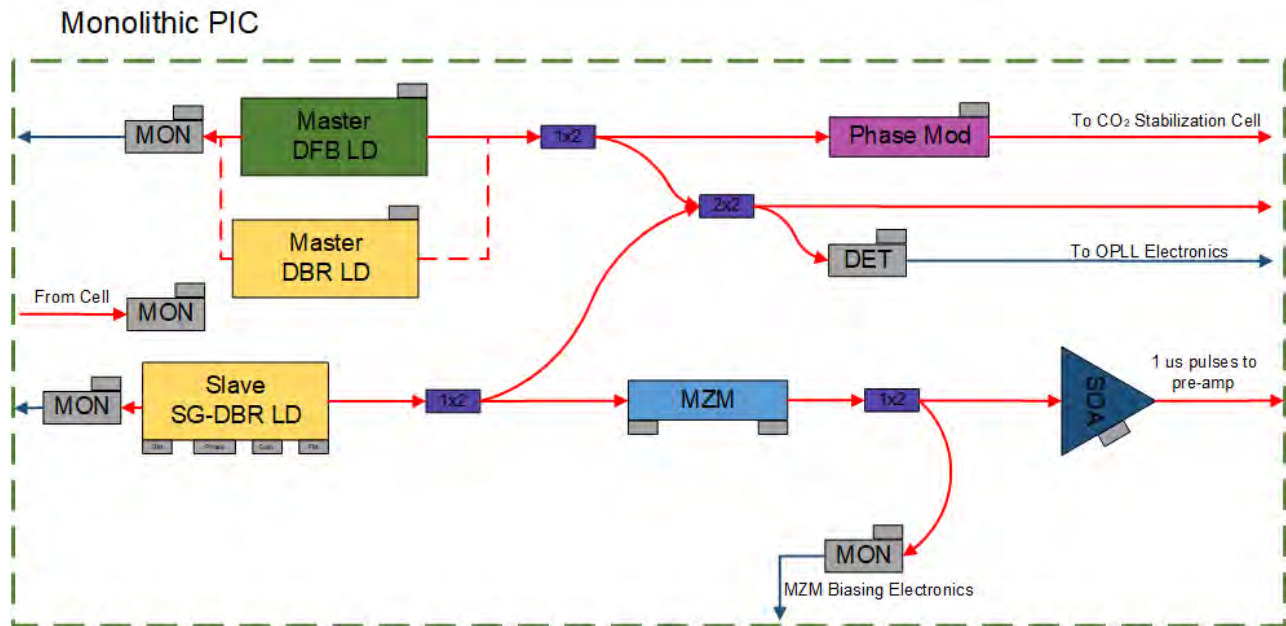


Figure 1 – PIC functional block diagram illustrating the components integrated onto a single photonic chip.

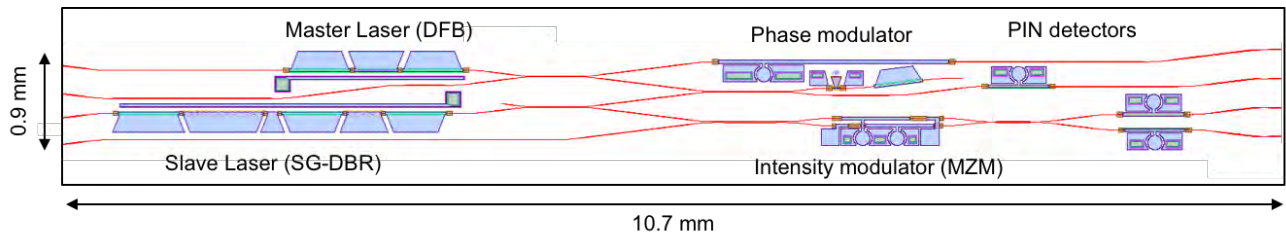


Figure 2 – PIC design layout

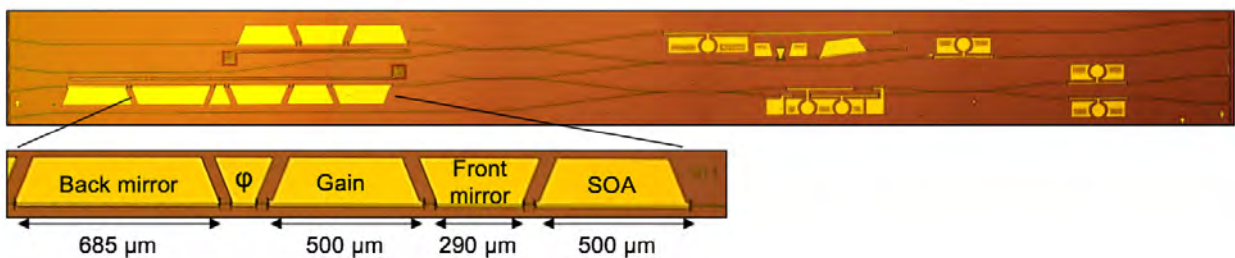


Figure 3 – Image of fabricated PIC with zoomed in SG-DBR laser section.

which is fed back into the DFB. The DFB itself is driven with low noise bias circuitry and the temperature is controlled using a thermo-electric-cooler (TEC). The widely-tunable, integrated SG-DBR is stepped across the absorption line feature at selective wavelengths using an OPLL offset-locking scheme. This offset-locking scheme is facilitated using the integrated high-speed photodetector which detects a beat note between the

master and slave lasers. OPLL circuitry feeds back an error signal to ensure the offset frequency maintains the frequency stability characteristics of the master laser. Additional circuitry will drive the SOA for lidar pulse carving and amplification. The MZM offers an alternative for pulse carving.

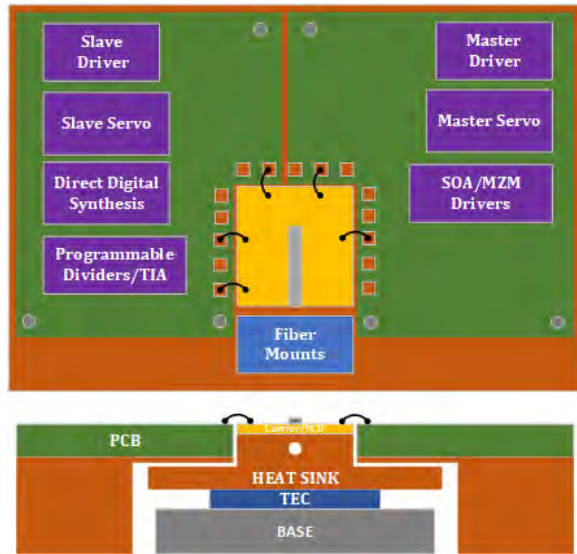


Figure 4 – Electrical and Photonic package design. The PIC is the gray rectangle mounted in the middle of the gold carrier. The carrier is cooled through TEC and heatsink and is wire bonded to the printed circuit boards (PCBs).

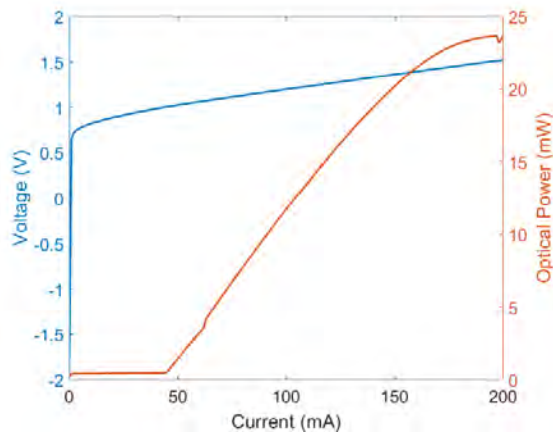


Figure 5 –Light-Current-Voltage (LIV) characteristics of integrated tunable laser from completed PIC

To realize the true potential of integrated photonics, close integration of the PIC with electronics is desirable. This makes the entire package smaller, lighter and more rugged and reduces losses due to transmission of high-speed electrical signals. A block diagram of the system design with closely integrated electronic PCBs is shown in Figure 4.

UCSB has completed fabrication of the designed photonic circuits and begun characterizing the performance. A sample PIC is shown in Figure 3. Figure 5 shows the light-current-voltage (LIV) characteristics of a tunable SG-DBR laser from the fabrication. The results to date are promising and we will show further test data of the PIC in the future.

3. CONCLUSIONS

We have demonstrated promising results on an integrated photonic circuit implementation for wavelength-tunable, amplitude-modulated laser system. This work shows the potential for orders of magnitude improvement in volume and mass while improving efficiency, ruggedness and reliability. The technology and component performance continues to improve rapidly due to increased investment from communications and data center applications. Space flight and other remote sensing applications can benefit significantly from the application of integrated photonics technology.

ACKNOWLEDGMENTS

The authors gratefully acknowledge funding from NASA's Earth Science Technology Office (ESTO) Advanced Component Technology (ACT) program.

6. REFERENCES

- [1] Krainak, M. A., Stephen, M. A., Troupaki, E., Tedder, S. A., Reyna, B., Bergman, K., Lipson, M., Rizzo, A. J., Datta, I., Abrams, N. C., Klamkin, J., Zhao, H., Song, B., Ho, S. T., Bei, Q., Huang, Y., Tu, Y., Moslehi, B., Harris, J., Matsko, A. B., Savchenkov, A., Liu, G., Proietti, R., Ben Yoo, S. J., Johansson, L., Dorrer, C., Qiao, J. X., Gong, S., Gu, T., Ohanian, O. S., Tran, M., Bowers, J. E., Ni, X., Ding, Y., Duan, Y., Dalir, H., Chen, R. T., Sorger, V. J., Komljenovic, T., Mookherjee, S., Wang, X., "Integrated photonics for NASA applications," SPIE: Photonics West 2019: 10899-14, 2019
- [2] H. Zhao, S. Pinna, B. Song, L. Megalini, S. T. Suran Brunelli, L. Coldren, J. Klamkin, "Indium Phosphide Photonic Integrated Circuits for Free Space Optical Links," IEEE Journal of Selected Topics in Quantum Electronics, vol. 24, no. 6, 2018.
- [3] H. Zhao, S. Pinna, B. Song, L. Megalini, S. T. Suran Brunelli, L. Coldren, J. Klamkin, "Integrated Indium Phosphide Transmitter for Free Space Optical Link," Integrated Photonics Research, Silicon and Nanophotonics Conference, paper ITu4B.6, 2018.
- [4] J. Klamkin, H. Zhao, B. Song, Y. Liu, B. Isaac, S. Pinna, F. Sang, L. Coldren, "Indium Phosphide Photonic Integrated Circuits: Technology and Applications," IEEE BiCMOS and Compound Semiconductor Integrated Circuits and Technology Symposium, 2018.
- [5] J. Fridlander, S. Pinna, V. Rosborough, S. Estrella, L. Johansson, J. Klamkin, "RZ-DPSK Photonic Integrated Transmitter for Space Optical Communications," Proc. SPIE vol. 10524, 2018.
- [6] Active Sensing of CO₂ Emissions over Nights, Days, and Seasons (ASCENDS) Mission, Science Mission Definition Study 2015, ASCENDS Ad Hoc Science Definition Team, April 15, 2015,

http://cce.nasa.gov/ascends_2015/ASCENDS_FinalDraft_4_27_15.pdf

[7] Kawa, S. R., J. Mao, J. B. Abshire, G. J. Collatz, X. Sun, and C. J. Weaver, "Simulation studies for a space-based CO₂ lidar mission," *Tellus B*, 62, 759–769, doi:10.1111/j.1600-0889.2010.00486.x, 2010.

[8] Earth Science and Applications from Space: National Imperatives for the Next Decade and Beyond Committee on Earth Science and Applications from Space: A Community Assessment and Strategy for the Future, National Research Council, ISBN: 0-309-66714-3, 456 pages, 2007, <http://www.nap.edu/catalog/11820.html>

[9] Abshire, J. B., Ramanathan, A., Riris, H., Allan, G. R., Sun, X., Hasselbrack, W. E., Mao, J., Wu, S., Chen, J., Numata, K., Kawa, S. R., Yang, M. Y., and DiGangi, J., "Airborne Measurements of CO₂ Column Concentrations made with a Pulsed IPDA Lidar using a Multiple-Wavelength-Locked Laser and HgCdTe APD Detector," *Atmos. Meas. Tech.*, 11, 2001–2025, 2018.

<https://doi.org/10.5194/amt-11-2001-2018>

[10] A. Yu, J. Abshire, M. Stephen, J. Chen, S. Wu, B. Gonzalez, L. Han, K. Numata, G. Allan, W. Hasselbrack, J. Nicholson, M. Yan, P. Wisk, A. DeSantolo, B. Mangan, G. Puc, D. Engin, B. Mathason, and M. Storm, "Fiber-Based Laser Transmitter Technology at 1.57 μm for Atmospheric Carbon Dioxide Satellite Remote Sensing," in *Advanced Solid State Lasers, OSA Technical Digest (online)* (Optical Society of America, 2015), paper AT1A.1.

[11] K. Numata, J. R. Chen, and S. T. Wu, "Precision and fast wavelength tuning of a dynamically phase-locked widely-tunable laser," *Opt. Express* 20, 14234-14243 (2012).

[12] K. Numata, J. R. Chen, S. T. Wu, J. B. Abshire, and M. A. Krainak, "Frequency stabilization of distributed-feedback laser diodes at 1572 nm for lidar measurements of atmospheric carbon dioxide," *Appl. Opt.* 50, 1047-1056 (2011).

Power Optimization for Datacenter Optical Transmitters

Sergio Pinna, Sarvagya Dwivedi, Larry A. Coldren, Clint Schow, Jonathan Klamkin

Electrical and Computer Engineering Department, University of California Santa Barbara, Santa Barbara, CA 93106, USA
pinna@ece.ucsb.edu

Abstract: Power allocation is investigated for a non-repeated/non-amplified datacenter network scenario. A mathematical model is constructed for the optical eye amplitude in a power constrained case, and the effectiveness of the model is demonstrated experimentally. © 2019 The Author(s)
OCIS codes:060.2330, 060.1155, 060.4256, 060.4250, 060.2360

1. Introduction

Mega datacenters are fundamental for an increasing number of services. These include cloud-based data storage, high performance computing, video streaming etc. Thus resulting in a relevant energy footprint, with an estimated energy consumption in the United States of 70 billion kWh in 2014, approximately 1.8% of the total national electricity consumption [1], estimated to reach 13% of the world energy consumption by 2030 [2]. Of those, approximately 15% (more than 10 billion kWh in 2014) consumed by the network equipment [3]. Many efforts, are directed to lower the power requirement of the physical level network components [4]. Most studies, however, focuses on the efficiency of the overall network architecture, or at improving individual optical components.

Here beginning with the assumption of limited total available power, we analyze how different power allocation strategies affect the performance of an externally modulated intensity modulated direct detection (IM-DD) link. We first define the mathematical transmitter model and estimate the link performance. We then compare the analytical results with the experimental bit error rate (BER) measurements. The optimal power allocation is found to be of 2/3 of the power to the laser source and 1/3 to the electrical data signal.

2. Model and measurements

Fig.1(a) sketches the network scenario. The transmitter, is composed of a laser source externally modulated by a Mach-Zehnder modulator (MZM), connected through a passive optical link to the receiver. The power dissipated by the link equals the electrical power dissipated by the laser plus the power required to drive the modulator. A laser wall-plug efficiency of $\eta=20\%$ is assumed, the MZM half wave voltage (V_π), insertion loss (IL), and input impedance (Z) are 5V, 6dB, and 30Ω , respectively. The amplitude ΔP of the optical modulated signal (see Fig. 1(a)), defined as the power difference between the logic zero (P_0) and one (P_1), can be calculated, neglecting noise contributions as in Eq. 1, where P_{laser} is the wall plug power dissipated by the laser, V_0 and V_1 are, respectively, the digital zero and one electrical amplitudes, assumed bipolar (i.e. $V_0=-V_1$), and V_b is the modulator bias voltage.

$$\Delta P = P_1 - P_0 = 10^{IL/10} \eta P_{laser} \left(\cos\left(\frac{2\pi(V_1 + V_b)}{V_\pi}\right) - \cos\left(\frac{2\pi(V_0 + V_b)}{V_\pi}\right) \right) \quad (1)$$

The bias voltage, which maximizes the MZM electro-optical conversion, is found by maximizing the derivative of the MZM transfer function with respect to V_b . The point of maximum slope corresponds to the MZM quadrature point ($V_b=V_\pi/2$). Using the small signal approximation, and defining $V_s=|V_1-V_0| \ll V_\pi$, Eq. 1 can be written as:

$$\Delta P = k P_{laser} \left[\frac{2\pi V_s}{V_\pi} \right] \longrightarrow \Delta P = k P_{laser} \left[\frac{2\pi \sqrt{Z(P_{tot} - P_{laser})}}{V_\pi} \right] \quad (2)$$

where $k=\eta 10^{IL/10}$. $P_{tot}=P_{laser}+P_s$ is the total available power, and $P_s=V_s^2/Z$. From Eq. 2, the ΔP is linearly proportional both to the laser power and the electrical signal amplitude. Therefore, to double ΔP , it is possible either to double P_{laser} , or V_s , leading in the second case to a four-fold increase in the signal power required. Maximizing

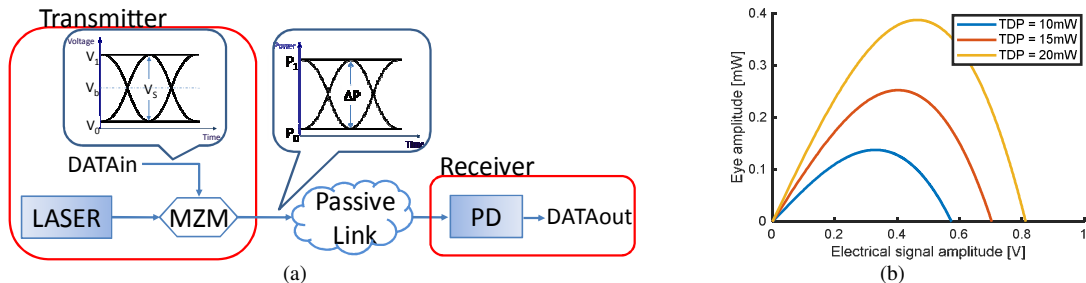


Fig. 1: (a) Network scenario considered in the model, MZM: Mach-Zehnder modulator, PD: photodetector. (b) Simulation of the optical eye diagram amplitude as a function of the electrical signal amplitude for different TDP levels (total dissipated power).

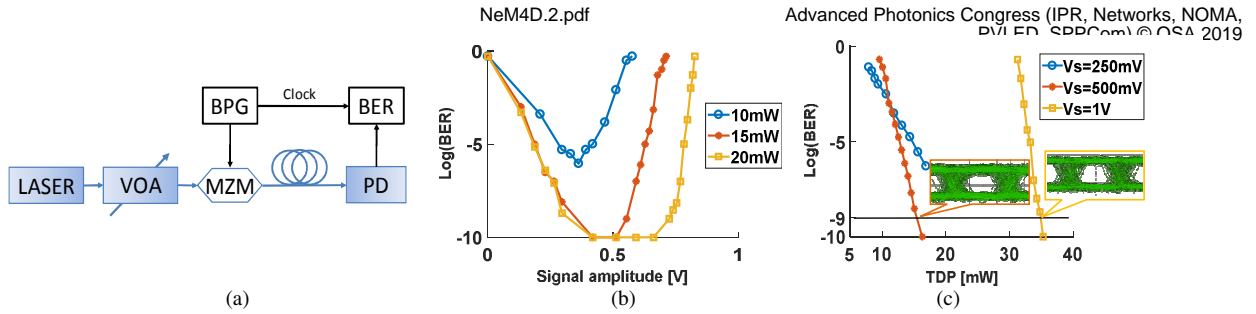


Fig. 2: (a) Test optical link, VOA: variable optical attenuator, BPG: bit pattern generator, BER: bit error rate tester. (b) measured BER as a function of the electrical driving voltage for different TDP values. (c) Measured BER different values of the driving signal amplitude.

Eq. 2 with respect to P_{laser} , the optimal strategy for low available power condition is to allocate $2/3$ of P_{tot} to the laser and $1/3$ to the electrical data signal. It's important to notice that the modulator parameters do not affect the power allocation strategy. Fig. 1(b) shows the simulated eye amplitude as a function of V_s for different values of the total dissipated power (TDP). As shown, if V_s is small, the optical eye amplitude is also small; negligible modulation depth, almost all the power is allocated to the optical source. As V_s increases, ΔP also increases, even if with a reduced extinction ratio (ER). The maximum ΔP is reached for $V_s = \sqrt{ZP_{tot}/3}$. Further increasing V_s results in an increase of the optical ER, however, the consequent reduction of the laser power leads to a reduction of ΔP .

If the small signal approximation doesn't hold, more power must be allocated to the laser source. As a limit, as the optimal electrical signal reaches $V_s = V_\pi$, the total amount of excess power must be allocated to the laser.

To validate the theoretical model, a 10 Gb/s optical link has been tested (Fig. 2(a)). The link operates at a wavelength of 1550 nm, the MZM has a $V_\pi = 5$ V, $IL = 6$ dB, and $V_b = V_\pi/2$. A bit pattern generator (BPG) drives the MZM with a signal amplitude between $0.2 V_{pp}$ to $2 V_{pp}$. The laser optical power was varied through a variable optical attenuator. At the receiver, a 12.5 GHz bandwidth photodetector is directly connected to the BER analyzer. Fig. 2(b) reports the BER measurements as a function of the driving voltage for three different total available power levels (10mW, 15mW, and 20mW), the optical power has been varied consequently. When the whole power is allocated to the laser (0 V signal amplitude), the optical eye diagram is completely closed (absence of modulation). BER=0.5. The same happens when the total power is allocated to the electrical signal; in this case the laser power is zero and no optical signal is present. Increasing the driving voltage from zero, the eye diagram rapidly opens and consequently the BER drops. When the power allocated to the electrical signal reaches $1/3$ of the total available power, ΔP reaches its maximum and consequently the BER reaches its minimum. For the 10mW the minimum BER (equal to $4e-6$) is reached for an electrical signal amplitude of 0.37 mV. In this case, the total allocated power is not sufficient to meet the receiver sensitivity and for this reason error free operation is not reached. Also, for the 15mW and 20mW cases it is possible to see that as the minimum of the measurable BER ($1e-10$ for our instrument) is reached for approximately 60% of the maximum voltage swing, thus demonstrating the theoretical prediction.

From a different perspective, Fig. 2(c) shows the BER measurements performed with a constant signal amplitude, for the cases of 250mV, 500mV, and 1V. With 1V (yellow curve), the error free (EF) condition is reached at approximately TDP = 37mW where $P_s = 33$ mW and $P_{laser} = 4$ mW. Reducing P_s to 500mV (orange curve), EF can be reached with a TDP of approximately 16mW, where $P_s = 8$ mW and $P_{laser} = 8$ mW. The insets of Fig.2(c) show the 10mV amplitude eye diagrams at BER= $1e-9$ where the reduced modulation depth is associated with the reduced driving voltage that fully recovered by the increased laser power.

3. Conclusions

In this paper, the power allocation for an energy constrained optical link has been reported. The model predicts that an optimized link allocates $2/3$ of the power to the laser source and $1/3$ of the power to the electrical data signal. The theoretical model has been compared with experimental BER measurements performed on a 10 Gb/s link.

Acknowledgements

The information, data, or work presented herein was funded in part by the Advanced Research Projects Agency-Energy (ARPA-E), U.S. Department of Energy, under Award Number DE-AR0000848. The views and opinions of authors expressed herein do not necessarily reflect those of the United States Government or any agency thereof.

4. References

- [1] Shehabi, A., et al. (2016). United States Data Center Energy Usage Report: LBNL Report #: LBNL-1005775.
- [2] Andrae, ASG, and Edler, T. "On global electricity usage of communication technology: trends to 2030." *Challenges* 6.1 (2015): 117-157.
- [3] Greenberg, A., et al. "The cost of a cloud: research problems in data center networks." *ACM SIGCOMM* Vol. 39, no. 1 p. 68-73 (2008).
- [4] Hiraki, T, et al. "Heterogeneously integrated iii-v/Si MOS capacitor Mach-Zehnder modulator." *Nature Photonics* 11.8 (2017): 482.

Monolithic Integration of Widely-Tunable DBR and DFB Lasers with One-Step Grating Formation

Victoria Rosborough¹, Fengqiao Sang¹, Joseph Fridlander¹, Hongwei Zhao¹, Bowen Song¹, Simone Tommaso Suran Brunelli¹, Jeffrey. R. Chen², Mark A. Stephen², Larry Coldren¹ and Jonathan Klamkin¹

¹Electrical and Computer Engineering Department, University of California, Santa Barbara, CA 93106, USA

²NASA Goddard Space Flight Center, Greenbelt, MD 20771, USA

rosborough@ucsb.edu

Abstract: We demonstrate the integration of widely-tunable sampled-grating DBR (SGDBR) and DFB lasers on indium phosphide. The SGDBR laser exhibits a 36-nm tuning range with ≥ 36 -dB SMSR and the DFB laser an SMSR of 51.6 dB. © 2019 The Author(s)

OCIS codes: (130.3120) Integrated optics devices; (140.5960) Semiconductor lasers; (050.2770) Gratings

1. Introduction

The complexity of indium phosphide (InP) based photonic integrated circuits (PICs) has increased in the past decade both in number of on-chip functions and functional complexity [1]. Multiple active and passive elements such as lasers, modulators, couplers, and photodetectors are fabricated in a single PIC for applications such as coherent transmitters and receivers, optical downconverters for microwave frequency generation, and LIDAR [1–3]. These PICs employ either sampled-grating distributed Bragg reflector (SGDBR) lasers for their wide tuning range or distributed feedback (DFB) lasers for their wavelength stability. In this work, we present a platform for integrating both SGDBR and DFB lasers on same substrate using a simplified fabrication process with a single grating lithography and etch step.

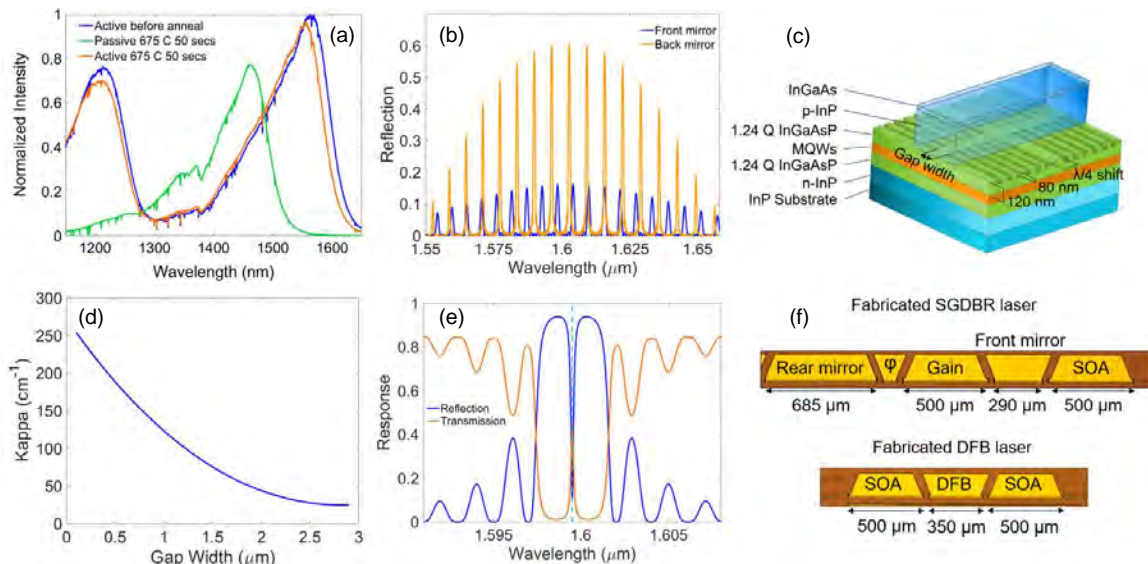


Fig. 1. (a) Photoluminescence intensity curves showing a 100 nm blueshift in the quantum well band edge after implantation and annealing. (b) Calculated rear and front mirror reflectivity for the SGDBR laser using an 80 nm etch depth into the top waveguide layer for the gratings. (c) Schematic of the DFB laser structure showing the vertically etched Bragg grating with a central gap. (d) Grating coupling coefficient (κ) as a function of gap width. (e) Calculated grating response of a 350 μm -long quarter-wave-shifted DFB laser with a 1- μm gap width. (f) Optical micrographs of fabricated SGDBR and DFB lasers.

2. Design and Fabrication

Active/passive integration was achieved with a quantum well intermixing (QWI) process. Ion implantation into a sacrificial cap layer created vacancies that diffused into the quantum wells when annealed, resulting in a blueshift of the quantum well band edge [4]. Figure 1(a) shows a 100-nm shift in the band edge of implanted sections after

annealing as measured by photoluminescence. The QWI approach was chosen for the ability to integrate DFB lasers without the specialized regrowth techniques required for butt-joint regrowth or selective area growth.

Figure 1(b) shows the calculated reflection of the rear and front SGDBR mirrors for an 80-nm grating etch depth. To achieve a lower coupling coefficient, κ , for the DFB lasers, a central gap was introduced into the vertically etched gratings as illustrated in Fig. 1(c). This lower κ design reduces fabrication time and improves process reliability by allowing the use of a single etch depth for both the SGDBR and DFB laser mirror gratings. The grating coupling coefficient as a function of the gap width is plotted in Fig. 1(d). Figure 1(e) shows the calculated response of a quarter-wave-shifted DFB grating with a 1 μm gap. Optical micrographs of fabricated SGDBR and DFB lasers are shown in Fig. 1(f).

3. Characterization

Figures 2(a) and (b) show the light-current-voltage (LIV) characteristics of the SGDBR and DFB laser, respectively. The optical power was measured by an on-chip detector following each laser. The SGDBR laser outputs 6 mW at 200 mA and has a threshold current of 30 mA. The jump in output power near 100 mA is due to a cavity mode hop. The DFB laser outputs 5 mW from a single end at 150 mA and has a threshold current of 30 mA. As shown in Fig. 2(c), the SGDBR laser exhibits a 36 nm tuning range. The side mode suppression ratio (SMSR) was greater than 36 dB over the entire tuning range with a maximum SMSR of 46.2 dB at 1580.5 nm. Figure 2(d) shows single-mode operation of the DFB laser at 1605 nm with an SMSR of 51.6 dB.

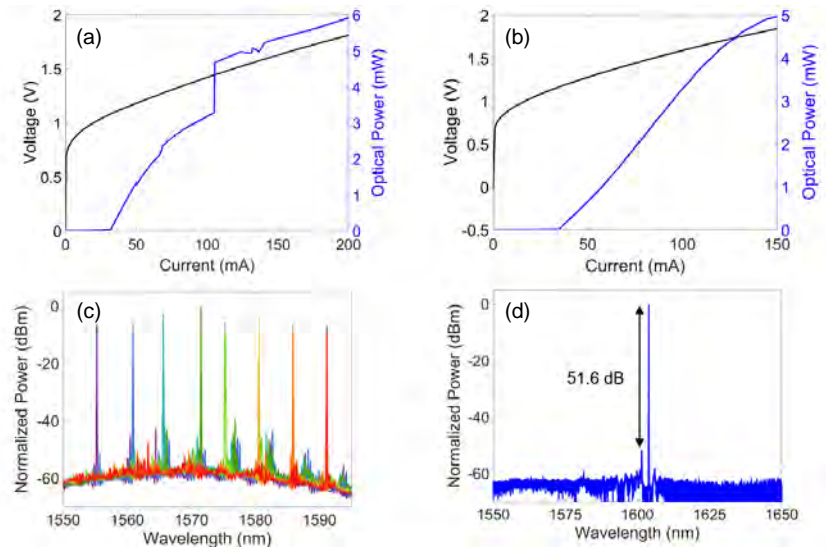


Fig. 2. LIV characteristic of (a) an SGDBR laser and (b) a DFB laser. (c) Superimposed output spectra of the SGDBR laser showing 36-nm tuning range. (d) DFB lasing spectrum with SMSR of 51.6 dB.

4. Conclusion

To the best of the authors' knowledge, we have presented the first monolithic integration of a widely-tunable SGDBR laser with a DFB laser on InP. Future PIC designs will take advantage of an SGDBR laser source for wide-tunability along with a DFB laser for wavelength stability.

5. Acknowledgements

The authors acknowledge NASA for support through the ROSES Advanced Component Technology grant.

6. References

- [1] S. Arafin and L. A. Coldren, "Advanced InP Photonic Integrated Circuits for Communication and Sensing," *IEEE JSTQE* **24**(1) (2018).
- [2] F. Kish, et al., "System-on-Chip Photonic Integrated Circuits," *IEEE JSTQE* **24**(1) (2018).
- [3] B. Isaac, et al., "Indium Phosphide Photonic Integrated Circuit Transmitter with Integrated Linewidth Narrowing for Laser Communications and Sensing," 2018 IEEE International Semiconductor Laser Conference (ISLC).
- [4] E. J. Skogen, et al., "A Quantum-Well-Intermixing Process for Wavelength-Agile Photonic Integrated Circuits," *IEEE JSTQE* **8**(4) (2002).

High Power Indium Phosphide Photonic Integrated Circuit for Pulse Position Modulation Free Space Optical Communications

Hongwei Zhao
Electrical and Computer
Engineering Department
University of California Santa
Barbara
Santa Barbara, USA
hwzhao@ece.ucsb.edu

Sergio Pinna
Electrical and Computer
Engineering Department
University of California Santa
Barbara
Santa Barbara, USA
pinna@ece.ucsb.edu

Fengqiao Sang
Electrical and Computer
Engineering Department
University of California Santa
Barbara
Santa Barbara, USA
fsang@ece.ucsb.edu

Simone Tommaso Suran Brunelli
Electrical and Computer
Engineering Department
University of California Santa
Barbara
Santa Barbara, USA
ssuranbrunelli@ucsb.edu

Larry A. Coldren
Electrical and Computer
Engineering Department
University of California Santa
Barbara
Santa Barbara, USA
coldren@ece.ucsb.edu

Jonathan Klamkin
Electrical and Computer
Engineering Department
University of California Santa
Barbara
Santa Barbara
klamkin@ece.ucsb.edu

Abstract— In this work, a high-power indium phosphide photonic integrated circuit was investigated for pulse position modulation free space optical communications. The integrated transmitter was fabricated with a novel high-power platform. 16-ary pulse position modulation was demonstrated at a data rate of 1.25 Gbps with an extinction ratio of 9.6 dB.

Keywords—Photonic integrated circuits, indium phosphide, free space communications, pulse position modulation

I. INTRODUCTION

Free space communications have been deployed by radio frequency (RF) technologies. Due to huge data traffic caused by high-speed Internet, multimedia services and Internet of things (IoT), the conventional RF band has been congested. One promising solution is to use optical carriers in the visible and infrared spectrum. Compared with RF techniques, free space optical communications support higher data rate and better security with less power and mass requirements [1, 2].

Indium phosphide (InP) photonic integrated circuits (PICs) can enable single-chip implementation of complex functionalities with significantly lower cost, size, weight and power consumption (CSWaP), therefore, are desirable for free space communication that requires CSWaP while demonstrating high output optical power and power-efficient modulation formats [3-6]. A novel platform for high optical power InP PICs was demonstrated in our previous work [7]. This platform is capable of a record output power of nearly 250

mW, which is significantly higher than conventional PIC platforms, reducing the requirements on a high-power booster amplifier and enabling certain links without the need for an amplifier [8].

Pulse position modulation (PPM) is a power-efficient modulation format, which is preferred for free space communications [9]. In this work, an InP transmitter based on a novel high-power PIC platform was characterized for 16-PPM, demonstrating a data rate of 1.25 Gbps with an extinction ratio of 9.6 dB.

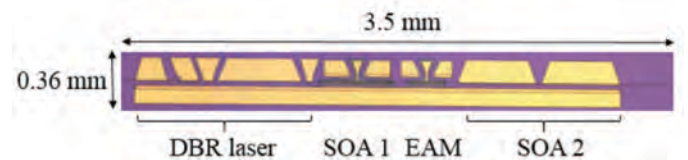


Fig. 1. Microscope image of fabricated PIC transmitter consisting of a DBR laser, a high-speed SOA (SOA 1), and EAM and a high-power two-section output booster SOA (SOA 2).

II. INDIUM PHOSPHIDE TRANSMITTER

The microscope image of the fabricated PIC transmitter is shown in Fig. 1. The PIC transmitter consists of a distributed Bragg reflector (DBR) laser, a high-speed semiconductor optical amplifier (SOA), an electro absorption modulator (EAM), and a two-section high-power output booster SOA. The active/passive integration was realized with the quantum

well intermixing technique. The footprint of the PIC is $3.5 \text{ mm} \times 0.36 \text{ mm}$. The lengths of SOA 1 and EAM are $500 \text{ }\mu\text{m}$ and $250 \text{ }\mu\text{m}$, respectively. SOA 1 can be used as a forward-biased modulator, which is based on current injection induced index change. The SOA modulation bandwidth is smaller compared to reverse-biased EAM.

The PIC transmitter was fabricated based on a novel epitaxial structure designed for high optical power. The epitaxial layers are shown in Fig. 2. Compared with conventional epitaxial design, a low-index 1.03 Q waveguide layer (WG 2) was added below the primary guiding structure. This novel design enables large modal area in SOA, thus increasing the output saturation power of SOA [7].



Fig. 2. Epitaxial structure of the InP-based transmitter with a low-index dilute waveguide (1.03 Q).

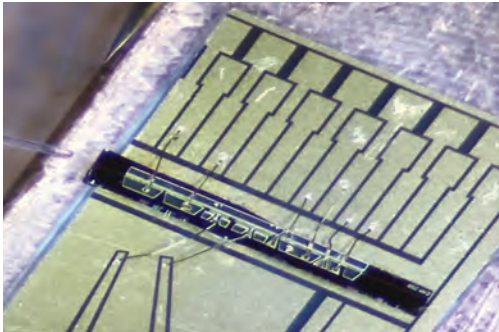


Fig. 3. A PIC transmitter that was mounted on a ceramic carrier .

The fabrication process was discussed in our previous work [7]. As shown in Fig. 3, the fabricated PIC transmitter was mounted on a ceramic carrier to test the RF performance. The P metal of SOA 1 and EAM were wire bonded to two 50-ohm RF feeding transmission lines. Then the device submount was fixed to a temperature-controller stage at 15°C .

III. PULSE POSITION MODULATION

Most common modulation formats such as on-off keying (OOK), phase shift keying (PSK), differential phase shift keying (DPSK) and pulse position modulation (PPM) can be used for free space communications. Among them, OOK is widely used since it requires relatively simple transmitter and receiver hardware. PPM is preferred to improve power

efficiency and receiver sensitivity and it can use the same transmitter and receiver hardware used for OOK [1].

Figure 4 compares OOK and PPM modulation. OOK is a simple two-level amplitude modulation format. Suppose the probability of '1' and '0' bit is equal, the peak optical power is twice the average power. Figure 5 shows the eye diagrams with non-return-to-zero (NRZ) OOK modulation. As expected, EAM demonstrates higher bandwidth than SOA 1.

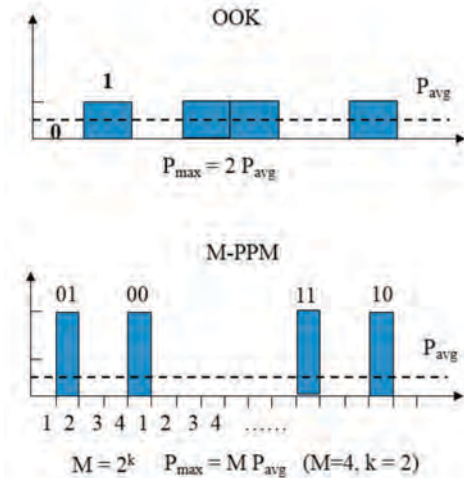


Fig. 4. Comparison of OOK and PPM.

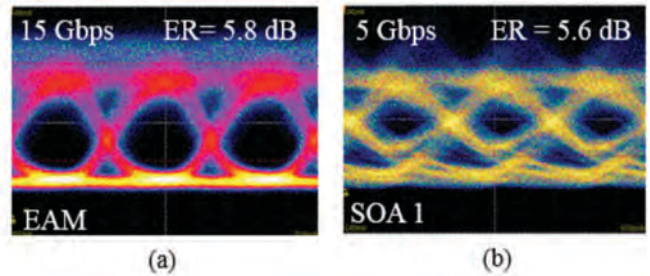


Fig. 5. Eye diagrams for OOK modulation. (a) EAM was modulated at 15 Gbps; (b) SOA 1 was modulated at 5 Gbps.

In M-PPM signals, the information is encoded by the time position of an optical pulse within symbol time slot. Then the duty cycle is $(1/M) \times 100\%$. For k bits of information, the number of time slots (M) is given by 2^k . The peak optical power is then M times of the average power.

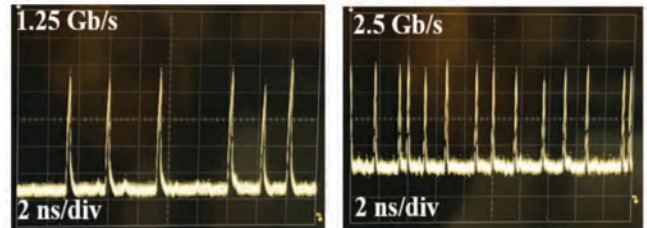


Fig. 6. 16-PPM output optical signals.

The schematic of the setup used to test the PIC for PPM is shown in Fig. 8. The RF signal was equally split into two; each was connected to a delay line (DL), then into a bias Tee. Firstly, the only EAM was driven with 16-PPM signals. The corresponding peak power is 16 times the average power. If the pulse bandwidth is f (Hz), the pulse width is $1/f$ (s). The bit rate (BR) is given by:

$$BR = \frac{f}{2^k} \times k \quad (1)$$

Figure 6 demonstrates the output 16-PPM sequences from the InP transmitter at a driving bandwidth of 5 GHz and 10 GHz. The corresponding data rates are 1.25 Gbps and 2.5 Gbps, respectively. The pulses appear fairly equalized and undistorted. The eye diagrams at 250 Mbps and 1.25 Gbps are shown in Fig. 7, demonstrating extinction ratios of 6.1 dB and 5.3 dB.

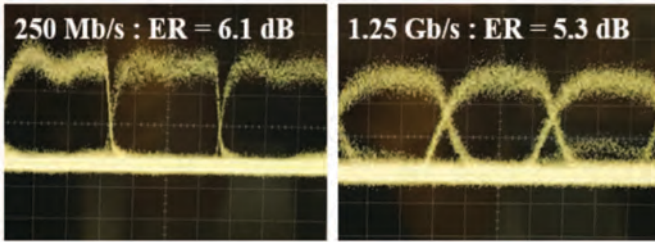


Fig. 7. Eye diagrams for 16-PPM with EAM modulated at a data rate of 250 Mbps and 1.25 Gbps.

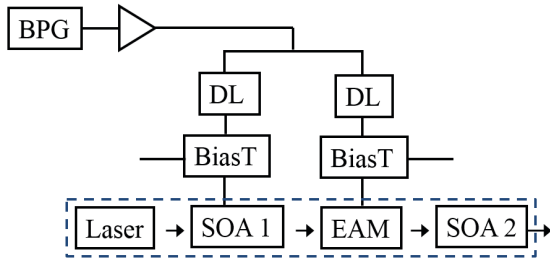


Fig. 8. Schematic of setup for PPM.

To improve the signal extinction ratio, the high-speed SOA and EAM can be driven simultaneously at lower data rates. SOA 1 and EAM were modulated by two phase-aligned 16-PPM signals. The eye diagrams at 250 Mbps and 1.25 Gbps are shown in Fig. 9. Compared to Fig. 6, the joint modulation of EAM and SOA 1 leads to an ER improvement above 3 dB. The modulation speed is limited by the forward biased SOA,

however the increased extinction ratio is preferred in low symbol rate applications.

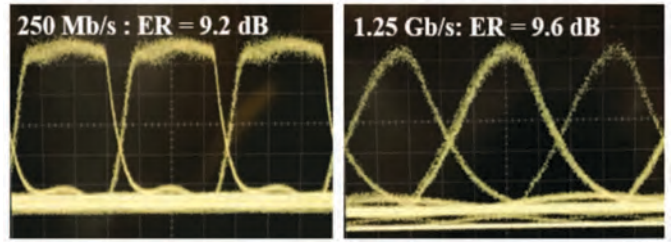


Fig. 9. Eye diagrams for 16-PPM with SOA 1 and EAM simultaneously modulated at a data rate of 250 Mbps and 1.25 Gbps.

IV. CONCLUSION

An InP PIC transmitter based on a novel high-power platform was investigated for free space communications. 16-PPM was demonstrated at a data rate of 1.25 Gbps with an extinction ratio of 9.6 dB.

REFERENCES

- [1] D. O. Caplan, "Laser communication transmitter and receiver design," *J. of Optical and Fiber Communications Reports*, vol. 4, pp. 225-362, 2007.
- [2] H. Kaushal and G. Kaddoum, "Optical Communication in Space: Challenges and Mitigation Techniques," in *IEEE Communications Surveys & Tutorials*, vol. 19, no. 1, pp. 57-96.
- [3] L. A. Coldren, S. C. Nicholes, L. Johansson, S. Ristic, R. S. Guzzon, E. J. Norberg, and U. Krishnamachari, "High performance InP-based photonic ICs—A tutorial," *Journal of Lightwave Technology*, vol. 29, no. 4, pp.554-570, 2011.
- [4] D. F. Welch et al., "Large-scale InP photonic integrated circuits: Enabling efficient scaling of optical transport networks," *IEEE J. Sel. Top. Quantum Electron.*, vol. 13, no. 1, pp. 22–31, Jan./Feb. 2007.
- [5] H. Zhao, S. Pinna, B. Song, L. Megalini, S. T. Šuran Brunelli, L. A. Coldren, and J. Klamkin, "Indium Phosphide Photonic Integrated Circuits for Free Space Optical Links," in *IEEE Journal of Selected Topics in Quantum Electronics*, vol. 24, no. 6, pp. 1-6, Nov.-Dec. 2018.
- [6] J. Fridlander, V. Rosborough, F. Sang, S. Pinna, S. Estrella, L. Johansson, and J. Klamkin. "High-speed RZ-DPSK photonic integrated transmitter for space optical communications." In *Laser Communication and Propagation through the Atmosphere and Oceans VIII*, vol. 11133, paper 1113309, 2019.
- [7] H. Zhao, S. Pinna, F. Sang, B. Song, S. T. Šuran Brunelli, L. A. Coldren, and J. Klamkin, "High-Power Indium Phosphide Photonic Integrated Circuits," in *IEEE Journal of Selected Topics in Quantum Electronics*, vol. 25, no. 6, pp. 1-10, Nov.-Dec. 2019.
- [8] H. Zhao, S. Pinna, F. Sang, S. T. Šuran Brunelli, L. A. Coldren, and J. Klamkin, "High power indium phosphide photonic integrated platform" Device Research Conference (DRC) 2019.
- [9] V. Rosborough, F. Gambini, J. Snyder, L. Johansson, and J. Klamkin, "Integrated Indium Phosphide Pulse Position Modulation Transmitter for Free Space Communications," in *Advanced Photonics 2016 (IPR, NOMA, Sensors, Networks, SPPCom, SOF)*, paper ITu2A.3.

Indium Phosphide Photonic Integrated Circuit Transceiver for FMCW LiDAR

Brandon J. Isaac¹, Bowen Song, Sergio Pinna, Larry A. Coldren², *Life Fellow, IEEE*,
and Jonathan Klamkin, *Senior Member, IEEE*

Abstract—We present a photonic integrated circuit (PIC) transceiver for frequency modulated continuous wave (FMCW) LiDAR applications. The transmitter consists of a widely tunable sampled grating distributed Bragg reflector laser (SGDBR) and a frequency discriminator which combines multimode interference couplers, a tunable asymmetric Mach–Zehnder Interferometer (a-MZI), and balanced photodiodes. The frequency discriminator converts frequency fluctuations of the laser to amplitude fluctuations of the photodiode currents. This provides an error signal for feedback into the laser cavity for frequency stabilization. Frequency modulation is obtained by a phase shifter in the a-MZI which tunes the quadrature point of the filter and the frequency where the error is zero. An on-chip receiver couples power from the transmitter to self-heterodyne with the time-delayed echo of a distant object. The generated beat frequency of the self-heterodyne measurement gives the echo signals time-of-flight to obtain the distance and velocity of the reflecting object. The theory of the components is described, and characterization of the transmitter and receiver is presented.

Index Terms—LiDAR, semiconductor lasers, photonics integrated circuits (PIC).

I. INTRODUCTION

TUNABLE lasers and photonic integrated circuits (PIC) have demonstrated performance improvements for several decades in the telecommunication industry enabling over 100 Gbps data rates [1]–[7]. Furthermore, advancements in silicon photonics have increasingly enabled integrated photonic platforms with high component density [4], [6], [7]. Beyond communication application, tunable lasers and PICs are enabling compact solutions for remote sensing, detection, and spectroscopy. Each individual application puts forth specific requirements on the PIC. Laser performance such as power output, linewidth, and tuning range become important parameters to optimize for the specific application. One emerging technology that can benefit from tunable lasers and photonic integration is

Light Detection and Ranging, or LiDAR. In contrast to RaDAR, LiDAR utilizes signals at optical frequencies which improves the spatial resolution of the imaging, opening possible solutions to autonomous driving, robotics, and terrain mapping. There are several approaches to LiDAR as discussed in refs. [8]–[10]. Photonic integration opens the possibility to reduce the system size, as a single chip can contain many of the necessary system elements such as acting as both a tunable light source and receiver.

Compared to standard pulsed techniques for LiDAR, frequency modulated continuous wave (FMCW) LiDAR has the benefit of low peak power, which makes it a good candidate to implement in semiconductor waveguides [11]–[14]. In this approach, the laser frequency is modulated with a triangular waveform, and split to serve as both an output signal to an optical phased array (OPA) and a reference for the detection. The OPA can provide 2D beam steering by utilizing phase shifters for steering along one direction, and frequency dispersion of the optical antenna for steering along the orthogonal direction [15]–[17]. The reflected echo signal couples back through the OPA to a receiver where it is mixed with the reference signal to generate the measurement result. The frequency modulation allows the time-of-flight to be determined by the beat frequency generated in the receiver. The echo signal frequency is offset from the reference by $\delta f = 2 \cdot (\Delta F/T) \cdot \delta t$, where ΔF is the total frequency modulation range, T is the period of the frequency modulation, and δt is the time-of-flight for the echo signal. The object distance can then be determined from $d = c \cdot (\delta t/2)$, where c is the speed of light. Using a triangular waveform, in contrast to a sawtooth waveform, allows both spatial and velocity information to be obtained as the object movement imparts a doppler shift to the echo signal frequency. The result is that the rising and falling portions of the waveform generate different beat frequencies which causes the peaks in the stationary frequency spectrum to be split by the doppler frequency $\delta f_D = 2f_0(\Delta v/c)$.

For the signal generation in a LiDAR system, indium phosphide (InP) provides mature PIC components and ability for active-passive integration to form an integrated transceiver [2], [5], [18]–[22]. This paper discusses the design and characterization of one such InP PIC transceiver which consists of a sampled grating distributed Bragg reflector (SGDBR) laser, a frequency discriminator based on an asymmetric Mach-Zehnder Interferometer (a-MZI) and balanced photodiodes (PD), and a receiver consisting of balanced PDs and couplers to mix the reference and echo signal. The paper is structured to first describe the

Manuscript received February 1, 2019; revised April 8, 2019; accepted April 10, 2019. Date of publication April 17, 2019; date of current version May 16, 2019. This work was supported in part by DARPA AFOSR Contract HR0011-16-C-0106 through a subcontract from Lockheed Martin. B. J. Isaac, supported by an NSF GRFP. (*Corresponding author: Brandon J. Isaac.*)

B. J. Isaac and L. A. Coldren are with the Materials Department, University of California, Santa Barbara, CA 93106 USA (e-mail: brandonjisaac@ucsb.edu; coldren@ece.ucsb.edu).

B. Song, S. Pinna, and J. Klamkin are with the Department of Electrical and Computer Engineering, University of California, Santa Barbara, CA 93106 USA (e-mail: bowen@ece.ucsb.edu; pinna@ece.ucsb.edu; klamkin@ece.ucsb.edu).

Color versions of one or more of the figures in this paper are available online at <http://ieeexplore.ieee.org>.

Digital Object Identifier 10.1109/JSTQE.2019.2911420

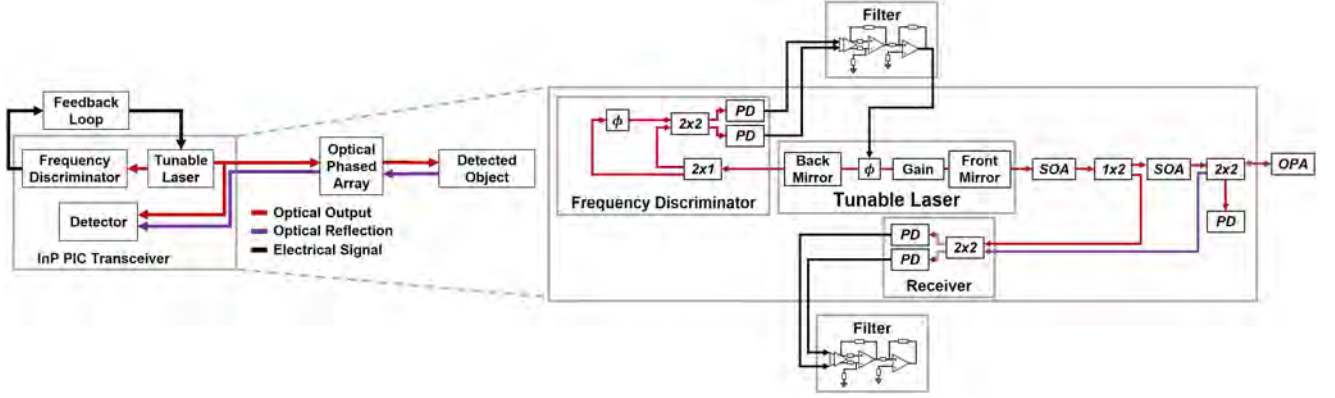


Fig. 1. Block diagram of the transceiver and OPA system (left). The tunable laser provides a signal for the OPA and on-chip frequency discriminator that drives an off-chip feedback circuit for frequency locking the laser. The detector utilizes tapped power from the tunable laser in a self-heterodyne measurement to convert object distance to a beat frequency as the tunable laser is frequency modulated. The expanded region (right) shows the transceiver PIC components including gain, phase, and mirrors of the laser; semiconductor optical amplifier (SOA); 1×2 and 2×2 splitters; phase shifters; and photodetectors (PD).

components of the PIC transmitter with details to elucidate design choices and tradeoffs that were considered, followed by a discussion of the fabrication and characterization of transceiver components

II. PIC OVERVIEW AND COMPONENT THEORY

A block diagram of the LiDAR system is shown in Fig. 1, along with a more detailed block diagram of the InP transceiver. The InP transceiver PIC can be coupled to an OPA which serves as the emitting and receiving aperture. The transmitter and receiver are discussed in further details below.

A. Transmitter

The transmitter consists of a widely tunable laser and a frequency discriminator [18], [23], [24]. The tunable laser is an SGDBR laser which consists of a DBR laser modified by periodic blanking of the front and back grating mirrors at different sampling periods. This produces a Vernier-like reflection spectra allowing for wide tunability [25]. The SGDBR laser was designed for tuning over the wavelength range of 1530 nm to 1570 nm. Coarse tuning of the wavelength is achieved by differential injection of current into the front and back mirrors of the laser. Fine tuning is achieved by equal current injection into the mirrors, or by current injection in a phase shifter inside the SGDBR cavity which controls the cavity mode locations. The grating design of the SGDBR also considers the front-to-back splitting to obtain the desired LiDAR output power and the sensitivity of the frequency discriminator. For this purpose, the mirror reflections were designed to give a front-to-back power splitting ratio of 7:1 by optimizing the number of sampled grating bursts. Power from the front mirror is guided to two semiconductor optical amplifiers (SOA), and 1×2 and 2×2 splitters for the OPA and receiver. The two SOAs use the same gain material as the SGDBR laser but are tapered to increase the mode size to prevent gain saturation. The 1×2 splitter is utilized to tap power for use in the receiver as a reference to the echo signal. A second, 2×2 , splitter is utilized for two purposes: first, to couple the reflected signal to the receiver, and second to measure chip

temperature through an on-chip PD. The laser, SOAs, couplers, and PDs were all implemented in surface ridge waveguides to minimize passive waveguide loss.

Frequency stabilization is achieved using a tunable a-MZI filter using deep ridge waveguides. The a-MZI converts frequency fluctuations of the laser to amplitude fluctuations of the PD currents. Power from the back mirror of the SGDBR laser is split by a 1×2 multimode interference coupler (MMI) between the two different paths of the a-MZI. The longer path also contains a phase shifter for tuning the filter quadrature frequency. A 2×2 MMI mixes the output from the two paths to allow balanced photodetection, eliminating common mode noise from the SGDBR laser. The transfer matrix relating the input electric field amplitude to the photocurrents in each PD is shown below:

$$\begin{pmatrix} I_1 \\ I_2 \end{pmatrix} \propto \begin{vmatrix} \begin{pmatrix} 1 & j \\ j & 1 \end{pmatrix} \begin{pmatrix} e^{(j\beta-\alpha)L_1} & 0 \\ 0 & e^{\phi} e^{(j\beta-\alpha)(L_1+\delta L)} \end{pmatrix} \\ \times \begin{pmatrix} 1 & j \\ j & 1 \end{pmatrix} \begin{pmatrix} E_0 \\ 0 \end{pmatrix} \end{vmatrix}^2 \quad (1)$$

Here, E_0 is the square root of the laser output power, β is the propagation constant of the waveguide mode, α is the waveguide loss, L_1 is the length of the shorter path in the a-MZI, δL is the additional path length of the second path, ϕ is the tunable phase shift in the second path, and $I_{1,2}$ is photocurrent in each PD. The transfer function using balanced photodetection is shown in Fig. 2a. Equation 1 can be used to determine the sensitivity to frequency fluctuations by calculating $dI/d\lambda$ and taking the maximum value. The sensitivity of the discriminator is determined by the input optical power, waveguide loss, and the free spectral range (FSR) of the a-MZI which is given by $c \cdot (n_{eff} \Delta L)^{-1}$. The sensitivity is quantified in terms of the discriminator slope as shown in Fig. 2b. The sensitivity, or slope, increases as the FSR decreases; however, the additional path length required to reduce the FSR increases the total loss. This reduces the sensitivity, as the photocurrent amplitude is proportional to the square of the electric field amplitude at the input. To address this trade-off, an FSR of 60 GHz was

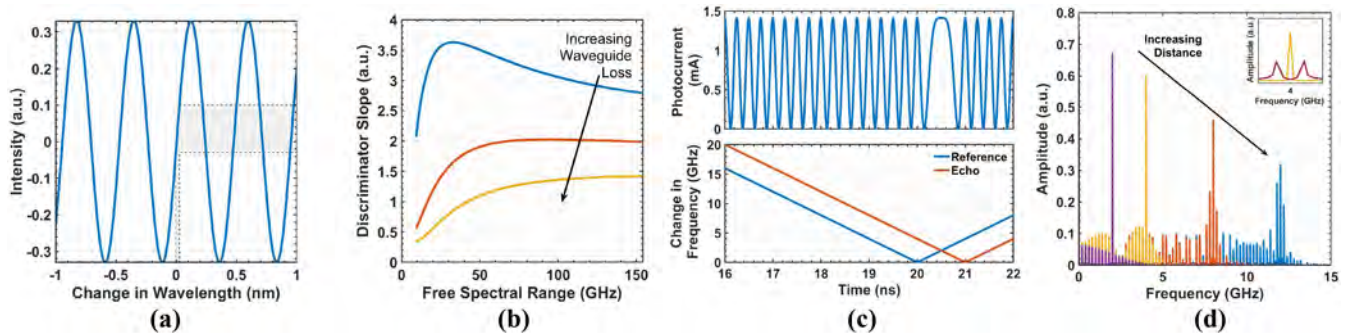


Fig. 2. (a) Output of a-MZI under balanced detection calculated from Eq. 1. The shaded region illustrates the amplitude change due to frequency changes of the laser output. (b) a-MZI based frequency discriminator sensitivity as the FSR varies for different passive waveguide losses. The orange curve uses a loss of 4 cm^{-1} typical for deep ridge waveguides in InP [23], [24], [26]. (c) Receiver operation principle. Bottom graph shows the instantaneous frequency of the reference and echo signal as a function of time. The top graph shows the measured photocurrent as the reference and echo signals beat together on the receiver PDs. (d) Frequency spectrum of the receiver photocurrent for reflections at different distances. The inset shows peak splitting due to the doppler effect for moving objects.

selected based on previous loss values of 4 cm^{-1} reported for deep ridge waveguides in InP [23], [24], [26]. The photocurrents generated in each PD are input to an off-chip circuit containing a two-stage differential amplifier with an inverting input to create the balanced detection, and a two-stage op-amp filter to drive the difference in PD photocurrents to zero. The amplifiers and filter act to convert the error to a current and inject it into the phase section of the laser cavity. This tunes the frequency of the laser to the quadrature point of the a-MZI where the power is equally split between the two photodiodes and the error is zero.

The a-MZI also contains a phase shifter in one path to shift the output interference independent of the frequency of the laser. This control is referred to as the “chirp” to reduce confusion with phase shifter in the SGDBR cavity. Injecting current into the chirp section tunes the quadrature frequency where the a-MZI equally splits the power between the two PDs. When the laser is frequency locked by the external circuit, tuning the quadrature frequency allows control over the laser frequency. By applying a modulated current to the chirp, the PIC can be used to realize FMCW LiDAR.

B. Receiver

The receiver consists of a 2×2 splitter and two PDs, which act to self-heterodyne the laser output with the received echo. Utilizing a 2×2 splitter allows for balanced photodetection in the receiver circuit to reject common mode noise and signal. The echo signal is coupled back into the transceiver PIC through the same port that coupled the output into the OPA. As shown in Fig. 2c, the reference and echo signal differ in frequency due to the additional travel time of the echo signal. The bottom graph shows the instantaneous frequency of the reference and echo signal at the receiver. The top graph shows the current measured by the receiver PDs that contains the beat frequency of the two signals. Fig. 2d shows the calculated frequency spectrum of the PD current for measurements on objects at different distances to illustrate the change in the peak frequency of the photocurrent. The inset shows the peak splitting imparted by a moving object due to doppler frequency shifts as discussed

previously. Also visible in the spectrums of Fig. 2d are satellite peaks arising from the beat frequency transient as the modulation changes direction (seen around 20 ns in Fig. 2c). This transient region sets the maximum range of the FMCW LiDAR system barring laser coherence length considerations. As the objects distance approaches one-half of the chirp period, the receiver photocurrent undergoes a constant frequency modulation and the spectrum is not peaked around a single value. Additionally, due to finite laser linewidth, there is a minimum detectable frequency shift, which affects the distance resolution as there will be some broadening in the frequency spectrum. The modulation period and rate must be selected to address desired range which is ultimately limited by the laser linewidth and frequency modulation bandwidth. The frequency locking technique described previously has demonstrated a linewidth of 570 kHz, which gives a maximum range of 160 m [24].

An important note on integration of the transmit and receive circuits for FMCW LiDAR, is the impact of the echo signal on the stability of the tunable laser. This can be broken down into three regimes: short-range (on-chip), medium-range, and long-range reflections. For the first case, all on-chip optical interfaces are angled to minimize reflections. Furthermore, it is well established that laser stability is not strongly influenced for very short external cavities [30], [31]. In the case of medium-range reflections, where the reflected power may be significant, the frequency modulation detunes the instantaneous emitting frequency from the reflection such that the influence of the reflections is strongly reduced [32]. For long range reflections, in addition to frequency detuning, the power will be below the limit to influence stability.

III. FABRICATION AND COMPONENT CHARACTERIZATION

A. PIC Fabrication

An overview of the fabrication process is shown in Fig. 3a. The starting material for the transceiver PIC is grown by metal organic chemical vapor deposition (MOCVD) up to an InP cap above the quantum well (QW) “active” layers. The QWs are selectively removed from the “passive” regions outside of the SGDBR gain section, the SOA and the PDs using a wet

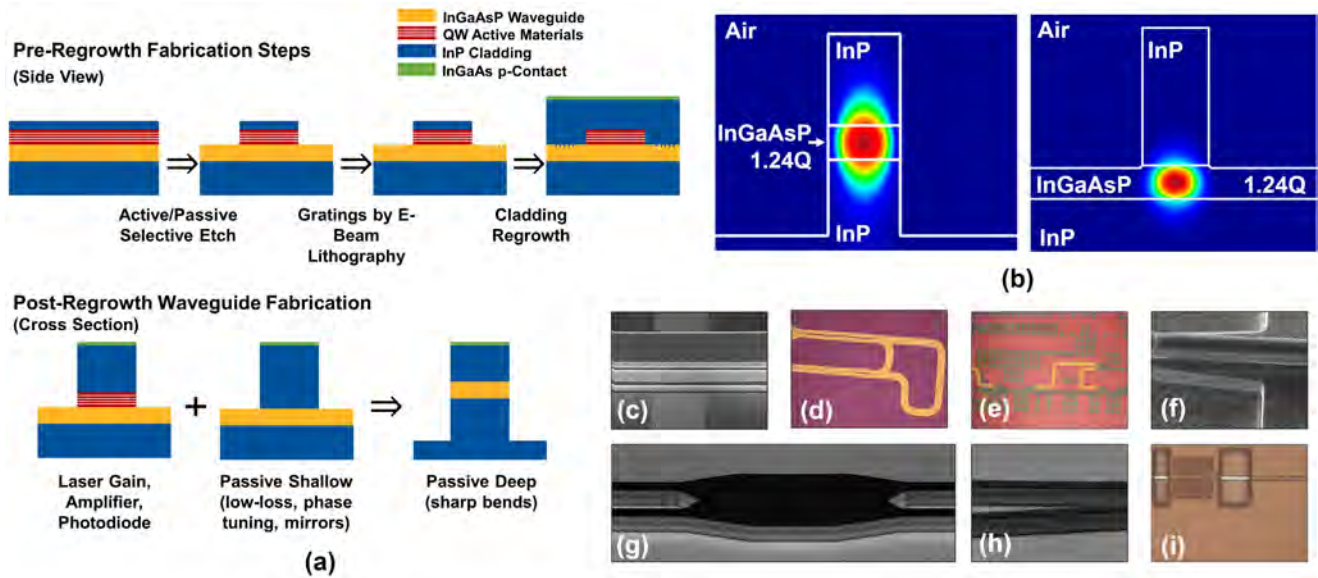


Fig. 3. (a) Overview of fabrication process for InP transceiver. The initial epitaxy structure is patterned to define the active regions with offset quantum wells. The gratings for the SGDBR laser are patterned and p-type InP and InGaAs are regrown by MOCVD for the cladding layer and p-contact. The waveguides are defined by wet and dry chemical etches to form the surface ridge waveguides for the laser, amplifiers, and photodiodes, and deep ridge waveguides for the sharp waveguide bends. (b) Optical mode simulations of the surface ridge and deep ridge waveguide structures used. (c–i) Images from fabrication showing various PIC components and processing steps. In order, these are the sampled gratings, a-MZI, waveguide definition, deep-to-shallow waveguide transition, 2×2 MMI, directional coupler and device isolation.

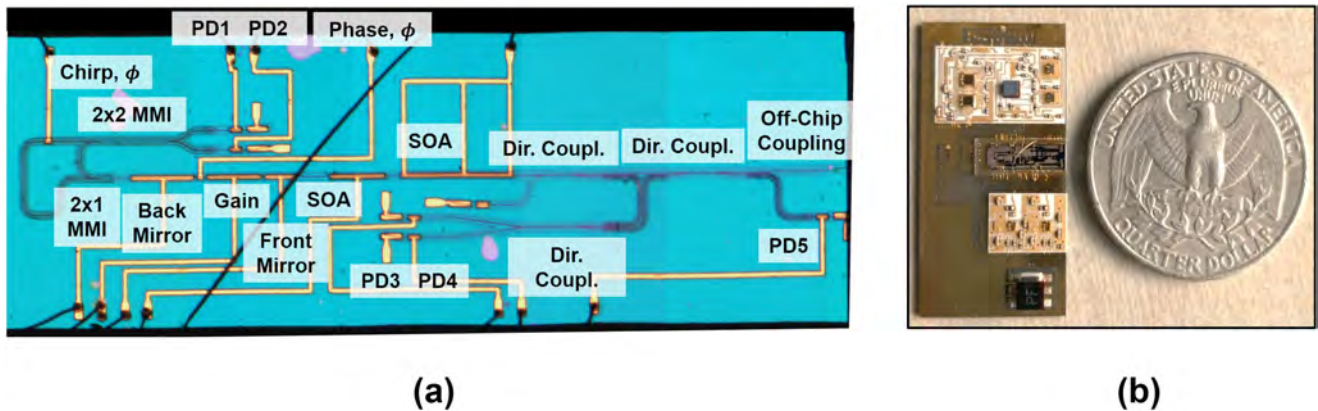


Fig. 4. (a) Image of fabricated PIC with components labeled. The dimensions are $8 \text{ mm} \times 2 \text{ mm}$. (b) Module for characterization of the PIC transceiver. The PIC is mounted on a carrier and sub-carrier which contains the electronics for the feedback circuit and receiver signal processing. The quarter is shown for scale.

chemical etch. The SGDBR sampled gratings are patterned using electron beam lithography and formed with a reactive-ion-etch (RIE). Next, the InP waveguide cladding and InGaAs p-contact are regrown using MOCVD. The waveguides are then defined using a combination of wet and dry chemical etches to form both surface ridge and deep ridge waveguides [27]–[29]. Fig. 3b shows the simulation of optical modes for the two different types of waveguides. The deep ridge waveguide provides higher optical confinement, allowing for sharper bend radii to keep the PIC footprint relatively small, however, this adds additional passive loss due to mode overlap with the etched side wall which contain some roughness from the etch. The surface ridge waveguide uses a selective wet etch which stops on the waveguide

layer and eliminates the loss due to sidewall roughness. Isolation between contacts of the electrodes is formed by removing the low resistance p-InGaAs layer on the top of the ridge waveguides, and a Ti/Pt/Au metal stack is deposited for the p-type contacts and probe pads. Fig. 3c–i shows images of taken during fabrication showing the various components. The wafer is thinned, and backside metal is deposited for a common N-contact. Lastly, the wafer is cleaved to separate the individual PICs. Fig. 4a shows the final fabricated PIC. The PICs were mounted on carriers for integration with electronic lockers and receiver circuits as shown in Fig. 4b. Testing of the PICs consisted of the following: Current-Voltage measurements on the all diodes, Light-Current-Voltage (LIV) measurements of gain section

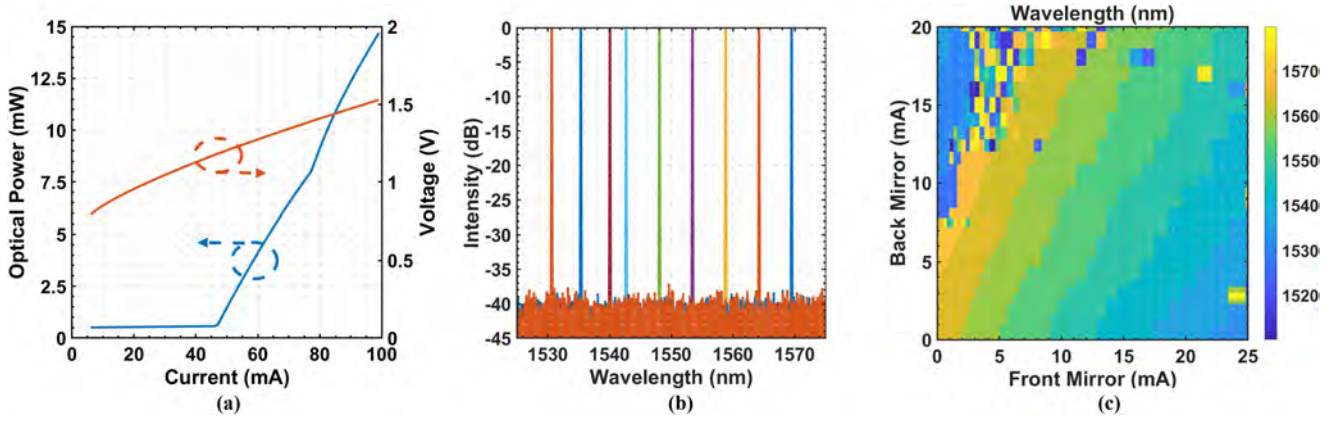


Fig. 5. (a) Light-current-voltage (LIV) measurement of the SGDBR laser. The laser threshold current is around 45 mA and an output power of 15 mW is achieved around 100 mA. The power is measured by reverse biasing the on-chip SOA. (b) Lasing spectrum over the tuning range of 1530 nm to 1570 nm. The side mode suppression ratio is greater than 37 dB for this range. (c) Wavelength tuning map as a function of current injection into the front and back mirror.

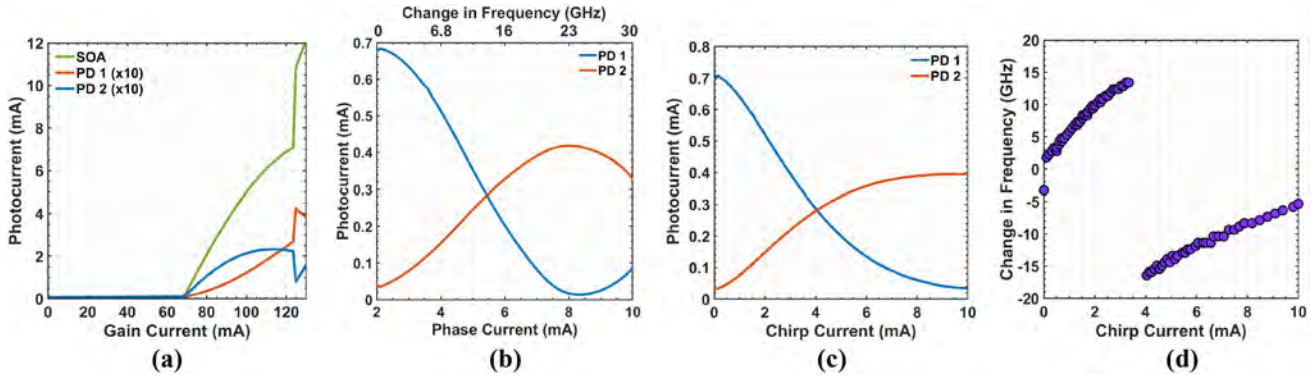


Fig. 6. (a) Photocurrent measured by the SOA and two PDs of the frequency discriminator. The discontinuity around 120 mA is a result of a mode hop. (b) Photocurrent in each PD of the frequency discriminator as a function of the current injected into the phase section of the SGDBR cavity. The top axis shows the corresponding frequency change of the laser output measured using an optical spectrum analyzer. (c) Photocurrent in each PD of the frequency discriminator as a function of the current injected into the chirp section of the a-MZI. (d) The locking frequency offset as a function chirp current. This is obtained by taking multiple measurements at various a-MZI chirp and SGDBR phase currents and measuring the frequency of photocurrent crossing point.

using reverse biased SOA and PDs to measure optical power, SGDBR spectrum mapping using the front and back mirrors, LI measurements of the discriminator PDs as the phase and chirp sections are tuned, and frequency chirp control.

B. SGDBR Laser Performance

The measured LIV of the SGDBR laser is shown in Fig. 5a. The threshold current is around 45 mA with the laser output achieving 15 mW at 100 mA. Fig. 5b shows wavelength tuning from 1530 nm to 1570 nm with side mode suppression ratio greater than 37 dB over the entire tuning range. Fig. 5c shows a full tuning map as the current is varied in the front and back mirrors. In practice, this provides a look-up table to tune the laser frequency and sample a discrete set of angular point using an OPA. The output during the transient stabilization can be suppressed by reducing the gain of the on-chip SOAs. Additionally, identical SGDBR lasers have been characterized by our group showing free-running linewidths of 6 MHz [22].

C. Frequency Discriminator Response

Characterization of the frequency discriminator consists of first determining the power reaching the PDs, then tuning the lasing wavelength by using the phase shifter in the SGDBR cavity, followed by tuning of the filter spectral location using the chirp section in the a-MZI. The photocurrent detected by the discriminator PDs was measured alongside the SOA photocurrent as shown in Fig. 6a. The SOA measures the power from the front mirror, while the two discriminator PDs measure the power from the back mirror. As mentioned above, a front to back splitting ratio of 7:1 was expected from the front and back mirror designs. However, lower power was detected at the discriminator PDs, which we attribute to passive optical loss in the deep ridge waveguide of the a-MZI. The photocurrent in each detector as a function of phase current is shown in Fig. 6b. Current injection into the phase section of the SGDBR provides fine tuning of the laser frequency, which is measured on an Optical Spectrum Analyzer and shown on the top x-axis of Fig. 6b. As discussed in Section II, the a-MZI was designed to have an FSR

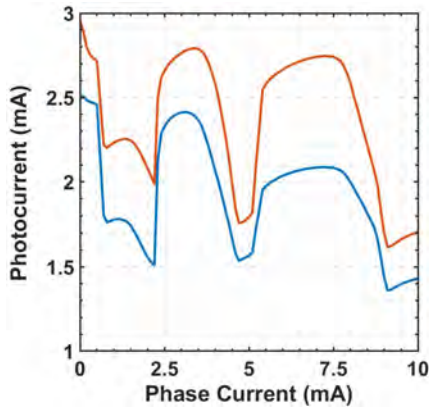


Fig. 7. Receiver photocurrent as a function of the SGDBR phase current. The large variations in the photocurrent are due to mode hops of the laser.

of 60 GHz. Fig. 6b shows that the filter passes through half of a cycle in 30 GHz of frequency tuning. Lastly, the filter quadrature location is tuned using the chirp section in the a-MZI as shown in Fig. 6c.

The external locking circuit operates by injecting current into the phase section of the SGDBR such that the lasing frequency is located at the quadrature point of the a-MZI and equal power is distributed to the two PDs. By tuning the current injected into the chirp section, the quadrature frequency is changed, and the output of the feedback circuit changes to maintain the locking condition. Fig. 6d shows the offset lasing frequency tuning over 30 GHz as the chirp phase shifter current is tuned between 0 mA to 10 mA. By imparting a triangular waveform with a current modulation range of 10 mA, the frequency of the laser can be modulated continuously over 30 GHz with a tuning efficiency of 3 GHz/mA.

D. Receiver

The receiver consists of two PDs and a 2×2 MMI. One input consists of the reference signal from the SGDBR laser and the second is the echo signal. Fig. 7 shows the measured photocurrent in each PD as the phase section of the SGDBR laser is tuned with no intentional reflection. With an intentional reflection present, this would undergo a similar beating response as seen in Fig 6b. As shown in Fig. 7, the reference signal provides greater than 1 mW of input power into the receiver. This falls into the regime of shot noise limited operation making the minimum detectable echo signal power around 1 nW [33].

IV. CONCLUSION

We presented a PIC transceiver consisting of an SGDBR laser with an on-chip frequency discriminator for frequency locking and modulation for LiDAR applications. The components of the PIC were characterized to demonstrate functionality and the operating principles of the transceiver. Future experiments will implement one-dimensional ranging measurements. This can be achieved by imparting frequency modulation in the a-MZI and coupling to fiber with delay lines and 2×2 couplers to act as near perfect reflectors to extract the beat frequency at various delay

lengths. In addition, the PIC transceiver can be butt-coupled to an OPA for full 2D beam-steering experiments and free space ranging measurements.

ACKNOWLEDGMENT

The authors acknowledge Paul Suni, James Colosimo, and S. J. Ben Yoo for technical discussions.

REFERENCES

- [1] L. A. Coldren, "Monolithic tunable diode lasers," *IEEE J. Sel. Topics Quantum Electron.*, vol. 6, no. 6, pp. 988–999, Nov./Dec. 2000.
- [2] S. Arafin and L. A. Coldren, "Advanced InP photonic integrated circuit for communication and sensing," *IEEE J. Sel. Topics Quantum Electron.*, vol. 24, no. 1, Jan./Feb. 2018, Art. no. 6100612.
- [3] D. F. Welch *et al.*, "The realization of large-scale photonic integrated circuits and the associated impact on fiber-optic communication systems," *J. Lightw. Technol.*, vol. 24, no. 12, pp. 4674–4683, Dec. 2006.
- [4] R. Soref, "The past, present, and future of silicon photonics," *IEEE J. Sel. Topics Quantum Electron.*, vol. 12, no. 6, pp. 1678–1687, Nov./Dec. 2006.
- [5] J. Klamkin *et al.*, "Indium Phosphide Photonic Integrated Circuits: Technology and Applications," presented at the IEEE BiCMOS Compound Semicond. Integr. Circuits Technol. Symp., San Diego, CA, USA, 2018.
- [6] R. Nagarajan, M. Filer, Y. Fu, M. Kato, T. Rope, and J. Stewart, "Silicon photonics-based 100 Gbit/s," *J. Opt. Commun. Netw.*, vol. 10, no. 7, pp. 25–36, Jul. 2018.
- [7] T. Pinguet *et al.*, "High-volume manufacturing platform for silicon photonics," *Proc. IEEE*, vol. 106, no. 12, pp. 2281–2290, Dec. 2018.
- [8] M.-C. Amann, T. M. Bosch, M. Lescure, R. Myllyla, and M. Rioux, "Laser ranging: A critical review of usual techniques for distance measurement," *Opt. Eng.*, vol. 40, no. 1, Jan. 2001.
- [9] M. Flood, "Laser altimetry: From science to commercial LiDAR Mapping," *Proc. Photogrammetric Eng. Remote Sens.*, Nov. 2001.
- [10] B. Schwarz, "Mapping the World in 3D," *Nature Photon.*, vol. 4, pp. 429–430, 2010.
- [11] H. K. Tsang *et al.*, "Two-photon absorption and self-phase modulation in InGaAsP/InP multi-quantum-well waveguides," *J. Appl. Phys.*, vol. 70, no. 7, pp. 3992–3994, 1991.
- [12] H. K. Tsang *et al.*, "Optical dispersion, two-photon absorption and self-phase modulation in silicon waveguides at 1.5 μm wavelength," *Appl. Phys. Lett.*, vol. 80, no. 3, 2002, Art. no. 416.
- [13] L. Yin and G. P. Agrawal, "Impact of two-photon absorption on self-phase modulation in silicon waveguides," *Opt. Lett.*, vol. 32, no. 14, pp. 2031–2033, 2007.
- [14] C. C. Lee and H. Y. Fan, "Two-photon absorption and photoconductivity in GaAs and InP," *Appl. Phys. Lett.*, vol. 20, no. 1, pp. 18–20, 1972.
- [15] S. Pinna, B. Song, L. A. Coldren, and J. Klamkin, "Vernier transceiver architecture for side-lobe-free and high-entendue LiDAR," presented at the Conf. Lasers Electro-opt., OSA Tech. Dig. (online), San Jose, CA, USA, 2018.
- [16] J. K. Doyle *et al.*, "Fully integrated hybrid silicon two-dimensional beam scanner," *Opt. Express*, vol. 23, no. 5, pp. 5861–5874, 2015.
- [17] J. K. Doyle, M. J. Heck, J. T. Bovington, J. D. Peters, L. A. Coldren, and J. E. Bowers, "Two-dimensional free-space beam steering with an optical phased array on silicon-on-insulator," *Opt. Express*, vol. 19, no. 22, pp. 21595–21604, 2011.
- [18] B. Isaac *et al.*, "Indium phosphide photonic integrated circuit transmitter with integrated linewidth narrowing for laser communications and sensing," presented at the IEEE Int. Semicond. Laser Conf. (ISLC), Santa Fe, NM, USA, 2018.
- [19] P. R. A. Binetti *et al.*, "Indium phosphide photonic integrated circuits for coherent optical links," *IEEE J. Quantum Electron.*, vol. 48, no. 2, pp. 279–291, Feb. 2012.
- [20] Y. A. Akulova *et al.*, "Widely tunable electroabsorption-modulated sampled-grating DBR laser transmitter," *IEEE J. Sel. Topics Quantum Electron.*, vol. 8, no. 6, pp. 1349–1357, Nov./Dec. 2002.
- [21] J. Raring *et al.*, "Single-Chip 40Gb/s widely-tunable transceivers with integrated SG-DBR laser, QW EAM, UTC photodiode, and low confinement SOA," presented at the IEEE 20th Int. Semicond. Laser Conf., Kohala Coast, Hawaii, 2006.
- [22] H. Zhao *et al.*, "Indium phosphide photonic integrated circuits for free space optical links," *IEEE J. Sel. Topics Quantum Electron.*, vol. 24, no. 6, Nov./Dec. 2018, Art. no. 6101806.

- [23] A. Sivanathan *et al.*, "Monolithic linewidth narrowing of a tunable SG-DBR Laser," presented at the OFC (OSA), Paper OTh31.3, Anaheim, CA, USA, 2013.
- [24] A. Sivanathan *et al.*, "Integrated linewidth reduction of a tunable SG-DBR laser," presented at the CLEO (OSA), CTu1L, San Jose, CA, USA, 2013.
- [25] V. Jayaraman, Z.-M. Chuang, and L. A. Coldren, "Theory, design, and performance of extended tuning range semiconductor lasers with sampled gratings," *IEEE J. Quantum Electron.*, vol. 29, no. 6, pp. 1824–1834, Jun. 1993.
- [26] J. S. Parker, E. J. Norberg, R. S. Guzzon, S. C. Nicholes, and L. A. Coldren, "High verticality InP/InGaAsP etching in inductively coupled plasma for photonic integrated circuits," *J. Vacuum Sci. Technol. B*, vol. 29, no. 1, 2011, Art. no. 011016.
- [27] L. Coldren, K. Furuya, B. Miller, and J. Rentschler, "Combined dry and wet etching techniques to form planar (011) facets in GaInAsP/InP double heterostructures," *Electron. Lett.*, vol. 18, no. 5, pp. 235–237, Mar. 1982.
- [28] S. Uekusa, K. Oigawa, and M. Tacano, "Preferential etching of InP for submicron fabrication with HCl/H₃PO₄ solution," *J. Electrochem. Soc.*, vol. 132, no. 3, pp. 671–673, 1985.
- [29] F. Karouta *et al.*, "High aspect ratio etching and application in InP-based photonic integrated circuits," presented at the Electrochemical Soc. Meeting, Honolulu, Hawaii, 2008.
- [30] K. Petermann, *Laser Diode Modulation and Noise*. Dordrecht, The Netherlands: Kluwer Academic Publishers, 1988.
- [31] L. A. Coldren, S. W. Corzine, and M. L. Masanovic, *Diode Lasers and Photonic Integrated Circuits*. Hoboken, NJ, USA: Wiley, 2012.
- [32] L. A. Johansson and L. A. Coldren, "Wavelength-tunable receiver channel selection and filtering using SG-DBR laser injection-locking," presented at the OFC/NFOEC Tech. Dig., Anaheim, CA, USA, 2005.
- [33] K. Kikuchi and S. Tsukamoto, "Evaluation of the sensitivity of the digital coherent receiver," *J. Lightw. Technol.*, vol. 26, no. 13, pp. 1817–1822, Jul. 2008.



Brandon J. Isaac received the B.S. degree in chemical engineering and physics from the University of Kentucky, Lexington, KY, USA, in 2013. He is working toward the Ph.D. degree in materials with the University of California Santa Barbara with a focus on opto-electronic devices and photonic integrated circuits. Prior to joining the Integrated Photonics Lab at UCSB, he worked on oxide heterostructure growth in the UCSB Molecular Beam Epitaxy Lab. He is a Student Member of OSA and recipient of NSF GRFP.



Bowen Song is from Shanxi, China. He received the B.E. degree from the School of Electronic Engineering and Optoelectronic Technology, Nanjing University of Science and Technology, Nanjing, China, in 2012, and the M.Sc. degree from Boston University, Boston, MA, USA, in September 2014. He is currently working toward the Ph.D. degree with the Department of Electrical and Computer Engineering, UCSB, Santa Barbara, CA, USA. In early 2013, he joined the Wide Bandgap Semiconductor Laboratory, Boston University, worked on developing

nano-patterned sapphire substrate for AlGaN-based deep UV LEDs. His current research interests include electronic-photonic integration, integrated photonics, and integrated Lidar.



Sergio Pinna received the B.Sc. and M.Sc. degrees in telecommunications engineering from the University of Pisa, Pisa, in 2008 and 2010, respectively, and the Ph.D. degree in innovative technologies from the Scuola Superiore Sant'Anna, Pisa, Italy, in 2014. From November 2010 to December 2015, he was a Fellow with CNIT, National Photonic Networks Laboratory, Pisa. In 2014, he was a Visiting Researcher at the Integrated Photonics Laboratory, Boston University, Boston, USA. From January 2016, he was a Research Fellow with TeCIP Institute, Scuola Superiore Sant'Anna, Pisa, within the Digital and Microwave photonics group.

In 2017, he joined the Integrated Photonics Laboratory, University of California Santa Barbara, as a Postdoctoral Research Associate. His research activity focuses on photonics for microwave applications and LiDAR sensors.



Larry A. Coldren received the Ph.D. degree in electrical engineering from Stanford University, Stanford, California, and spent 13 years in research at Bell Labs before joining UCSB in 1984. He is a Distinguished Professor Emeritus and Research Professor with the University of California, Santa Barbara, CA, USA. He has served as Director of several multi-university optoelectronics research centers, including one of the DARPA/Industry sponsored Optoelectronics Technology Centers throughout the 1990s. He also acted as Dean of Engineering at UCSB from 2009–

2011. In 1991 he Co-Founded Optical Concepts, acquired as Gore Photonics, to develop novel Vertical-Cavity Surface-Emitting Laser (VCSEL) technology; and later in 1998, Agility Communications, acquired by JDS-Uniphase (now Lumentum), to develop widely-tunable integrated optical transmitters. At Bell Labs, he worked on Surface-Acoustic-Wave (SAW) filters and tunable coupled-cavity lasers using novel RIE technology that he was first to develop for the then new InP-based materials. At UCSB he continued work on multiple-section lasers, in 1988 inventing the widely-tunable multielement mirror concept, now used in numerous commercial products. He has also made seminal contributions to efficient VCSEL designs, now used in high-speed data links. His group was first to suggest and demonstrate that gain elements should be placed only at E-field standing-wave maxima, which is key to all commercial VCSELs today. He continues efforts on high-performance InP-based photonic integrated circuits (PICs) and high-speed VCSELs. He has authored or coauthored more than a thousand journal and conference papers, including numerous plenary, tutorial and invited presentations. He has also coauthored eight book chapters and two textbooks, including the most used text on Diode Lasers and Photonic ICs in circulation today. He has been issued 61 patents and is a recipient of several awards, including the John Tyndall, Aron Kressel, David Sarnoff, IPRM, and Nick Holonyak Jr. Awards. He is a Life Fellow of the IEEE, and a Fellow of the OSA, the National Academy of Inventors, and IEE as well as a member of the National Academy of Engineering.



Jonathan Klamkin received the B.S. degree from Cornell University, Ithaca, NY, USA and the M.S. and Ph.D. degrees from the University of California Santa Barbara, Santa Barbara, CA, USA. From 2008 to 2011, he was a member of the Technical Staff in the Electro-Optical Materials and Devices Group, MIT Lincoln Laboratory, Lexington, MA, USA. From 2011 to 2013, he was an Assistant Professor with the Institute of Communication, Information and Perception Technologies at the Scuola Superiore Sant'Anna, Pisa, Italy. From 2013 to 2015, he was

an Assistant Professor of Electrical and Computer Engineering (ECE) and materials at Boston University, Boston, MA, USA. In 2015, he joined the ECE Department at the University of California Santa Barbara, where he is currently an Associate Professor and Director of the UCSB Nanotech. He is an Associate Editor for Photonics Technology Letters, Vice Chair for the Microwave Theory and Techniques Society Subcommittee on Microwave Photonics, and Steering Committee Member for the Journal of Lightwave Technology. He was Program Chair for the Integrated Photonics Research, Silicon and Nanophotonics Conference, in 2017, and General Chair for the same conference, in 2018. He or his group members received best paper awards at the 2006 Conference on Optoelectronic and Microelectronic Materials and Devices, the 2007 Microwave Photonics Conference, and the 2017 Asia Communications and Photonics Conference. He has published more than 180 journal and conference papers and holds three patents. He received the NASA Early Career Faculty Award and the DARPA Young Faculty Award. He is a Senior Member of the IEEE and OSA.

High-Power Indium Phosphide Photonic Integrated Circuits

Hongwei Zhao , Sergio Pinna, Fengqiao Sang, Bowen Song, Simone Tommaso Šuran Brunelli, Larry A. Coldren , *Life Fellow, IEEE*, and Jonathan Klamkin, *Senior Member, IEEE*

(Invited Paper)

Abstract—Indium phosphide (InP) is the most developed platform for photonic integrated circuits (PICs). Of interest is the advancement of this platform for applications that demand high performance, especially high output power, including free space communications and microwave photonics. In this paper, we summarize development of InP-based PIC transmitters. Two transmitter types were fabricated: one based on an offset quantum wells (OQW) platform and the other on a quantum well intermixing (QWI) platform. The OQW-based transmitter consists of a widely tunable laser, a high-speed semiconductor optical amplifier (SOA), a Mach–Zehnder modulator, and an output SOA. This transmitter demonstrates a 44-nm tuning range, >45 dB side mode suppression ratio, 14.5 dBm OFF-chip power, and a data rate of 7 Gbps. The second transmitter, based on QWI, utilizes an alternate epitaxial structure to achieve a lower confinement factor for higher SOA output saturation power. This QWI transmitter consists of a distributed Bragg reflector laser, a high-speed SOA, an electroabsorption modulator, and an output SOA. The measured OFF-chip power is 19.5 dBm, and a data rate of 20 Gbps is demonstrated. Based on the improved performance with the new epitaxial structure, a novel platform for high-power PIC transmitters integrated with low confinement and high-power SOAs is described.

Index Terms—Photonic integrated circuits, DBR laser, optical transmitter, sampled grating DBR laser, semiconductor optical amplifier, offset quantum wells, quantum well intermixing, free space optics.

I. INTRODUCTION

INDIUM phosphide (InP) is the most advanced platform for high-performance large-scale photonic integrated circuits (PICs). This platform allows for the monolithic integration of all the required active elements (e.g., lasers, semiconductor optical amplifiers (SOAs), modulators, photodetectors), and passive components (e.g., waveguide interconnects, filters, couplers), thus enabling complex single-chip implementations

Manuscript received February 1, 2019; revised March 22, 2019; accepted March 26, 2019. Date of publication April 2, 2019; date of current version May 14, 2019. This work was supported by a NASA Early Stage Innovations Award. (Corresponding author: Hongwei Zhao.)

The authors are with the Department of Electrical and Computer Engineering, University of California Santa Barbara, Santa Barbara, CA 93106 USA (e-mail: hwzhao@ece.ucsb.edu; pinna@ece.ucsb.edu; fsang@ece.ucsb.edu; bowen@ece.ucsb.edu; ssuranbrunelli@umail.ucsb.edu; coldren@ece.ucsb.edu; klamkin@ece.ucsb.edu).

Color versions of one or more of the figures in this paper are available online at <http://ieeexplore.ieee.org>.

Digital Object Identifier 10.1109/JSTQE.2019.2908788

of advanced transmitters and receivers. Compared to optical systems with discrete components, monolithic integration improves the system reliability and provides significant reduction in packaging cost, system footprint, fiber coupling loss and power consumption [1]–[3].

High-performance InP-based PICs have been widely used in coherent transmitter, receiver, wavelength-conversion and packet-switching applications [4]–[7]. The last several decades have witnessed the maturation of InP from discrete photonic devices to complex high-functionality PICs. The electroabsorption modulated laser (EML) was first introduced in mid-1980s [8]. This device integrated a three-section distributed Bragg reflector (DBR) laser with an electroabsorption modulator (EAM). Distributed feedback (DFB) lasers were also incorporated into EMLs and this two-component device has become a mainstay in telecommunications, providing benefits over the use of separate discrete components [9]. Widely tunable laser sources were developed for wavelength division multiplexing (WDM) systems, but have also found use in sensing applications. The sampled grating DBR (SGDBR) laser was first proposed in early 1990s. It provides wide optical tuning range without compromising mode suppression [10]–[12]. The first commercial large-scale multi-channel InP PIC transmitter/receiver for dense WDM was reported in 2004 [13]. Since then, advancements have been made in manufacturing capability so as to realize InP PICs with 14-channel coherent transmitter on a single chip for 4.7 Tbps aggregate capacity [14].

In addition to fiber optic communication systems, InP PICs can impact other applications where high performance is required in conjunction with low cost, size, weight and power (CSWaP). These include microwave photonics and free space communications [15]–[18]. For high linearity microwave photonics links, InP coherent receivers were developed demonstrating state-of-the-art spurious-free dynamic range [19]. Widely tunable InP PICs have also been used for optical frequency synthesis and coherent LiDAR [20], [21]. PICs are particularly attractive for free space optical communications where low CSWaP is critical [22]–[25]. The Lunar Laser Communications Demonstration (LLCD) was a highly successful demonstration of laser communications (lasercom) in space [26]. Since the success of this program, several lasercom efforts have been pursued by various space agencies and by industry [27]. Lasercom transmitters are desired to output high peak power levels

and to support power-efficient modulation formats [28], [29]. Although some work has been carried out to realize high-power InP lasers and SOAs [30]–[32], little to no work has been carried out to realize a full high-power InP PIC platform because of the challenges associated with integrating high-confinement waveguides (for seed lasers, modulators, photodetectors, and passives) with low-confinement waveguides (for high-power lasers and SOAs).

In conventional InP PICs, the active waveguide width is typically only 2–3 μm , resulting in mode dimensions on the order of 3 $\mu\text{m} \times 1 \mu\text{m}$. The small mode size and high confinement factor (>5%) is beneficial to achieve maximum modal gain for lasers and high efficiency for modulators. However, high confinement limits the saturation output power of SOAs. A number of approaches have been employed to improve the SOA saturation power. One is to increase the width of the active region with a flared waveguide [33], [34]. Waveguide SOAs with width of a few hundred microns were reported with output power up to 0.3 W [35]. Since the thickness of the active region is typically 1 μm , the large beam dimension in the horizontal direction imposes challenges on the coupling to single-mode fiber. A second approach is to decrease the confinement factor. The photon density within the active region is reduced with lower confinement, thus decreasing the stimulated emission rate, which slows down the carrier depletion and in turn increases the saturation power. Slab-coupled optical waveguides (SCOW) with small confinement factor ($\sim 0.25\%$ – 1%) have been investigated for high-power SOAs and lasers. Unlike conventional single-mode waveguide SOAs, the SCOW concept expands the mode in the vertical direction and is engineering for single-mode behavior. External-cavity SCOW lasers and SOAs with 29-dBm saturation power have been separately reported [36], [37]. However, it is very challenging to realize monolithic integration of the SCOW SOAs with other optical elements required for a PIC such as a seed laser and modulator.

In this work, we have investigated InP PIC transmitters for high optical power and proposed a novel platform enabling the monolithic integration of low-confinement SOAs with other high-confinement components including a seed laser and high-speed modulator. The first type of InP PIC transmitter presented is based on an offset quantum well (OQW) platform. Although the fabrication process is fairly simple, the performance of the integrated components is limited. It is also challenging to incorporate a dilute waveguide (i.e., an InGaAsP waveguide layer with lower refractive index) into this platform primarily because of the mode discontinuity in the active and passive regions. Nevertheless, OQW InP PICs with seed lasers, modulators, and booster SOAs demonstrated up to 14.5 dBm off-chip power and a 7 Gbps data rate. These PICs were also incorporated into a basic free space transmission experiment and were compared in performance to a transmitter based on high-performance commercial discrete components [15], [29]. A more advanced transmitter was developed based on a quantum well intermixing (QWI) platform. In addition to allowing for the integration of higher efficiency modulators, this platform was adapted to a dilute waveguide structure allowing for the integration of both high-confinement and low-confinement waveguide compo-

nents. The QWI PIC transmitters demonstrated up to 19.5 dBm off-chip output power and a 20 Gbps data rate. In addition to describing the design, fabrication, and characterization results of the OQW and QWI PIC transmitters, a discussion is provided on the implementation and integration of low-confinement, high-power integrated SOAs.

II. HIGH POWER AMPLIFIERS

The optical output power of PICs primarily depends on the performance of the output SOA. The main factors limiting the output power of an SOA are the gain (G) and saturation output power ($P_{o, sat}$). During the amplification process, the carriers in the active gain region become depleted as the optical power increases, resulting in a decrease of the gain and the power saturation. The saturation output power can be expressed as:

$$P_{o, sat} = \left(\frac{G_0 \ln 2}{G_0 - 2} \right) A \left(\frac{h\nu}{a\tau} \right) \quad (1)$$

where G_0 is the unsaturated gain, $h\nu$ is the photon energy, a is the differential gain, τ is the carrier lifetime, and A is the amplifier modal area [30]. In conventional SOAs, A can be estimated as:

$$A = \frac{wd}{\Gamma} \quad (2)$$

where w and d are the width and thickness of the active material, and Γ is the optical confinement factor. $P_{o, sat}$ is proportional to the modal area, which can be increased by proper design of the waveguide structure in the active layers.

In this work, two different InP-based epitaxial structures (denoted S1 and S2) were investigated for output power considerations, one based on the OQW platform, and the other on an advanced QWI platform that includes a lower dilute waveguide for transitioning a guided optical mode to lower optical confinement. The epitaxial structures were grown by metal organic chemical vapor deposition (MOCVD) on n-type (001) InP substrates. In both structures, the active layers consist of five pairs of indium gallium arsenide phosphide (InGaAsP) quantum wells that are situated above an InGaAsP waveguide (WG) core layer. The layer structures and corresponding fundamental TE modes in a ridge waveguide are shown in Fig. 1 and Fig. 2. Ordinarily a high index waveguide core layer is selected for low threshold high efficiency lasers. For S1, the composition of the InGaAsP WG core layer was selected to achieve a slightly lower index (bandgap wavelength of 1.24 μm), so that the confinement factor is made lower without significant change to the epitaxial layers. For S2, a 2.5- μm thick waveguide layer (WG2) was added below the primarily guiding structure. With the same ridge waveguide width, S2 yields a modal area of 3.37 μm^2 , 53% larger than that of S1. The modal area can be significantly increased from this by engineering the waveguide geometry so that the mode mostly couples to the lower waveguide layer WG2.

By tailoring the waveguide geometry, two advanced SOA designs with ultralow confinement (<1%) in the active gain region would enable higher saturation output power. Fig. 3 shows two SOA designs with epitaxial structure S2. As the waveguide width is reduced from 3 μm to 1.5 μm and the

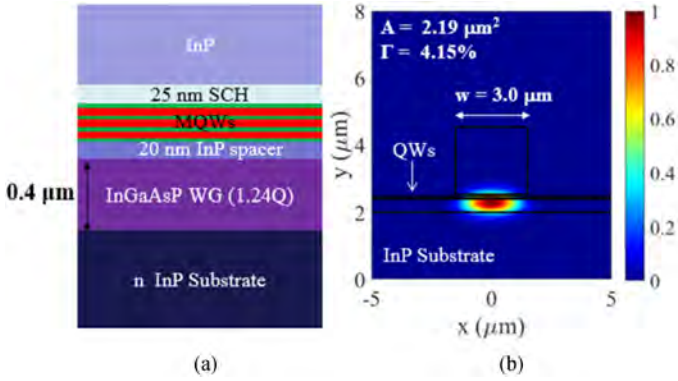


Fig. 1. (a) Epitaxial structure S1; (b) Fundamental TE mode in a ridge waveguide with S1.

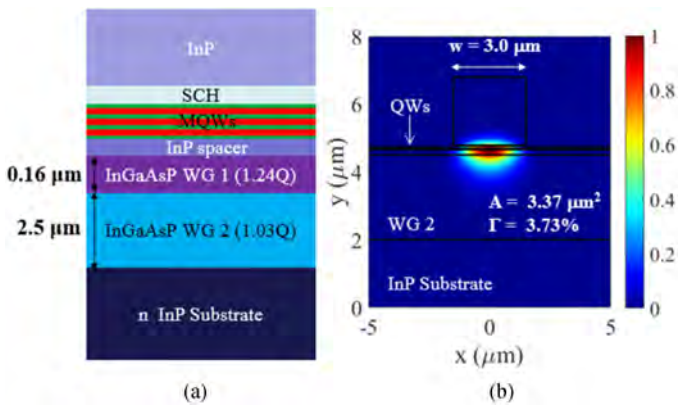


Fig. 2. (a) Epitaxial structure S2; (b) Fundamental TE mode in a ridge waveguide with S2.

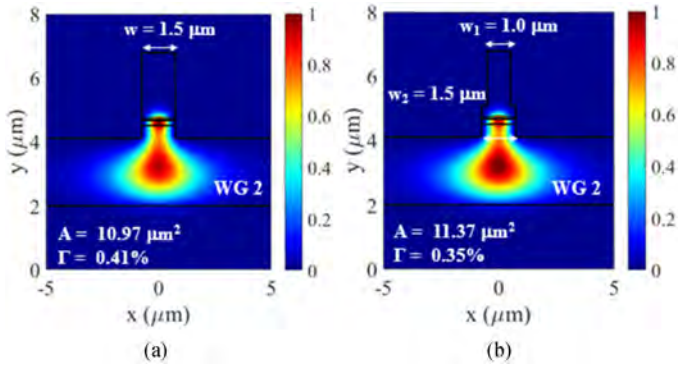


Fig. 3. Fundamental TE mode in advanced waveguide designs with epitaxial structure S2 for ultralow confinement and ultimately high SOA output saturation power. (a) Single-ridge waveguide; (b) Double-ridge waveguide.

ridge is etched into the lower waveguide layer, the confinement is dramatically decreased to 0.41% and the corresponding modal area is increased by a factor of 3.3. A double ridge design would further lower the confinement factor and increase the modal area. This latter structure facilitates the coupling of the optical mode from the high confined regime, where most of the mode is confined in the upper waveguide (WG1), to the

lower confined regime, where most of the mode is confined in the lower waveguide (WG2).

III. INTEGRATION PLATFORM AND FABRICATION

A high-functionality PIC platform must facilitate coupling between different integrated elements to optimize system performance and reliability. This can be challenging since the design of each element requires unique epitaxial structures and waveguide designs for optimum device performance. High efficiency lasers require a highly confined quantum well structure for large modal gain. Mach-Zehnder modulators (MZMs) based on the Franz-Keldysh effect utilize bulk material. For EAMs, the bandgap of the quantum wells should be blue shifted from that of the laser region to reduce insertion loss. For high saturation power SOAs, a weakly confined optical mode is preferred for lowering the local photon density. To enable complex functions on a single chip, efforts have been made to advance various integration technologies over the past three decades. Integration schemes include selective area regrowth (SAG), butt-joint growth (BJG), OQW, and QWI.

SAG utilizes a patterned dielectric mask to modify the thickness and composition of the epitaxial layers, allowing for varying bandgaps across a wafer [38], [39]. The growth conditions have to be precisely controlled to achieve desired bandgaps.

BJG involves selective removal of as-grown quantum wells, selective regrowth of alternative material structures with desired bandgaps, and then growth of a doped upper cladding [40], [41]. Some such processes include an additional regrowth step to incorporate an unintentionally doped cladding in the passive regions. BJG requires separate complex growth steps for each component thus increases the fabrication complexity and consequently yield problems in the past. Recent investigations on the epitaxial technology have resolved the yield issue with BJG [42], [43].

The OQW platform is simple and robust. It is based on the selective removal of quantum wells in regions where gain is not needed and a single, blanket (i.e., not selective) P-type cladding regrowth [44], [45]. Since this platform allows for only two unique bandgaps, the SOAs must share the same epitaxial layers as the lasers, generally resulting in higher confinement than is not desired for a high power SOA. The composition of the waveguide core also influences the tradeoffs between passive loss, modulator efficiency, and SOA saturation power.

QWI is a post growth technique that can modify the bandgap of quantum wells selectively. The QWI process utilized here is based on ion implantation and annealing to generate point defects in a sacrificial layer and subsequently diffuse these defects into the quantum well region [46], [47]. This process ultimately reshapes the quantum wells and effectively increases the quantum well bandgap. This platform is ideal because it allows for integration of multiple bandgaps while minimizing the index discontinuity at interfaces, the latter of which is important for integration with low confinement waveguides such as that utilized in structure S2.

With epitaxial structure S1, a PIC transmitter was realized by simple OQW platform. Fig. 4 illustrates the OQW-based

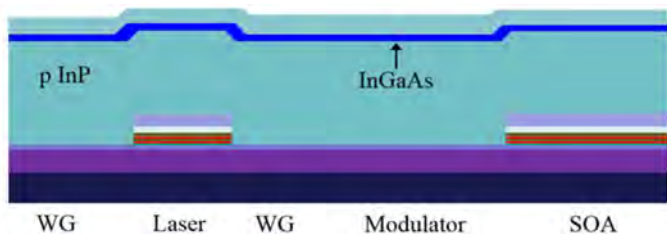


Fig. 4. Schematic of the OQW-based PIC transmitter.

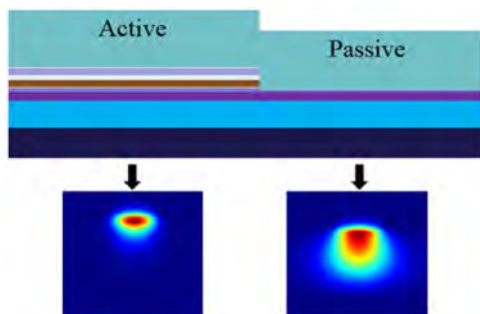


Fig. 5. Active/passive interface of S2 with OQW platform.

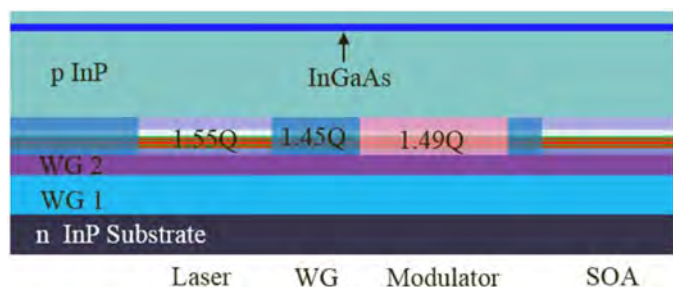


Fig. 6. Schematic of the QWI-based high-power PIC transmitter.

PIC transmitter with S1. The quantum wells outside the gain regions were removed by wet etch. A SGDBR laser design was employed for widely tunable range. Franz-Keldysh absorption based modulator works at reverse bias, as the tilting of the bands increase the tunneling probability when electrical field increases.

Epitaxial structure S2 was optimized with a thick lower waveguide layer (1.03Q) for low confinement in SOA. If OQW platform was used for S2, the active/passive interface will experience significant mode mismatch (as shown in Fig. 5). To reduce the interface discontinuity, QWI platform is preferred. Besides, QWI technique enables efficient EAM, thus eliminate the tradeoff between modulation efficiency and insertion loss.

A schematic of QWI-based high power PIC transmitter is demonstrated in Fig. 6. A two-step anneal process were developed after a single P⁺ implantation. The sample was annealed to reach a desire bandgap for efficient electro-absorption modulation, then the InP buffer layer was removed in the modulator region. The bandgap in passive region, where the buffer layer were intact, will be further blue-shifted with additional

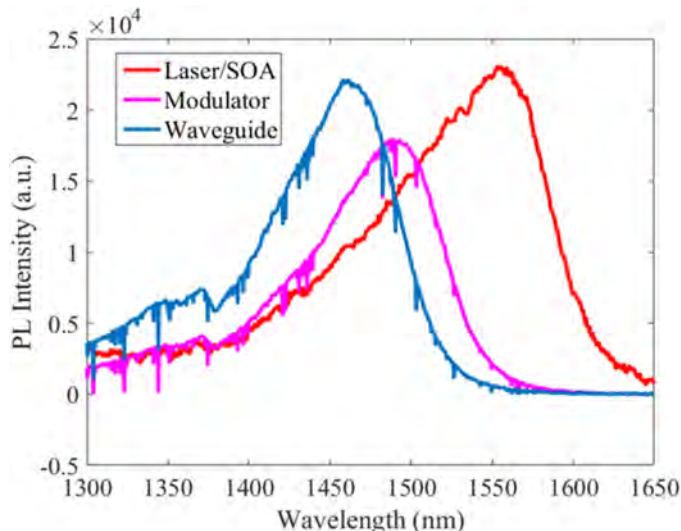


Fig. 7. Photoluminescence of the different regions in S2.

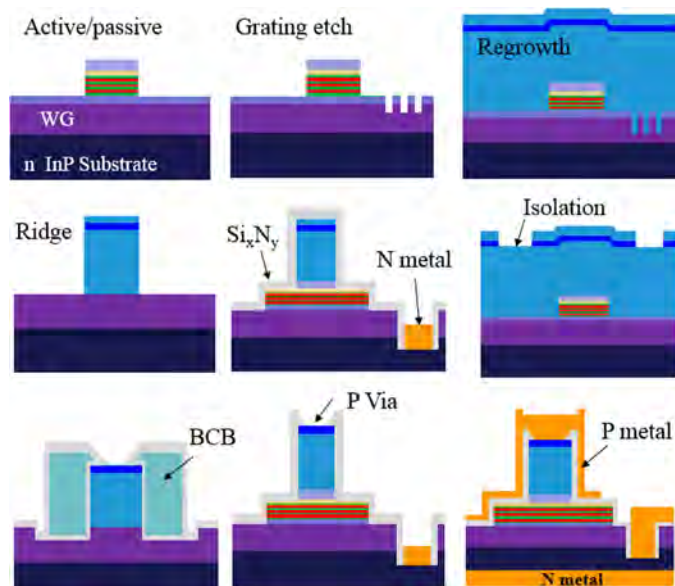


Fig. 8. Fabrication flow for OQW-based transmitter.

annealing. As shown Fig. 7, PL peaks in the gain section, EAM and passive waveguide are 1550 nm, 1490 nm and 1450 nm, respectively.

The fabrication process for the OQW-based and QWI-based PIC transmitters are similar except for the active/passive definition. The fabrication flow for OQW-based PIC transmitter is shown in Fig. 8. Grating mirrors were patterned by electron beam lithography and dry etched with chlorine-based ion beam etching. This was followed by a 'blanket' regrowth of the InP cladding and p+ InGaAs contact layer. The waveguide ridges were then formed in the [110] direction by using inductively coupled plasma dry etch and a cleanup wet etch to form smooth vertical sidewalls. Topside n-metal (Ni/AuGe/Ni/Au) were deposited. The p+ InGaAs contact layer was removed between

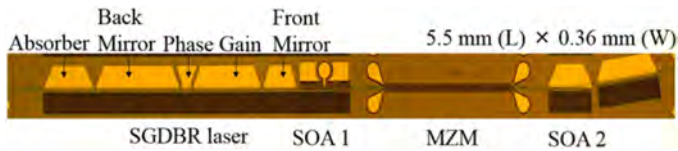
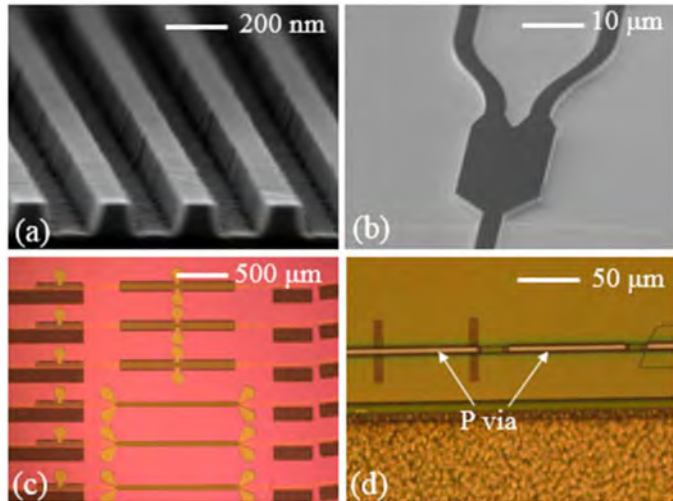


Fig. 9. Microscope image of fabricated OQW-based PIC transmitter.


 Fig. 10. Microscope images at various stages of the fabrication process of OQW-based transmitter: (a) The sampled gratings of the front mirror of the laser; (b) Top view of a 1×2 MMI structure; (c) BCB patterns for high-speed SOAs and MZMs; (d) P vias on top of ridges.

different components by wet etching to provide some electrical isolation. To reduce parasitic pad capacitance for the high-speed SOA and modulators, photosensitive Benzocyclobutene (BCB) was used in such regions. Ti/Pt/Au was deposited for p contacts. Next, the fabricated samples were thinned to less than $180\text{-}\mu\text{m}$ thickness and backside Ti/Pt/Au n-metal was deposited on the thinned wafers. The cleaved PICs were then solder mounted to ceramic carriers and wire-bonded for characterization.

IV. OFFSET QUANTUM WELL-BASED TRANSMITTER

The fabricated OQW-based PIC transmitter is shown in Fig. 9. It consists of a widely tunable SGDBR laser, a high-speed SOA (SOA 1), a MZM and a high-power two-section output booster SOA (SOA 2). The waveguide at the output is angled with respect to the chip facet to reduce the reflectivity of this interface. The transmitter has a footprint of $5.5\text{ mm} \times 0.36\text{ mm}$. The microscope images at various stages of the fabrication process are demonstrated in Fig. 10.

The five-section widely tunable SGDBR laser consists of an active gain section, a front SGDBR mirror, a back SGDBR mirror, a phase section, and a rear absorber (see Fig. 11). The SGDBR laser has a five-period front sampled grating mirror with $4\text{-}\mu\text{m}$ wide bursts and $68.5\text{-}\mu\text{m}$ period, a 12-period back sampled grating mirror with $6\text{-}\mu\text{m}$ wide bursts and $61.5\text{-}\mu\text{m}$ period [42].

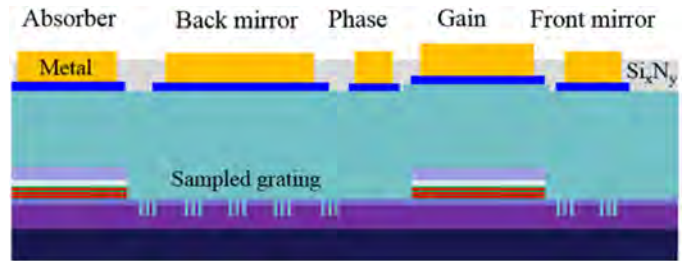


Fig. 11. Schematic of the five-section SGDBR laser.

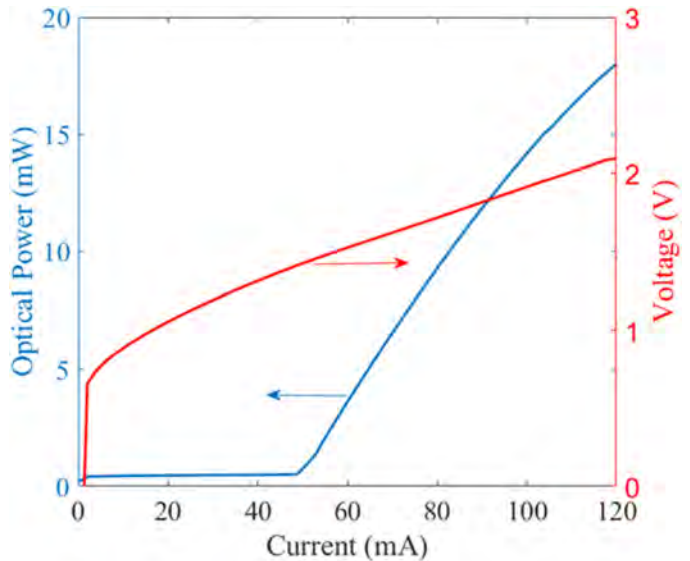


Fig. 12. SGDBR laser LIV curve (with CW current source) measured by using the SOA 1 as a photodiode.

To measure the light-current-voltage (LIV) characteristics, the reversed-biased high-speed integrated SOA (SOA 1) was used as an on-chip photodetector (estimated responsivity 0.9 A/W). The LIV curve of the SGDBR laser is shown in Fig. 12, demonstrating a threshold current of 45 mA and an output optical power of 15 mW at a gain section current of 100 mA . Laser spectrum near 1550 nm is shown in Fig. 13, the side mode suppression ratio (SMSR) is 55 dB . The tuning characteristics of the SGDBR laser are illustrated in Fig. 14 and Fig. 15, which present the emission wavelength and SMSR at various tuning conditions. Fig. 15 shows the ‘supermode’ boundaries and suggests that the width of the SMSR degradation between switching modes is very small. By adjusting the injected current in the front and back mirrors, the emission wavelength was tuned from 1521 nm to 1565 nm , covering more than the entire C-band. Across the entire tuning range, $> 45\text{ dB}$ SMSR was maintained.

There are two SOAs in this transmitter: a high-speed SOA (SOA 1) for amplification/modulation and a two-section booster SOA (SOA 2) with curved/angled and flared ridge waveguides. SOA 1 is $3\text{ }\mu\text{m}$ wide and $400\text{ }\mu\text{m}$ long. It is placed after the laser and before the 1-mm long MZM, and could also be used for modulation. Fig. 16 shows the gain characteristics of the

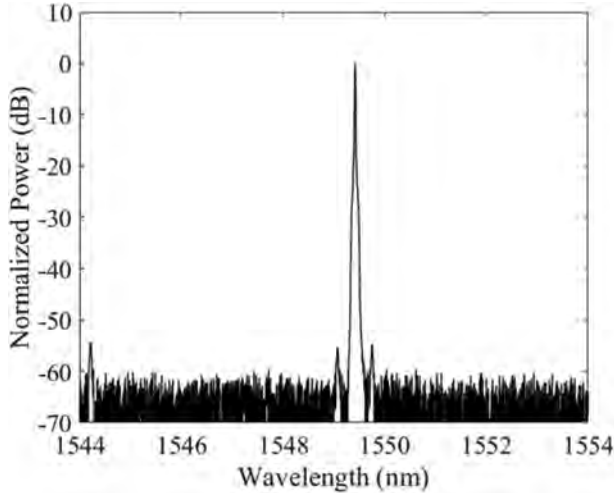


Fig. 13. Lasing spectrum near 1550 nm with a 55-dB SMSR measured by an optical spectrum analyzer with a resolution bandwidth of 0.02 nm.

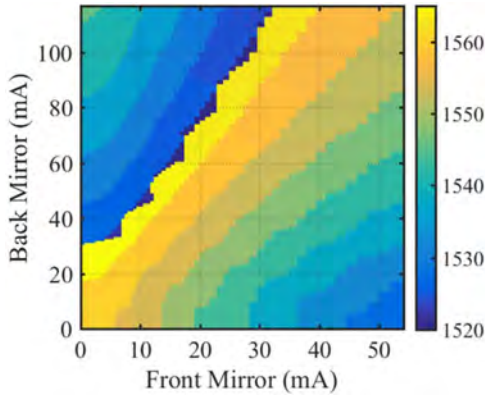


Fig. 14. Emission wavelength (nm) at various tuning conditions.

high-speed SOA at different input power levels. A gain of 6 dB is achieved at a current density of 10 kA/cm^2 , which is sufficient to compensate for the modulator insertion loss. The output booster SOA (SOA 2) is constructed with two separate sections that can be pumped with different injection current levels. The lengths of the two sections are 350 and 500 μm , respectively. The first section is 3- μm wide and the second section linearly flares from 3- μm to 5- μm wide.

The optical output was coupled to an integrating sphere to measure the off-chip power. Fig. 17 shows the off-chip power versus the current density in the flared-waveguide section of SOA 2. The current of the laser gain section, the SOA 1, and the first section of the SOA 2 are 150 mA, 110 mA and 90 mA, respectively. The maximum output power with the above DC biasing is 14.5 dBm (28 mW).

To measure the high-speed performance of the OQW-based transmitter, one arm of the MZM was wire bonded to a 50- Ω RF feeding transmission line and on the other side to a 50- Ω load mounted to the ceramic carrier. Fig. 18 shows the eye diagrams from 2 Gps to 7 Gbps non-return-to-zero (NRZ) on-off keying

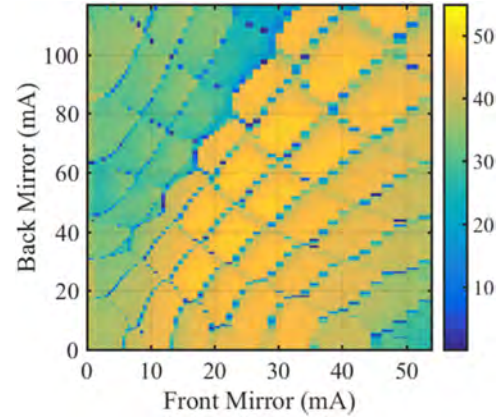


Fig. 15. Side mode suppression ratio (dB) at various tuning conditions.

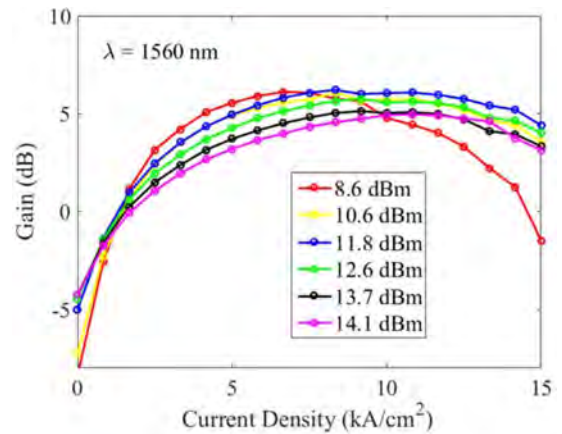


Fig. 16. Gain as a function of current density for the high-speed SOA ($3 \mu\text{m} \times 400 \mu\text{m}$) with different input power levels at a wavelength of 1560 nm.

(OOK) modulation at a reverse bias of -2.2 V and 3 V signal amplitude (V_{pp}).

V. QUANTUM WELL INTERMIXING-BASED TRANSMITTER

Fig. 19 demonstrates the schematic of a high-power transmitter integrated with ultralow-confinement SOA design. The full transmitter contains two stages: stage 1 consists of a laser, an EAM and two SOAs (SOA 1 and SOA 2) with relatively high confinement ($\Gamma = 3\% \sim 4\%$); Stage 2 features with a transition gain section (SOA 3), and an ultralow-confinement SOA (SOA 4). In stage 1, different elements are integrated by QWI. Transition gain section in stage 2 is a simple linear width taper. The integration of SOA 3 and SOA 4 will just add one additional etch process.

Since the epitaxial structure S2 was optimized for high-power SOA, the performance of laser and EAM may be degraded with the same material. Therefore, our first step is to test the performance of Stage 1, which is similar to the OQW-based transmitter in Sec. IV. Fig. 20 shows the microscope image of the fabricated PIC transmitter, which has a footprint of $3.5 \text{ mm} \times 0.36 \text{ mm}$. It consists of a DBR laser, a high-speed SOA (SOA 1), an EAM,

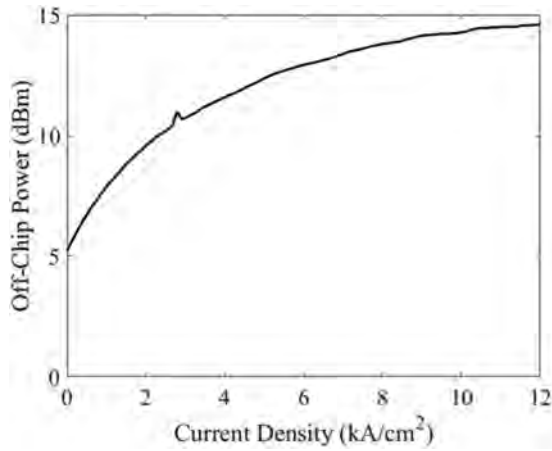


Fig. 17. Off-chip optical power of the PIC transmitter versus the current density in the second section of the booster SOA.

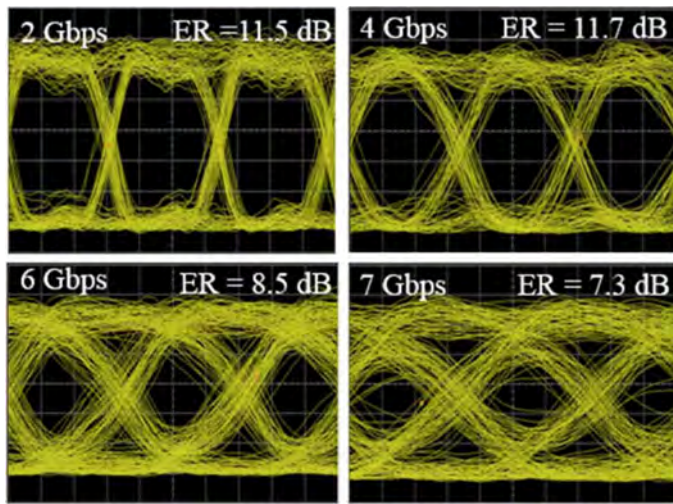


Fig. 18. Eye diagrams of OQW-based transmitter with NRZ OOK modulation at a data rate up to 7 Gbps.

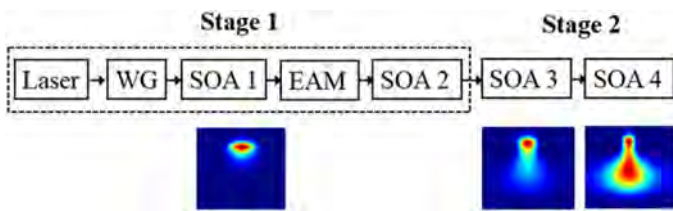


Fig. 19. Schematic of a high-power PIC transmitter with integrated ultralow-confinement SOA design.

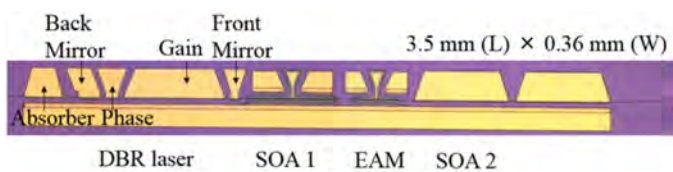


Fig. 20. Microscope image of fabricated QWI-based PIC transmitter comprising of a five-section DBR laser, a 250- μ m long EAM, and two high-power two-section output booster SOA (SOA 2).

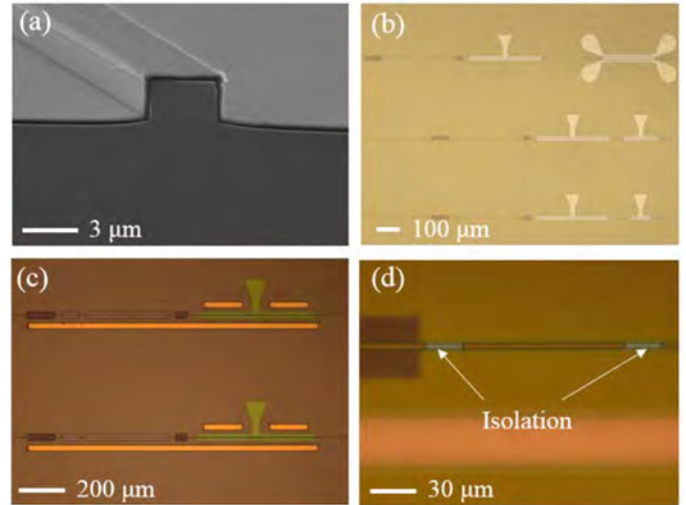


Fig. 21. SEM images at various stages of the fabrication process: (a) The dry-etched ridge waveguide; (b) Passivation etch for modulators; (c) N metal deposition; (d) Isolation between the back mirror and the phase section.

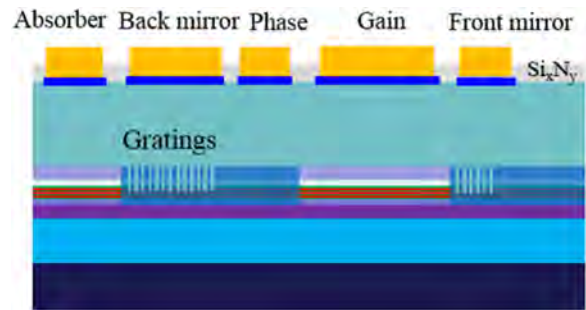


Fig. 22. Schematic of the five-section DBR laser.

and a high-power two-section output booster SOA (SOA 2). The images at various stages of the fabrication process are shown in Fig. 21.

The DBR laser consists of a rear absorber, a back DBR mirror, a phase section, an active gain section, and a front DBR mirror. The lengths of the front and back mirrors are 50 μ m and 120 μ m, respectively. The lengths are longer than DBR designs with a conventional high confinement epitaxial structure. In conventional structure, the grating etch will not significantly alter the optical modes, so a deep etch can be performed to achieve high coupling efficiency (κ). The reflectivity of the grating can be written as:

$$r_g = \tanh(\kappa L_g) \tag{3}$$

where L_g is the length of the grating mirror. With high κ , higher reflectivity can be achieved, thus reducing the loss in the mirror. However, in the QWI-based transmitter if the quantum well layers were all etched off, the optical mode would “leak” into the thick waveguide layer (WG2) and result in extra loss (see Fig. 5). Therefore, the etch depth into the quantum wells should be well controlled. In this case, the QWs were only partially etched (as shown in Fig. 22).

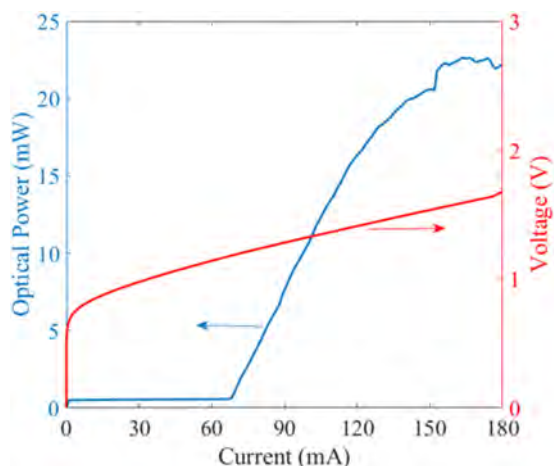


Fig. 23. DBR laser LIV curve (with CW current source) measured by using the SOA 1 as a photodiode.

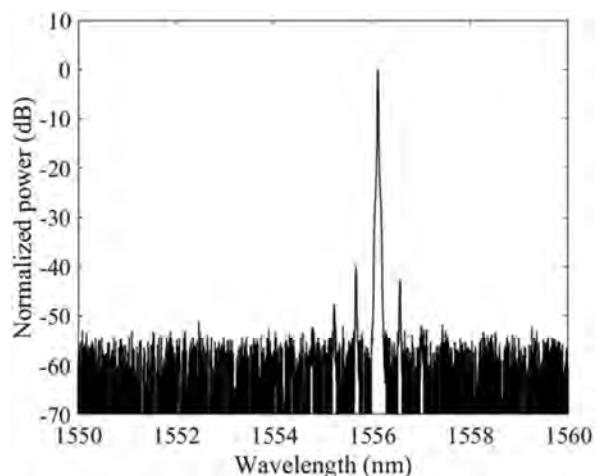


Fig. 24. Lasing spectrum near 1556 nm with a 40-dB SMSR measured by an optical spectrum analyzer with a resolution bandwidth of 0.02 nm.

The LIV characteristic of the DBR laser is plotted in Fig. 23, measured by exploiting the reverse bias SOA 1 as photodetector, which shows a threshold of 65 mA. At a current of 150 mA, the optical power is 20 mW. The SMSR near 1556 nm is 40 dB (see Fig. 24).

SOA1 and each section of SOA 2 are 3- μm wide and 500- μm long. To test the gain characteristic, the laser gain section is biased at 150 mA and SOA 1 at 90 mA. Gain of SOA 2 as a function of the current density in the second section of SOA 2 is plotted in Fig. 25. Here the jumps in the measured SOA gain are ascribed to thermal crosstalk induced mode hopping of the laser.

Fig. 26 shows the off-chip power versus the current density in the second section of the booster SOA (SOA 2). The current of the laser gain section, the SOA 1, and the first section of the SOA 2 are 150 mA, 90 mA and 140 mA, respectively. The maximum output power with the above DC biasing is 19.4 dBm (87 mW). Fig. 27 shows the eye diagram for NRZ OOK modulation up to 20 Gbps.

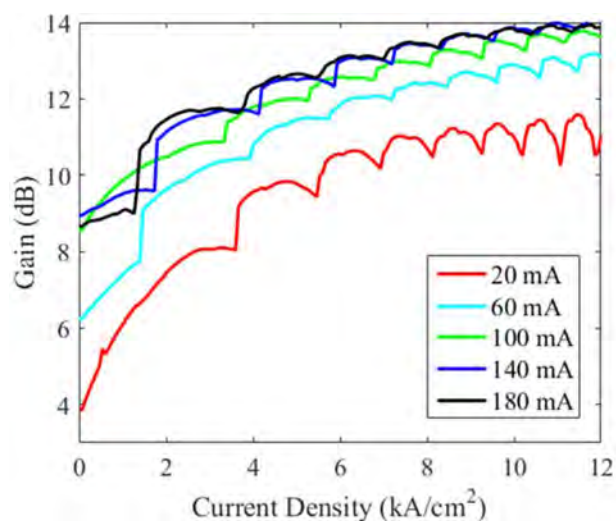


Fig. 25. Gain of SOA 2 as a function of current density in the second section as the current in the first section is increased from 20 to 180 mA.

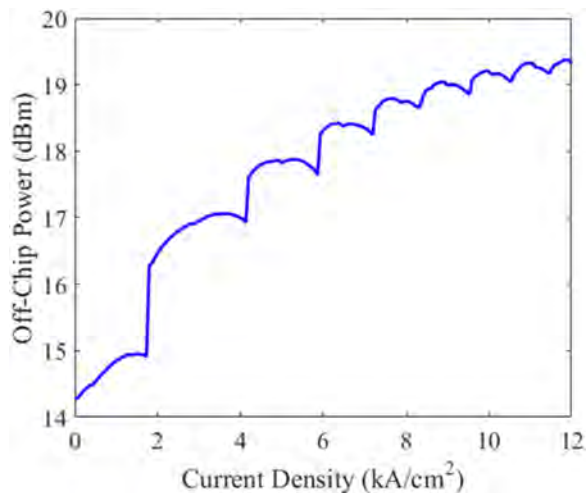


Fig. 26. Off-chip optical power of the PIC transmitter versus the current density in the second section of the booster SOA.

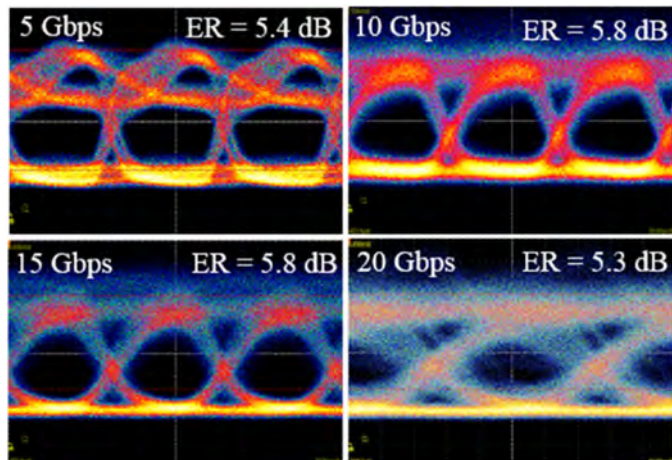


Fig. 27. Eye diagrams of QWI-based transmitter with NRZ OOK modulation at a data rate up to 20 Gbps.

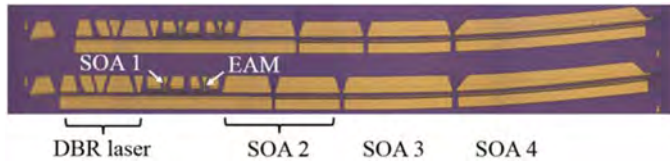


Fig. 28. Microscope image of high-power PIC transmitters with integrated ultralow-confinement SOAs.

Compared with the OQW-based transmitter, the QWI-based one demonstrated both higher optical power and higher data rate, the first enabled by an optimized epi structure, while the second achieved through a compact and efficient EAM. In future work, the fabricated high-power PIC transmitter with integrated ultralow confinement SOA will be characterized. As shown in Fig. 28, the footprint of each transmitter is $8 \text{ mm} \times 0.36 \mu\text{m}$. With the ultralow-confinement SOA at the output, $>25 \text{ dBm}$ off-chip optical power is expected.

VI. CONCLUSION

In this work, InP-based PIC transmitters were fabricated and characterized for high optical output power. The OQW-based transmitter is tunable from 1521 nm to 1565 nm while maintaining $>45 \text{ dB SMSR}$ across this range. Measured off-chip power of 14.5 dBm and 7-Gbps data rate were demonstrated. A QWI-based transmitter with new epitaxial structure was employed for higher optical output power, which shows 19.5 dBm output power and up to 20 Gbps operation. The new epitaxial material enables ultralow confinement SOA designs and monolithic integration of the SOA with DBR laser, EAM, and passive waveguide.

REFERENCES

- [1] L. A. Coldren *et al.*, "High performance InP-based photonic ICs—A tutorial," *J. Lightw. Technol.*, vol. 29, no. 4, pp. 554–570, Feb. 2011.
- [2] D. F. Welch *et al.*, "Large-scale InP photonic integrated circuits: Enabling efficient scaling of optical transport networks," *IEEE J. Sel. Top. Quantum Electron.*, vol. 13, no. 1, pp. 22–31, Jan./Feb. 2007.
- [3] J. Klamkin *et al.*, "Indium phosphide photonic integrated circuits: Technology and applications," in *Proc. IEEE BiCMOS Compound Semicond. Integr. Circuits Technol. Symp.*, 2018, pp. 8–13.
- [4] T. Koch and U. Koren, "Semiconductor lasers for coherent optical fiber communications," *J. Lightw. Technol.*, vol. 8, no. 3, pp. 274–293, Mar. 1990.
- [5] M. M. Dummer, J. Klamkin, A. Tauke-Pedretti, and L. A. Coldren, "40 Gb/s field-modulated wavelength converters for all-optical packet switching," *IEEE J. Sel. Topics Quantum Electron.*, vol. 15, no. 3, pp. 494–503, May/June 2009.
- [6] S. C. Nicholes *et al.*, "The world's first InP 8×8 monolithic tunable optical router (MOTOR) operating at 40 Gbps line rate per port," in *Proc. Conf. Opt. Fiber Commun.*, 2009, Paper PDPB1.
- [7] J. Summers *et al.*, "40 Channels \times 57 Gb/s monolithically integrated InP-based coherent photonic transmitter," in *Proc. Eur. Conf. Opt. Commun.*, 2014, Paper P.2.5.
- [8] Y. Kawamura, K. Wakita, Y. Yoshikuni, Y. Itaya, and H. Asahi, "Monolithic integration of a DFB laser and an MQW optical modulator in the 1.5 μm wavelength range," *IEEE J. Quantum Electron.*, vol. QE-23, no. 6, pp. 915–918, Jun. 1987.
- [9] M. Suzuki *et al.*, "Monolithic integration of InGaAsP/InP distributed feedback laser and electroabsorption modulator by vapor phase epitaxy," *J. Lightw. Technol.*, vol. LT-5, no. 9, pp. 1277–1285, Sep. 1987.

- [10] E. J. Skogen *et al.*, "Widely tunable negative-chirp SG-DBR laser/EAM-modulated transmitter," *J. Lightw. Technol.*, vol. 23, no. 1, pp. 80–86, Jan. 2005.
- [11] L. A. Coldren, "Monolithic tunable diode lasers," *IEEE J. Sel. Topics Quantum Electron.*, vol. 6, no. 6, pp. 988–999, Nov./Dec. 2000.
- [12] V. Jayaraman, Z. M. Chuang, and L. A. Coldren, "Theory, design, and performance of extended tuning range semiconductor lasers with sampled gratings," *IEEE J. Quantum Electron.*, vol. 29, no. 6, pp. 1824–1834, Jun. 1993.
- [13] R. Nagarajan *et al.*, "Large-scale photonic integrated circuits," *IEEE J. Sel. Top. Quant. Electron.*, vol. 11, no. 1, pp. 50–65, Jan./Feb. 2005.
- [14] V. Lal *et al.*, "Extended C-band tunable multi-channel InP-based coherent transmitter PICs," *J. Lightw. Technol.*, vol. 35, no. 7, pp. 1320–1327, Apr. 2017.
- [15] H. Zhao *et al.*, "Indium phosphide photonic integrated circuits for free space optical links," *IEEE J. Sel. Top. Quant. Electron.*, vol. 24, no. 6, Nov./Dec. 2018, Art. no. 6101806.
- [16] H. Zhao *et al.*, "Integrated indium phosphide transmitter for free space optical link," in *Proc. Adv. Photon.*, 2018, Paper ITu4B.6.
- [17] S. Iezekiel, M. Burla, J. Klamkin, D. Marpaung, and J. Capmany, "RF engineering meets optoelectronics: Progress in integrated microwave photonics," *IEEE Microw. Mag.*, vol. 16, no. 8, pp. 28–45, Sep. 2015.
- [18] J. A. Nanzer, A. Wichman, J. Klamkin, T. P. McKenna, and T. R. Clark, "Millimeter-wave photonics for communications and phased arrays," *Fiber Integr. Opt.*, vol. 34, no. 4, pp. 159–174, Jul. 2015.
- [19] A. Ramaswamy *et al.*, "Integrated coherent receivers for high-linearity microwave photonic links," *J. Lightw. Technol.*, vol. 26, no. 1, pp. 209–216, Jan. 2008.
- [20] S. Arafin *et al.*, "Towards chip-scale optical frequency synthesis based on optical heterodyne phase-locked loop," *Opt. Express*, vol. 25, no. 2, pp. 681–695, 2017.
- [21] B. Isaac *et al.*, "Indium phosphide photonic integrated circuit transmitter with integrated linewidth narrowing for laser communications and sensing," presented at the IEEE Int. Semicond. Laser Conf., Santa Fe, NM, USA, 2018, Paper MC.5.
- [22] M. A. Krainak and A. W. Yu, "1047-nm master oscillator power amplifier free-space optical communications laser transmitter," *IEEE J. Quantum Electron.*, vol. 32, no. 1, pp. 112–117, Jan. 1996.
- [23] D. O. Caplan, "Laser communication transmitter and receiver design," *J. Opt. Fiber Commun.* vol. 4, pp. 225–362, 2007.
- [24] H. Hemmati, A. Biswas, and I. B. Djordjevic, "Deep-space optical communications: Future perspectives and applications," *Proc. IEEE*, vol. 99, no. 11, pp. 2020–2039, Aug. 2011.
- [25] H. Zhao *et al.*, "Widely tunable integrated laser transmitter for free space optical communications," presented at the IEEE Int. Semicond. Laser Conf., Santa Fe, NM, USA, 2018, Paper MC.5.
- [26] D. M. Boroson, J. J. Scozzafava, D. V. Murphy, B. S. Robinson, and M. I. T. Lincoln, "The lunar laser communications demonstration (LLCD)," in *Proc. 3rd IEEE Int. Conf. Space Mission Challenges Inf. Technol.*, 2009, pp. 23–28.
- [27] D. J. Israel, B. L. Edwards, and J. W. Staren, "Laser communications relay demonstration (LCRD) update and the path towards optical relay operations," in *Proc. IEEE Aerosp. Conf.*, 2017, pp. 1–6.
- [28] D. Caplan, "High-performance free-space laser communications and future trends," presented at the Opt. Amplifiers Their Appl., 2005, Paper TuB1.
- [29] H. Zhao *et al.*, "High-power integrated indium phosphide transmitter for free space optical communications," presented at the IEEE Conf. Lasers Electro-Optics (CLEO), 2018, Paper JW2A.52.
- [30] P. W. Juodawlkis *et al.*, "High-power, low-noise 1.5- μm slab-coupled optical waveguide (SCOW) emitters: Physics, devices, and applications," *IEEE J. Sel. Top. Quant. Electron.*, vol. 17, no. 6, pp. 1698–1714, Nov./Dec. 2011.
- [31] J. Klamkin *et al.*, "High-output saturation power variable confinement slab-coupled optical waveguide amplifier," presented at the Opt. Fiber Commun. Conf. /Nat. Fiber Optic Eng. Conf., Los Angeles, CA, USA, 2011, Paper JThA025.
- [32] M. Faugeron *et al.*, "High power three-section integrated master oscillator power amplifier at 1.5 μm ," *IEEE Photon. Technol. Lett.*, vol. 27, no. 13, pp. 1449–1452, Jul. 2015.
- [33] J. P. Donnelly *et al.*, "High-power 1.3- μm InGaAsP-InP amplifiers with tapered gain regions," *IEEE Photon. Technol. Lett.*, vol. 8, no. 11, pp. 1450–1452, Nov. 1996.

- [34] G. Bendeli, K. Komori, S. Arai, and Y. Suematsu, "A new structure for high power TW-SLA (Travelling wave semiconductor laser amplifier)," *IEEE Photon. Technol. Lett.*, vol. 3, no. 1, pp. 42–44, Jan. 1991.
- [35] F. Koyama, K.-Y. Liou, A. G. Dentai, T. Tanbun-ek, and C. A. Burrus, "Multiple-quantum-well GaInAs/GaInAsP tapered broad-area amplifiers with monolithically integrated waveguide lens for high-power applications," *IEEE Photon. Technol. Lett.*, vol. 5, no. 8, pp. 916–919, Aug. 1993.
- [36] J. J. Plant *et al.*, "1.5- μm InGaAsP-InP slab-coupled optical waveguide lasers," *IEEE Photon. Technol. Lett.*, vol. 17, no. 4, pp. 735–737, Apr. 2005.
- [37] J. Klamkin *et al.*, "Direct modulation and wavelength stabilization of high power slab-coupled optical waveguide lasers," in *Proc. Conf. Lasers Electro-Opt.*, 2010, Paper CWE4.
- [38] M. Aoki *et al.*, "Novel structure MQW electroabsorption modulator/DFB-laser integrated device fabricated by selective area mcvd growth," *Electron. Lett.*, vol. 27, no. 23, pp. 2138–2140, 1991.
- [39] T. Tanbun-Ek *et al.*, "DFB lasers integrated with Mach-Zehnder optical modulator fabricated by selective area growth MOVPE technique," *IEEE Photon. Technol. Lett.*, vol. 7, no. 9, pp. 1019–1021, Sep. 1995.
- [40] B. Mason *et al.*, "40-Gb/s tandem electroabsorption modulator," *IEEE Photon. Technol. Lett.*, vol. 14, no. 1, pp. 27–29, Jan. 2002.
- [41] J. J. M. Binsma *et al.*, "MOVPE waveguide regrowth in InGaAsP/InP with extremely low butt-joint loss," in *Proc. Annu. Symp. IEEE/LEOS*, 2001, pp. 245–248.
- [42] M. Smit *et al.*, "An introduction to InP-based generic integration technology," *Semicond. Sci. Technol.*, vol. 29, no. 8, Jun. 2014, Art. no. 083001.
- [43] L. M. Augustin *et al.*, "InP-based generic foundry platform for photonic integrated circuits," *IEEE J. Sel. Topics Quantum Electron.*, vol. 24, no. 1, Jan./Feb. 2018, Art. no. 6100210.
- [44] J. S. Barton, "The integration of Mach-Zehnder modulators with sampled grating DBR lasers," Ph.D. dissertation, Elect. Comput. Eng., University of California Santa Barbara, Santa Barbara, CA, USA, 2004.
- [45] A. M. Tauke-Pedretti, "Monolithic separate absorption and modulation Mach-Zehnder wavelength converters," Ph.D. dissertation, Elect. Comput. Eng., University of California Santa Barbara, Santa Barbara, CA, USA, 2007.
- [46] E. J. Skogen, J. S. Barton, S. P. DenBaars, and L. A. Coldren, "A quantum-well-intermixing process for wavelength-agile photonic integrated circuits," *IEEE J. Sel. Top. Quant. Electron.*, vol. 8, no. 4, pp. 863–869, Jul./Aug. 2002.
- [47] J. J. Plant *et al.*, "Compact external-cavity semiconductor mode-locked laser with quantum-well-intermixed modulator and saturable absorber," in *Proc. IEEE Photon. Soc. 24th Annu. Meeting*, Arlington, VA, USA, 2011, Paper ThK3.

Hongwei Zhao received the B.S. degree from the Huazhong University of Science and Technology, Wuhan, China, in 2008, and the M.S. degree from the Institute of Semiconductors, Chinese Academy of Sciences, Beijing, China, in 2011. She is currently working toward the Ph.D. degree in the Integrated Photonics Lab, Electrical and Computer Engineering Department, University of California Santa Barbara, Santa Barbara, CA, USA. Her research interests include silicon photonics with emerging materials (such as graphene, indium tin oxide, and indium silicon oxide), compound semiconductor photonic integrated circuits, InP-based photonic integrated circuits for free space communications, and monolithic integration of III-V lasers on Si substrate.

Sergio Pinna received the B.Sc. and M.Sc. degrees in telecommunications engineering from University of Pisa, Pisa, Italy, and the Ph.D. degree in innovative technologies from Scuola Superiore Sant'Anna, Pisa, Italy, in 2008, 2010, and 2014, respectively. From November 2010 to December 2015, he was a Fellow with CNIT, National Photonic Networks Laboratory, Pisa, Italy. In 2014, he was a Visiting Researcher with the Integrated Photonics Laboratory, Boston University, Boston, MA, USA. Since January 2016, he has been a Research Fellow with TeCIP Institute, Scuola Superiore Sant'Anna, Pisa, Italy, within the Digital and Microwave Photonics Group. In 2017, he joined the Integrated Photonics Laboratory, University of California Santa Barbara, as a Postdoctoral Research Associate. His research interests include integrated photonics for microwave and LiDAR applications.

Fengqiao Sang received the B.S. degree in electrical engineering from Drexel University, Philadelphia, PA, USA. He is currently working toward the Ph.D. degree in the Electrical and Computer Engineering Department, University of California Santa Barbara, Santa Barbara, CA, USA. His research interests include photonic integrated circuits and semiconductor lasers.

Bowen Song is from Shanxi, China. He received the Bachelor of Engineering degree from the School of Electronic Engineering and Optoelectronic Technology, Nanjing University of Science and Technology, Nanjing, China, in 2012, and the Master of Science degree in developing nano-patterned sapphire substrate for AlGaIn-based deep UV LEDs from Wide Bandgap Semiconductor Laboratory, Boston University, Boston, MA, USA, in 2014. He is currently working toward the Ph.D. degree in the Electrical and Computer Engineering Department, University of California Santa Barbara, Santa Barbara, CA, USA. His research interests include electronic-photonic integration, integrated photonics, and integrated LiDAR.

Simone Tommaso Šuran Brunelli received the bachelor's degree in industrial engineering and the master's degree in materials engineering from the Università degli Studi di Trieste, Trieste, Italy. After a fellowship at Elettra Sincrotrone, working on carbon nanotube synthesis and photoelectron spectroscopy, he joined the Integrated Photonics Laboratory, University of California Santa Barbara, Santa Barbara, CA, USA, as a Ph.D. student. His current research focuses on metal organic chemical vapor deposition of III-V semiconductors for nanoelectronic and photonic applications including low-power tunneling transistors.

Larry A. Coldren (S'67–M'72–SM'77–F'82–LF'12) received the Ph.D. degree in electrical engineering from Stanford University, Stanford, CA, USA, in 1972. After 13 years in the research area with Bell Laboratories, he joined the University of California at Santa Barbara (UCSB), CA, USA, in 1984. He is currently the Fred Kavli Professor of optoelectronics and sensors and holds appointments with the Department of Materials and the Department of Electrical and Computer Engineering, University of California Santa Barbara. From 2009 to 2011, he was the acting Dean of the College of Engineering, University of California Santa Barbara. In 1990, he cofounded Optical Concepts, later acquired as Gore Photonics, to develop novel VCSEL technology, and, in 1998, he cofounded Agility Communications, later acquired by JDSU (now Lumentum), to develop widely tunable integrated transmitters. At UCSB, he worked on multiple-section widely tunable lasers and efficient vertical-cavity surface-emitting lasers (VCSELs). More recently, his group has developed high-performance InP-based photonic integrated circuits and high-speed, high-efficiency VCSELs. He has authored or coauthored more than a thousand journal and conference papers, eight book chapters, a widely used textbook, and 63 issued patents. He is a Fellow of OSA, and the National Academy of Inventors, as well as a member of the National Academy of Engineering. He was the recipient of the 2004 John Tyndall Award, the 2009 Aron Kressel Award, the 2014 David Sarnoff Award, the 2015 IPRM Award, and the 2017 Nick Holonyak, Jr. Award.

Jonathan Klamkin (SM'15) received the B.S. degree from Cornell University, Ithaca, NY, USA, and the M.S. and Ph.D. degrees from the University of California Santa Barbara (UCSB), Santa Barbara, CA, USA. From 2008 to 2011, he was a member of the Technical Staff in the Electro-Optical Materials and Devices Group, MIT Lincoln Laboratory, Lexington, MA, USA. From 2011 to 2013, he was an Assistant Professor with the Institute of Communication, Information and Perception Technologies, Scuola Superiore Sant'Anna, Pisa, Italy. From 2013 to 2015, he was an Assistant Professor of Electrical and Computer Engineering (ECE) and Materials with Boston University, Boston, MA, USA. In 2015, he joined the ECE Department, University of California Santa Barbara, where he is currently an Associate Professor and Director of the UCSB Nanotech. He has authored or coauthored more than 180 journal and conference papers, and holds three patents. He is an Associate Editor of *Photonics Technology Letters*, Vice Chair of the Microwave Theory and Techniques Society Subcommittee on Microwave Photonics, and Steering Committee Member of the *Journal of Lightwave Technology*. He was the Program Chair of the Integrated Photonics Research, Silicon and Nanophotonics Conference, in 2017, and the General Chair of the same conference, in 2018. He or his group members were the recipient of best paper awards at the 2006 Conference on Optoelectronic and Microelectronic Materials and Devices, 2007 Microwave Photonics Conference, and 2017 Asia Communications and Photonics Conference. He was the recipient of the NASA Early Career Faculty Award and the DARPA Young Faculty Award. He is a Senior Member of OSA.

I. Photonic Integrated Circuits

D. Signal Processing

Wideband and Continuously Tunable Microwave Photonic Phase Shifter Based on an Active InP/InGaAsP Microring Resonator

Jian Tang,^{1,2,3} Ming Li,^{2,3} Robert S. Guzzon,⁴ Larry A. Coldren,⁴ and Jianping Yao^{1,*}

1. Microwave Photonics Research Laboratory
School of Electrical Engineering and Computer Science, University of Ottawa
Ottawa, Ontario K1N 6N5, Canada

2. State Key Laboratory on Integrated Optoelectronics,
Institute of Semiconductors, Chinese Academy of Sciences
Beijing 100083, China

3. School of Electronics, Electrical and Communication Engineering
University of Chinese Academy of Sciences, Beijing 100049, China

4. Department of Electrical and Computer Engineering
University of California Santa Barbara
Santa Barbara, California 93116, USA

*Corresponding author: jpyao@uottawa.ca

Abstract—We propose and experimentally demonstrate a wideband and continuously tunable microwave photonic (MWP) phase shifter based on an active InP/InGaAsP microring resonator (MRR) incorporating two semiconductor optical amplifiers (SOAs) and a phase modulator (PM). By tuning the gain provided by the SOAs, the loss in the ring cavity can be compensated and the extinction ratio of a resonance is decreased to nearly 0 dB, while maintaining the optical phase shift range of nearly 2π within the resonance bandwidth. A theoretical analysis is performed. The key advantages of using the proposed MRR to achieve a microwave phase shifter are that the power variation at the output of the phase shifter is minimized during phase tuning and the microwave phase can be continuously tuned by tuning the PM in the MRR theoretically. The proposed phase shifter is experimentally demonstrated. A continuously tunable microwave phase shift over a phase tuning range of 291° from 5 GHz to 20 GHz by tuning the injection current to the PM is implemented. The microwave power variation is lower than 5 dB.

Keywords—integrated optics devices, ring resonators, phase shift.

I. INTRODUCTION

Microwave phase shifter is one of the most important devices that is widely used in modern microwave systems, such as Radar [1], wireless communications [2], 5G networks [3], and warfare systems [4]. Pure electronic microwave phase shifters are limited by the bandwidth and tunability which may not be able to meet the requirements needed by modern microwave systems [4-6]. Modern photonics, especially integrated photonics, with key features such as broad bandwidth, large tunability and small size can be employed to implement microwave photonic (MWP) phase shifters [6-9]. The most representative integrated device employed to implement an MWP phase shifter is a micro-ring resonator (MRR) [10-12]. By locating the optical carrier in the bandwidth of a resonance, a phase shift is introduced to the optical carrier. Then, by beating the optical carrier with a sideband, a phase shifted microwave signal with its phase shift translated from the optical carrier is generated. By cascading two MRRs on a silicon on insulator (SOI) platform, a maximum microwave phase shift range of 600° was achieved at a

microwave frequency of 40 GHz [13]. A high Q MRR based on aluminum nitride (AlN) material system was used to realize an MWP phase shifter. A phase shift range of 332° over a frequency range from 4 GHz to 25 GHz was demonstrated [14]. A cascaded MRRs based on silicon nitride (Si_3N_4) material system was also employed to demonstrate an MWP phase shifter with a 2π phase tunable range [15]. An MRR based on InP/InGaAsP material system has the key advantage of electrical pumped optical gain, which does not exist in the above-mentioned material systems, and thus has the ability to provide a loop gain to compensate for the loss. It makes an InP/InGaAsP-based MRR has an additional degree of flexibility to control its spectral response, thus making it more suitable for realizing an MWP phase shifter.

In this letter, we propose and experimentally demonstrate an add-drop type InP/InGaAsP material based MRR which is employed to realize a continuously tunable microwave phase shifter. Two semiconductor optical amplifiers (SOAs) and a phase modulator (PM) are integrated in the ring cavity to provide an optical gain and realize phase shift tuning, respectively. When the loss in the active MRR is compensated by the gain provided by the SOAs, the optical extinction ratio of a resonance is reduced to nearly 0 dB, while a large phase shift range in a resonance bandwidth is maintained almost unchanged. The problem that a large phase shift may result in a large microwave power variation for an MRR-based MWP phase shifter is solved. The key advantages of using the proposed active MRR to achieve an MWP phase shifter are that the power variation at the output of the phase shifter is minimized during phase tuning and the microwave phase can be continuously tuned by tuning the PM in the MRR theoretically. The proposed MRR-based MWP phase shifter is demonstrated experimentally. A continuously tunable microwave phase shift over a phase tuning range of 291° from 5 GHz to 20 GHz by tuning the injection current to the PM is implemented. The microwave power variation is lower than 5 dB.

II. PRINCIPLE

Figure 1 (a) shows the schematic of the proposed add-drop type InP/InGaAsP-based MRR. As can be seen the MRR has two SOAs (SOAs1-2) and a PM (PM0) in the cavity. Two tunable couplers (TCs) consist of two PMs (PM1 and PM2) and two multi-mode interferometer (MMI) 3-dB couplers. The

This work was supported by the Natural Sciences and Engineering Research Council of Canada (NSERC). Jian Tang was supported by the China Scholarship Council.

coupling ratio of each TC can be adjusted by tuning the injection currents to the PMs in a TC. By tuning the injection current to PM0 in the ring cavity, the resonance frequency of the MRR can be continuously tuned for tens GHz. In addition, four other SOAs (SOAs3-6) are integrated in the four straight waveguides which are mainly used to compensate for the coupling loss from the lens fiber to the chip. Note that the SOAs integrated on the chip can operate in two states. When an SOA is forward biased, it operates in the amplification states, while when an SOA is reverse biased, it operates as an optical absorber. Fig. 1 (b) shows the photograph of the proposed chip which is wire-bonded to a polychlorinated biphenyl carrier for the experimental measurement. Two lens fibers are used to couple the light into (or out from) the chip through the edge couplers integrated on the chip.

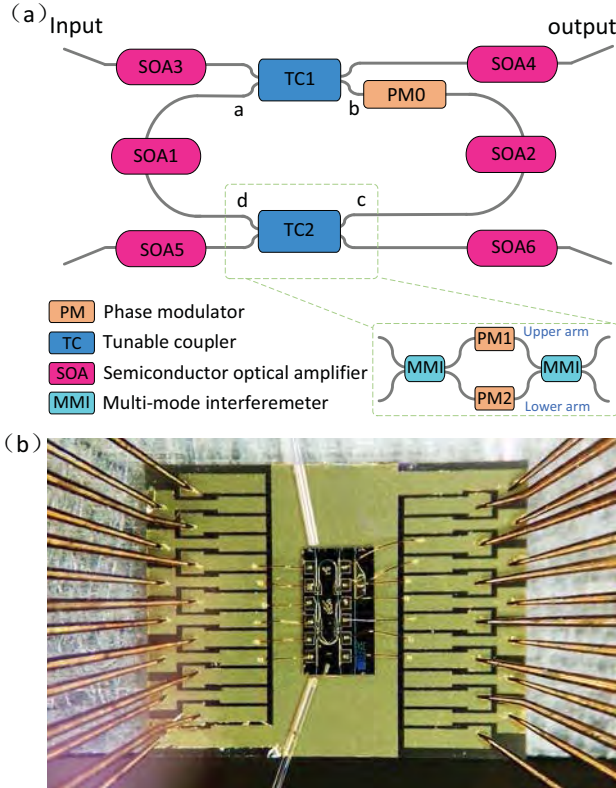


Fig. 1. (a) The schematic of the proposed active MRR. The inset shows the details of the tunable coupler. (b) The photograph of the proposed MRR chip.

To simplify the analysis, the self-coupling coefficients of the two TCs are regarded as constant over the frequency range and the coupling loss is ignored. By employing the transfer matrix method, the transfer function of the proposed add-drop type InP/InGaAsP-based MRR can be expressed as [16]

$$H(\omega) = \frac{t_{TC1} - t_{TC2}G_1G_2e^{-j\varphi(\omega)}}{1 - t_{TC1}t_{TC2}G_1G_2e^{-j\varphi(\omega)}} \quad (1)$$

where t_{TC1} and t_{TC2} are the self-coupling coefficients of TC1 and TC2, respectively. G_1 is the accumulated transmission gain from point d to point a and G_2 is the accumulated transmission gain from point b to point c. $\varphi(\omega) = \omega\tau$, ω is the angular frequency and τ is the one round trip time for the light transmitting in the ring circuit. The resonance frequency is given by $\omega\tau = 2n\pi$ (n is an integer). When PM0 in the ring circuit is tuned, τ is changed. Thus, the resonance frequency is changed. By tuning the gain

provided by SOA1 and SOA2, the loss in the ring resonator can be compensated. In this case, $t_{TC2}G_1G_2$ is close to unity. Then, Eq. (1) can be written as

$$T = \frac{t_{TC1} - e^{-j\varphi(\omega)}}{1 - t_{TC1}e^{-j\varphi(\omega)}} = -\frac{e^{-j\varphi(\omega)/2} - t_{TC1}e^{j\varphi(\omega)/2}}{e^{j\varphi(\omega)/2} - t_{TC1}e^{-j\varphi(\omega)/2}} \quad (2)$$

One can find that the expression in the numerator ($e^{-j\varphi(\omega)/2} - t_{TC1}e^{j\varphi(\omega)/2}$) is a complex conjugate of the expression in the denominator ($e^{j\varphi(\omega)/2} - t_{TC1}e^{-j\varphi(\omega)/2}$). Thus, the magnitude response (T) of the transmission is unity which can be written as

$$|T| = |H(\omega)|^2 = 1 \quad (3)$$

The phase response in transmission can be written as [11]

$$\phi(\omega) = \pi + 2 \tan^{-1} \left[\frac{(1 + t_{TC1}) \sin\left(\frac{1}{2}\varphi(\omega)\right)}{(1 - t_{TC1}) \cos\left(\frac{1}{2}\varphi(\omega)\right)} \right] \quad (4)$$

Thus, the phase shift range within the resonance maintains 2π theoretically when the $\varphi(\omega)$ increases from $(2n-1)\pi$ to $(2n+1)\pi$, n is an integer.

III. EXPERIMENTS

The proposed MRR is fabricated based on the InP/InGaAsP material system and the use of the MRR to achieve MWP phase shifter is experimentally evaluated. In the experiment, the self-coupling coefficient of TC1 is first measured. SOA3 is forward biased at an injection current of 20 mA to compensate for the coupling loss from the lens fiber to the chip. SOA4 is reverse biased with a voltage of -3 V to make it works as a photodetector (PD). By tuning the injection current from 0 mA to 7 mA which is applied to PM2 of TC1, the self-coupling coefficient is recorded, as shown in Fig. 2(a). The self-coupling coefficient of TC2 is measured in the same way, which is shown in Fig. 2(b). To obtain a small extinction ratio at the resonance bandwidth, the injection current applied to PM2 in TC2 is tuned to 2 mA to get a largest t_{TC2} .

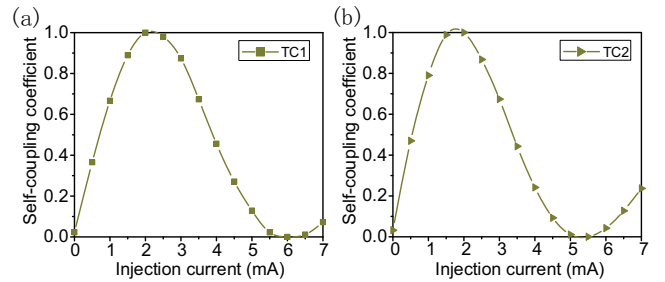


Fig. 2. Experimentally measured tunable self-coupling coefficients of TC1 and TC2.

Then, the transmission response of the MRR is characterized. The injection currents to SOA1 and SOA2 are set to 24 mA and 22 mA. The injection current to PM0 in the ring cavity is set to 0.8 mA. Both SOA3 and SOA4 are biased with a current of 20 mA to compensate for the coupling loss, and SOA5 and SOA6 are reverse biased to prevent from unexpected light reflection. We first use an optical vector network analyzer (OVNA, Luna 5400) to measure the

magnitude response, as shown in Fig. 3(a). As can be seen the free spectral response (FSR) of the MRR is around 0.203 nm (or 25.38GHz).

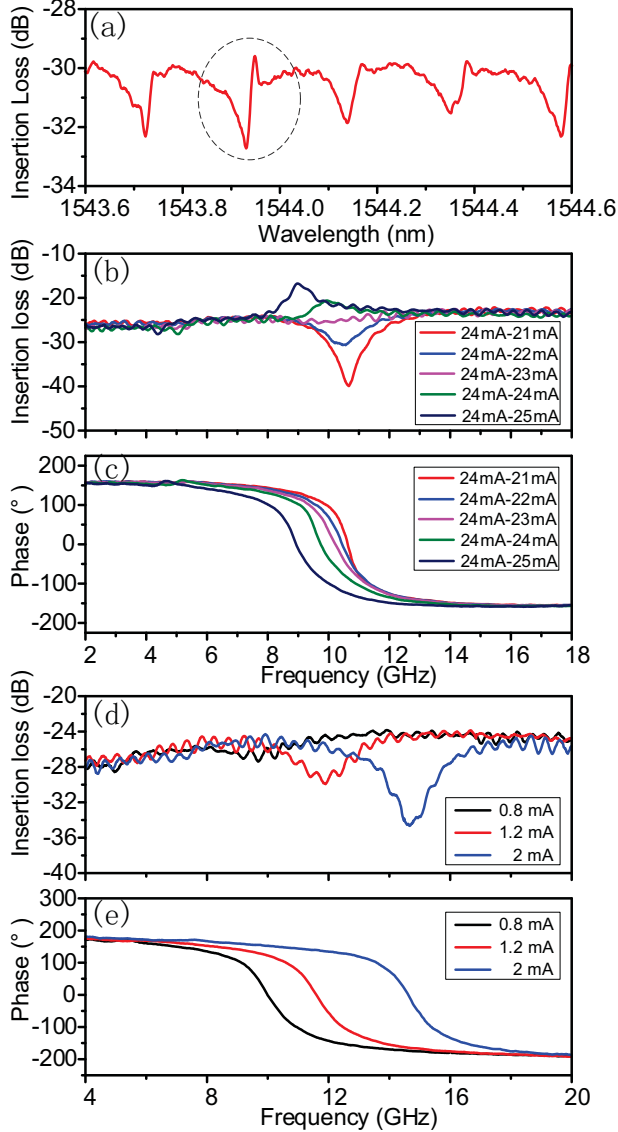


Fig. 3. The measurement results of the active MRR. (a) The magnitude response. (b) The magnitude response at 1543.92 nm and (c) the phase response. (d) The magnitude response when the resonance wavelength is tuned by PM0 and (e) the corresponding phase response.

Since the resolution of the OVNA is not high enough to measure the details of the spectral response of the MRR, we build a measurement system based on single sideband modulation to get a high resolution spectral response measurement through sweeping the sideband [17, 18]. The optical carrier is set at 1544.002 nm with the lower sideband sweeps from the optical carrier to a shorter wavelength. Here, the injection current to SOA1 is fixed at 24 mA. The extinction ratio at a resonance at 1543.92 nm is decreased when the injection current to SOA2 is increased from 20 mA to 23 mA, as shown in Fig. 3(b). When the injection current is larger than 23 mA, the gain will be greater than the loss in the ring cavity, but the lasing still does not start. Thus, the response of the MRR should be stable when the injection current applied on SOA2 is less than 23 mA. Fig. 3(c) shows the phase response when the injection current to SOA2 is increasing. As can be seen the phase shift range of about 300° is maintained almost unchanged. A slight resonance frequency

shift, as shown in Fig. 3(b) and (c), is mainly caused by the thermal effect introduced by the SOAs. Fig. 3(d) shows the resonance wavelength tuning of the MRR. As can be seen the resonance frequency is shifted from 9.7 GHz to 14.7 GHz when the injection current applied to PM0 is increased from 0.8 mA to 2 mA. During the wavelength tuning, the phase response is laterally shifted, but the phase shift range is remained almost unchanged (shown in Fig. 3(e)).

The MRR is then employed to implement an MWP phase shifter. The experimental setup is shown in Fig. 4. An optical carrier from a tunable laser source (TLS, Anritsu MG9638A) is modulated by a microwave signal generated by a vector network analyzer (VNA, Agilent E8364A) at a PM. After amplification by an erbium-doped fiber amplifiers (EDFA), the optical signal is sent to a tunable bandpass optical filter (OF) where one sideband is filtered out, to get an optical single-sideband (OSSB) signal. Then, the OSSB signal is coupled into the MRR through a polarization controller (PC2). The optical signal at the output of the MRR is detected by a PD to recover the microwave signal, which is sent to the VNA for intensity and phase analysis.

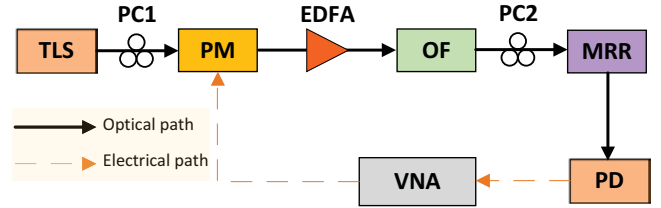


Fig. 4. Experimental setup for the proposed MWP phase shifter.

In the experiment, the wavelength of the optical carrier is set at 1543.884 nm, located at the resonance wavelength shown in Fig. 3(d) when the injection current to PM0 is 1.2 mA. The two sidebands are located at outside of the resonance, and one sideband is removed by the optical filter. To avoid the nonlinear effect in the MRR, the power of the optical carrier light is controlled less than -3 dBm before coupling into the MRR. A phase shift is introduced to the optical carrier from the phase response of the MRR, and the phase shift can be tuned by tuning the injection current to PM0. The beating between the optical carrier and the sideband will translate the phase shift in the optical carrier to the microwave signal.

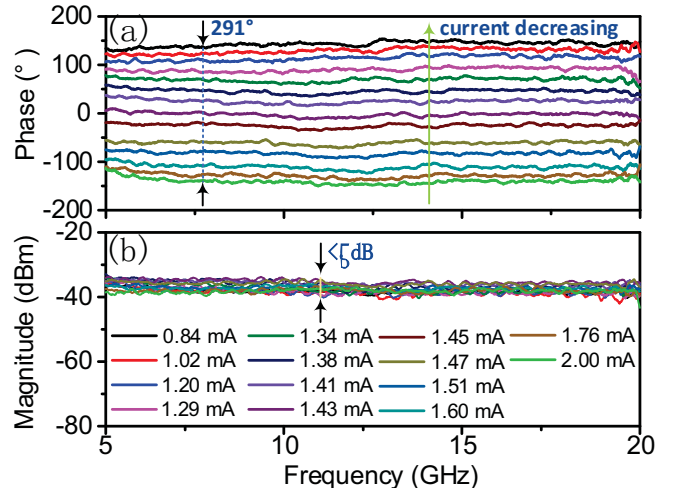


Fig. 5. Experimental results of the (a) phase response and (b) magnitude response of the phase shifter by decreasing the injection current applied on the PM in the ring cavity.

In the experiment, the injection currents to SOA3 and SOA4 are 20 mA. SOA5 and SOA6 are reverse biased with an identical voltage of -3 V. The injection current to SOA1 is set at 24 mA and the injection current to SOA2 is set at 23 mA. The injection currents applied to TC1 and TC2 are 1.5 mA and 2 mA, respectively. By tuning the injection current to PM0 from 2 mA to 0.84 mA, a phase shift from -148° to 143° with a total phase tunable range of 291° for a microwave frequency range from 5 GHz to 20 GHz is realized, as shown in Fig. 5(a). The microwave power variation is controlled small by fixing the injection currents which are applied to SOA1 and SOA2 to make the gain compensate the loss in the resonance cavity. As can be seen, in Fig. 5(b), the microwave power variation is smaller than 5 dB. This power variation can be attributed to the noise of the SOA and thermal noise in the chip. Once the chip is well temperature controlled, the microwave power variation during phase shifting can be suppressed. Moreover, since the MRR used in our experiment is an active device without packaging, the microwave power variation due to environmental changes is relatively high, which can be reduced if the device is well packaged. The bandwidth of the proposed MWP phase shifter is mainly limited by the FSR of the MRR. By reducing the length of the ring cavity, the FSR of the MRR could be increased. Thus, the bandwidth of the proposed MWP phase shifter can be broadened.

IV. CONCLUSION

We have proposed and experimentally demonstrated a continuously tunable MWP phase shifter based on the add-drop type InP/InGaAsP-based MRR. By tuning the optical gain in the MRR, the extinction ratio of the magnitude response at a resonance was decreased to nearly zero, while the large phase shift range was maintained almost unchanged. This unique feature of the MRR is preferable for the implementation of a microwave phase shifter. The proposed phase shifter was experimentally demonstrated. A continuously tunable microwave phase shift over a phase tuning range of 291° from 5 GHz to 20 GHz by tuning the injection current to the PM was implemented. The microwave power variation was controlled as low as 5 dB. The proposed MWP phase shifter is simple and can be expected to be fully integrated on a chip by incorporating the laser source and the PM in the chip. It has great potential for using on integrated system and practical microwave applications.

REFERENCES

- [1] P. Heli, F. Largesse, F. Scotti, G. Serafino, A. Capri, S. Pinna, D. Noori, C. Pori, M. Scaffidi, A. Malacarne, V. Verses, E. Lazzeri, F. Berizzi, and A. Bogoni, "A fully photonics-based coherent radar system," *Nature*, vol. 507, no. 7492, pp. 341-345, Mar. 2014.
- [2] M. H. Alsharif and R. Nordin, "Evolution towards fifth generation (5G) wireless networks: Current trends and challenges in the deployment of millimetre wave, massive MIMO, and small cells," *Telecommun. Syst.*, vol. 64, no. 4, pp. 617-637, Apr. 2017.
- [3] M. Agiwal, A. Roy, and N. Saxena, "Next Generation 5G Wireless Networks: A Comprehensive Survey," *IEEE Commun. Surveys Tuts.*, vol. 18, no. 3, pp. 1617-1655, Feb. 2016.
- [4] J. Yao, "Microwave Photonics," *J. Lightwave Technol.*, vol. 27, no. 3, pp. 314-335, Feb. 2009.
- [5] J. Capmany and D. Novak, "Microwave photonics combines two worlds," *Nature Photon.*, vol. 1, no. 6, pp. 319-330, Jun. 2007.
- [6] R. A. Minasian, E. H. W. Chan, and X. Yi, "Microwave photonic signal processing," *Opt. Express*, vol. 21, no. 19, pp. 22918-22936, Sep. 2013.
- [7] L. R. Chen, "Silicon Photonics for Microwave Photonics Applications," *J. Lightwave Technol.*, vol. 35, no. 4, pp. 824-835, Feb. 2017.
- [8] X. Yi, S. Chew, S. Song, L. Nguyen, and R. Minasian, "Integrated Microwave Photonics for Wideband Signal Processing," *Photonics*, vol. 4, no. 4, pp. 46, Nov. 2017.
- [9] W. Zhang and J. Yao, "Silicon-Based Integrated Microwave Photonics," *IEEE J. Quantum Elect.*, vol. 52, no. 1, pp. 0600412, Jun. 2016.
- [10] Q. Xu, B. Schmidt, S. Pradhan, and M. Lipson, "Micrometre-scale silicon electro-optic modulator," *Nature*, vol. 435, no. 7040, pp. 325-327, May 2005.
- [11] W. Liu, M. Li, R. S. Guzzon, E. J. Norberg, J. S. Parker, M. Lu, L. A. Coldren and J. Yao, "A fully reconfigurable photonic integrated signal processor," *Nature Photon.*, vol. 10, no. 3, pp. 190-195, Feb. 2016.
- [12] J. Capmany, D. Domenech, and P. Munoz, "Silicon graphene waveguide tunable broadband microwave photonics phase shifter," *Opt. Express*, vol. 22, no. 7, pp. 8094-8100, Apr. 2014.
- [13] M. Pu, L. Liu, W. Xue, Y. Ding, L. H. Frandsen, H. Ou, K. Yvind, and J. M. Hvam, "Widely tunable microwave phase shifter based on silicon-on-insulator dual-microring resonator," *Opt. Express*, vol. 18, no. 6, pp. 6172-6182, Mar. 2010.
- [14] X. Liu, C. Sun, B. Xiong, J. Wang, L. Wang, Y. Han, Z. Hao, H. Li, Y. Luo, J. Yan, T. Wei, Y. Zhang, and J. Wang, "Broadband tunable microwave photonic phase shifter with low RF power variation in a high-Q AlN microring," *Opt. Lett.*, vol. 41, no. 15, pp. 3599-3602, Aug. 2016.
- [15] M. Burla, D. Marpaung, L. Zhuang, C. Roeloffzen, M. R. Khan, A. Leinse, M. Hoekman, and R. Heideman, "On-chip CMOS compatible reconfigurable optical delay line with separate carrier tuning for microwave photonic signal processing," *Opt. Express*, vol. 19, no. 15, pp. 21475-21484, Aug. 2011.
- [16] D. G. Rabus, "Integrated Ring Resonators: The Compendium" *Springer Series in Optical Sciences*, no. 4, 2007.
- [17] W. Li, W. Wang, L. Wang, and N. Zhu, "Optical vector network analyzer based on single-sideband modulation and segmental measurement," *IEEE Photon. J.*, vol. 6, no. 2, pp. 1-8, Apr. 2014.
- [18] N. Ehteshami, W. Zhang, and J. Yao, "Optically tunable full 360° microwave photonic phase shifter using three cascaded silicon-on-insulator microring resonators," *Opt. Commun.*, vol. 373, pp. 53-58, Aug. 2016.

II. Widely-Tunable VCSELs



Resonant-antiresonant coupled cavity VCSELs

KEVIN T. COOK,¹ PENGFEI QIAO,¹ JIPENG QI,¹ LARRY A. COLDREN,² AND CONNIE J. CHANG-HASNAIN^{1,*}

¹Department of Electrical Engineering and Computer Sciences and Tsinghua-Berkeley Shenzhen Institute, University of California at Berkeley, Berkeley, CA 94720, USA

²Departments of Electrical and Computer Engineering and Materials, University of California at Santa Barbara, Santa Barbara, CA 93106, USA

*cch@berkeley.edu

Abstract: The wavelength tuning range of a tunable vertical-cavity surface-emitting laser (VCSEL) is strongly influenced by the design of the interface between the semiconductor cavity and the air cavity. A simplified model is used to investigate the origin of the dramatic differences in free spectral range (FSR) and tuning slope observed in semiconductor cavity dominant, extended cavity, and air cavity dominant VCSELs. The differences arise from the positioning of the resonant and antiresonant wavelengths of the semiconductor cavity with respect to the center wavelength. The air cavity dominant design is realized by designing an antiresonant semiconductor cavity, resulting in a larger tuning slope near the center of the tuning range and a wider FSR toward the edges of the tuning range. The findings from the simplified model are confirmed with the simulation of a full VCSEL structure. Using an air cavity dominant design, an electrically pumped laser with a tuning range of 68.38 nm centered at 1056.7 nm at a 550 kHz sweep rate is demonstrated with continuous wave emission at room temperature. This epitaxial design rule can be used to increase the tuning range of tunable VCSELs, making them more applicable in swept-source optical coherence tomography and frequency-modulated continuous-wave LIDAR systems.

© 2019 Optical Society of America under the terms of the [OSA Open Access Publishing Agreement](#)

1. Introduction

Wavelength-swept lasers are important components in modern optical communications, light detection and ranging (LIDAR), optical coherence tomography (OCT), and high-resolution laser spectroscopy. The most important performance criteria are wavelength tuning ratio ($\Delta\lambda/\lambda_C$) and sweep speed. Vertical-cavity surface-emitting lasers (VCSELs) with tuning capability [1] have exhibited many desirable attributes including wafer-scale fabrication and testing, continuous and wide tuning, small footprint, and low power consumption. With a very short cavity (2-10 μm), the VCSEL's wavelength can be tuned by varying the optical thickness of some of the DBR layers or the optical cavity. This may be accomplished by varying the refractive index of some of the layers [2–4] or their physical thicknesses. The former approach has yet to experimentally result in a wide sweep range. Alternatively, using a microelectromechanical system (MEMS) to physically change the optical cavity length, a wide, continuous tuning range has been demonstrated [5]. Since the first MEMS-tunable VCSEL reported in 1995, many advances have been reported for center wavelengths (λ_C) of 850 nm, 980 nm, 1060 nm, 1310 nm, and 1550 nm [6–13]. Conventional MEMS-tunable VCSELs are designed with a high optical intensity concentrated in the semiconductor portion [5–7]. This configuration is referred to as semiconductor cavity dominant (SCD) design. The tuning ratio of a SCD design is limited to $\sim 3.5\%$ by the relatively small free spectral range (FSR).

To increase the tuning range, researchers have designed VCSELs with a $\lambda_C/4$ -thick anti-reflection (AR) layer with $n_{AR} = \sqrt{n_S}$ where n_S is the index of the topmost semiconductor

layer. This configuration was referred to as the extended cavity (EC) design in [8]. In this case, the semiconductor and air cavities are perfectly matched. They resonate as one cavity, as if the semiconductor cavity “extends” into the air region. Previously, a very large static tuning range of 102 nm centered at 1550 nm ($\Delta\lambda/\lambda_C = 6.6\%$) was reported for an electrically-pumped EC VCSEL using electro-thermal tuning [9]. Limited by the thermal time constant, the tuning speed is shown to be relatively slow at 215 Hz with a smaller dynamic sweep range of 87 nm ($\Delta\lambda/\lambda_C = 5.6\%$). The EC design has also been implemented at a center wavelength of 1050 nm with a swept tuning range of 63.8 nm ($\Delta\lambda/\lambda_C = 6.1\%$) and a faster sweep rate of 240 kHz [10]. Both devices utilize dielectric distributed Bragg reflectors (DBR) with a high index contrast to minimize the effective length of the cavity, increasing the FSR at the cost of increased fabrication complexity due to additional deposition steps or multiple oxidation layers.

Recently, a third configuration called the air cavity dominant (ACD) design was reported, which forces the optical field to be confined more significantly in the air cavity at the center wavelength [11]. This design led to a record tuning ratio of 6.9% for an electrically-pumped VCSEL, while allowing more flexible choices of materials and thicknesses in the semiconductor-air coupling (SAC) region and the bottom DBR.

In this study, we reveal the origin of the increased tuning range of the ACD design and the impact of the design on threshold material gain. The swept operation of the device is demonstrated, exhibiting a swept tuning ratio of 6.5% at a sweep rate of 550 kHz. The high sweep rate is attributed to the lightweight high-contrast grating (HCG) used as the tunable mirror [14].

2. Underlying physics of tunable VCSELs

Figure 1 shows the schematic and the scanning electron microscopy (SEM) image of our 1060-nm ACD HCG tunable VCSEL. The device consists of a semiconductor portion, a top HCG mirror, and an air gap in between forming an air cavity. The semiconductor portion (starting from the top) includes a semiconductor-air coupling (SAC) region, two pairs of p-DBRs ($\text{Al}_{0.12}\text{Ga}_{0.88}\text{As}$ high-index layer first, followed by $\text{Al}_{0.9}\text{Ga}_{0.1}\text{As}$ low-index layer, $\text{Al}_{0.12}\text{Ga}_{0.88}\text{As}$ high-index layer, and $\text{Al}_{0.98}\text{Ga}_{0.02}\text{As}$ layer for oxidation), a $1\lambda_C$ cavity with five quantum wells in the center, followed by 38.5 pairs of n-DBRs, all grown on an n-doped GaAs substrate. One can identify two longitudinally coupled cavities: one centered at the active cavity with quantum wells and a second centered at the air gap between the HCG and the semiconductor. As described in [11], the SAC region dictates the difference between the three designs: SCD, EC and ACD.

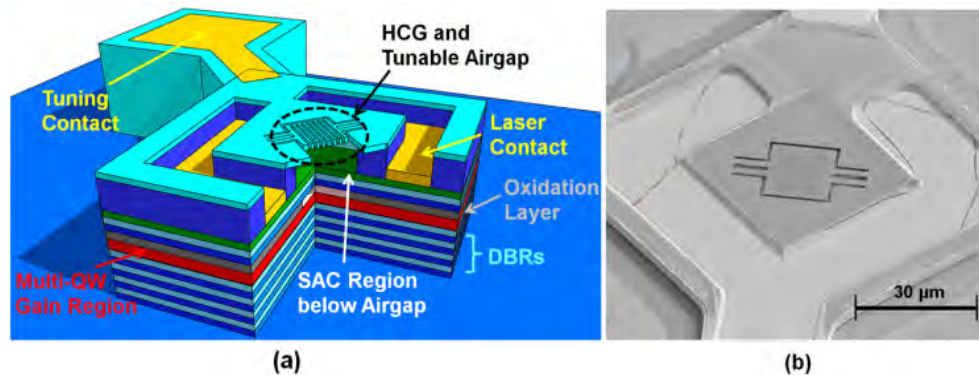


Fig. 1. (a) Schematic view of a MEMS-HCG tunable VCSEL with engineered semiconductor-air coupling (SAC) region. (b) Scanning electron microscope view of a fabricated 1060-nm MEMS-HCG tunable VCSEL.

To explore the underlying physics of the two cavities, we simplified the entire epitaxy stack to a $4\lambda_C$ semiconductor cavity with index n_S , a $\lambda_C/4$ SAC layer, and an air region of variable length (index 1), shown in Fig. 2(a). The semiconductor cavity was chosen to be $4\lambda_C$ to have a similar FSR to a realistic design. The structure is bounded on both sides by ideal reflectors which have Fresnel coefficients $r_1 = r_3 = 0.999 + 0i$ for all wavelengths. This eliminates the nonlinearity and discontinuities in the phase of the HCG and DBR reflectors, which allows the resonance lines in Fig. 2 to extend beyond the bandwidth of the real reflectors. When the mirrors are replaced with practical structures, the wavelength range will be sampled by the bandwidth of the DBR and the phase spectra of the reflectors will distort the tuning curve near the edges of the tuning range.

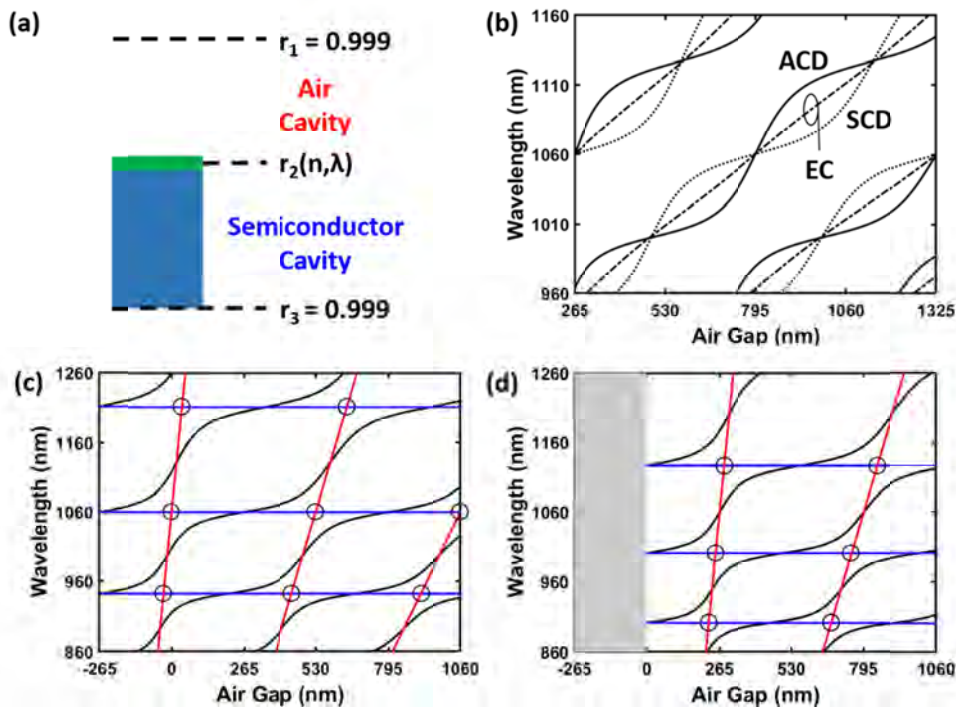


Fig. 2. Simplified coupled-cavity transfer-matrix analysis. (a) Illustration of simplified two coupled cavities with a semiconductor-air coupling (SAC) layer in-between. The $4\lambda_C$ semiconductor cavity with index n_S is shown in blue, the SAC layer with index n_{SAC} is shown in green, and the air cavity has an index of 1. The reflectors are indicated by dashed lines. (b) Comparison between SCD, EC, and ACD tuning characteristics with $n_{SAC} = 1$, n_{AR} , n_S respectively. The ACD design has the widest FSR when measured around the center wavelength of 1060 nm. (c) SCD and (d) ACD tuning curves plotted in black against semiconductor cavity modes in blue and air cavity modes in red. The circles indicate where the two families of lines cross, which results in anti-crossing in the (black) resonance lines of the full structures.

We consider three refractive index values for the $\lambda_C/4$ SAC layer, $n_{SAC} = 1$, n_{AR} , or n_S , representing SCD, EC, and ACD cases, respectively. The resonances of the simplified coupled-cavity structure for the three cases are calculated using the transfer matrix method by finding the wavelengths with zero round-trip phase for each air cavity length and are plotted as a function of air cavity length, as shown in Fig. 2(b), for all three cases. The EC case has Fabry-Perot (FP) wavelength linearly dependent on the air cavity length since the entire structure is one cavity. However, the SCD and ACD have distinctly different curvatures. This behavior is the same as shown in Fig. 13 of [11] with a full VCSEL design.

To understand the curvatures of the SCD and ACD resonance lines, we examine the two cavities: the air cavity defined by r_1 and r_2 , and the semiconductor cavity defined by r_2 and r_3 . The FP resonances for the semiconductor cavity, computed by removing r_1 from the transfer matrix simulation described above and plotted in blue in Figs. 2(c) and 2(d), are horizontal lines since they do not depend on the air cavity length. The FP resonances for the air cavity between r_1 and r_2 , computed by removing r_3 from the simulation and plotted in red in Figs. 2(c) and 2(d), are linearly proportional to the air cavity length. Coupling between the semiconductor cavity and air cavity occurs when the two families of lines intersect each other, marked with circles on Figs. 2(c) and 2(d). The FP resonances of the full structure follows these two families of lines but avoid the crossings as shown by the black curved traces.

Figure 2(c) shows the case where $n_{SAC} = 1$. The semiconductor cavity is in resonance at $\lambda_C = 1060$ nm and thus a blue line is shown at the center wavelength 1060 nm. At an air gap of $-\lambda_C/4$, r_1 directly touches the semiconductor cavity. The full structure resonance lines are coincident with the semiconductor cavity resonance lines. As the air gap increases, an avoided crossing causes the full structure resonance to follow the air cavity resonance. Eventually, the full structure resonance avoids a second crossing to switch back to following the semiconductor resonance line. Since there is a semiconductor resonance at λ_C , the full structure resonance shows a low tuning slope at the center wavelength. This is the characteristic feature of an SCD design.

Figure 2(d) shows the case where $n_{SAC} = n_S$. Due to the $\lambda_C/4$ SAC refractive index, the FP wavelengths for the semiconductor cavity are shifted from those in the SCD case (Fig. 2(c)). In this ACD case, the semiconductor cavity is in *antiresonance* at λ_C , with the nearest FP modes located instead at 1130.7 and 997.6 nm. Again, the full structure resonance lines begin coincident with the semiconductor lines at an air cavity length of 0. The VCSEL resonance curves avoid the crossings between semiconductor and air resonances as air cavity length increases. Since the semiconductor cavity is in antiresonance at λ_C , the full structure resonance follows the air cavity resonance, resulting in a large tuning slope. This represents the ACD case. A stronger coupling between the semiconductor and air cavities in either an ACD or SCD design pushes the black lines apart, approaching the tuning characteristic for the EC case, in which the cavities are perfectly coupled.

The mathematical origin of the semiconductor resonances lies in the phase of r_2 . If $n_{SAC} < n_{AR}$, then the interface between the semiconductor cavity and the SAC layer dominates r_2 . The reflection phase into the semiconductor cavity, $\angle r_2(\lambda_C)$, is zero, and the semiconductor cavity is in resonance at λ_C . For the special case in which $n_{SAC} \cong n_{AR}$, the magnitude of r_2 is insignificant and the VCSEL cavity resonates as a unit. If $n_{SAC} > n_{AR}$, then the interface between the air cavity and the $\lambda_C/4$ SAC layer dominates r_2 . The reflection phase $\angle r_2(\lambda_C) = \pi$, the semiconductor cavity is in antiresonance at λ_C , and the design is ACD. Note this description is very general and applies to more complex designs, such as that depicted in Fig. 1, which has two pairs of p-DBR between the $1\lambda_C$ cavity and the SAC, and the SAC consists of a window ($\lambda_C/2$) layer between the $\lambda_C/4$ n_{SAC} layer and air cavity.

For a typical tunable MEMS-VCSEL design, the air cavity length is chosen to be large enough to allow large tuning range with a maximum MEMS movement approximately 1/3 of the air gap. The FSR is thus the limiting factor in tunable VCSEL designs. As noted above, FSR is not constant with changing air cavity length. The range-limiting FSR is the shortest wavelength difference between the modes directly above and directly below the center wavelength, as these are the modes which are able to achieve threshold. In both ACD and SCD designs, the highest FSR is located near the intersections of the VCSEL cavity modes and the semiconductor cavity modes. Since the semiconductor cavity modes are off-center in an ACD VCSEL, the FSR is highest when the VCSEL resonance is far from the center of its tuning range. In contrast, the FSR of an SCD VCSEL is decreased as the VCSEL resonance moves away from the tuning center. The difference in FSR is illustrated in Fig. 2(b), which

shows the VCSEL cavity modes for SCD, EC, and ACD designs. With this model, it is clear that to obtain a large tuning ratio, it is important to design an antiresonant semiconductor cavity with minimum length and reduce the coupling between the two cavities. In other words, it is best to let the air cavity dominate.

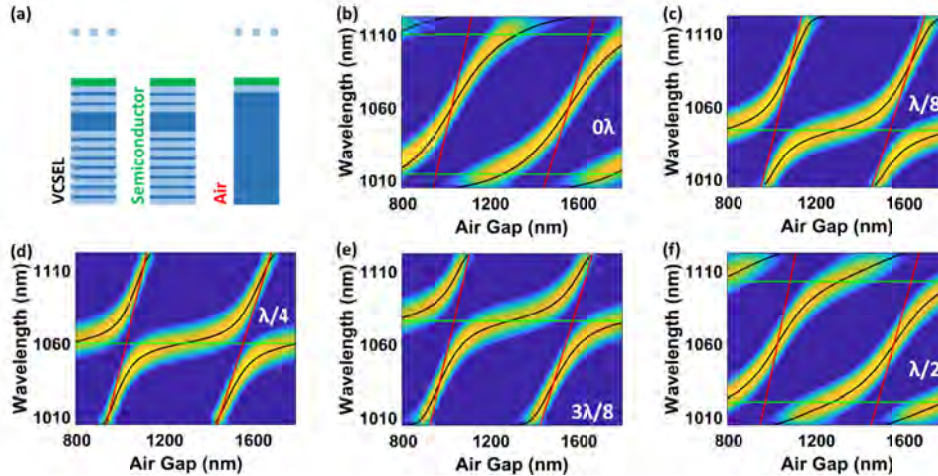


Fig. 3. FP Resonance as a function of air cavity thickness for a realistic VCSEL cavity using transfer-matrix and FDTD analysis. (a) Schematic of VCSEL structure, semiconductor cavity structure, and air cavity structure used to compute Fabry-Perot modes. The SAC region contains a high-index $\lambda_c/2$ “window” layer on top of a low-index $\lambda_c/4$ layer with n_{low} , both indices $>n_{AR}$. (b)–(f) Transfer matrix simulations for VCSEL modes (black), semiconductor cavity modes (green), and air cavity modes (red), inscribed on a resonance colormap from FDTD simulations of the full VCSEL structure. The thickness of the “window” layer is varied from 0 to $\lambda_c/2$, illustrating the shift from ACD at 0 to SCD at $\lambda_c/4$ and back to ACD at $\lambda_c/2$.

3. FDTD simulation of full structure

The above simplified model is next verified by FDTD simulation of a realistic VCSEL structure without active layers. Figure 3(a) shows the structure consisting of regions of $n_{high} = 3.483$ and $n_{low} = 2.988$, both $>n_{AR}$. From top to bottom, there is an HCG, a tunable air cavity, a SAC region, a 2-pair DBR, a $1\lambda_c$ high-index cavity, a 38.5-pair DBR, and a high-index substrate of infinite thickness. The SAC region contains a high-index $\lambda_c/2$ window layer on top of a low-index $\lambda_c/4$ layer with n_{low} . In this example, since there are limited choices of III-V epitaxy materials (refractive indices) for monolithic growth, we illustrate the coupling effect by changing the SAC window layer thickness instead by adding or removing a $\lambda_c/4$ layer.

In this structure, r_1 is the reflectivity of the HCG (computed using rigorous coupled-wave analysis [14]), r_2 is the reflectivity of the SAC region, and r_3 is the reflectivity of the 38.5-pair DBR terminating in the substrate. The FDTD simulation in Figs. 3(b)–3(e) shows resonance lines of the entire structure as functions of air cavity length when the window layer is varied from 0 to $\lambda_c/2$. The color code indicates the strength of the cavity resonance (yellow is high Q and blue is low). The resonance for the air cavity, semiconductor cavity and the entire structure using transfer-matrix simulations are also plotted in the same plots for comparison. Excellent agreement is obtained between the two approaches.

Since the dominant interface contributing to r_2 is the interface between the window layer and the air gap, the semiconductor cavity is much more sensitive to changes in window layer thickness than the air cavity. As the thickness of the window layer increases, so does the wavelength of each semiconductor resonance. Meanwhile, the position and slope of the air cavity resonances remains almost constant. Since the tuning behavior is dominated by the semiconductor cavity resonance, any increase in the overall thickness of the semiconductor

cavity corresponds to a shift in the tuning characteristic. When the thickness of the window layer is 0, the SAC simply consists of a low-index $\lambda_c/4$ layer (but the low index is still greater than n_{AR}). Hence, the semiconductor cavity is antiresonant with two semiconductor resonances at ~ 1010 and 1110 nm, as shown in Fig. 3(b). This is the ACD case. When the window has a thickness of $\lambda_c/4$, the semiconductor cavity is in resonance, resulting in an SCD tuning characteristic as shown in Fig. 3(d). With the window layer increased to $\lambda_c/2$, the device is again ACD, as shown in Fig. 3(f).

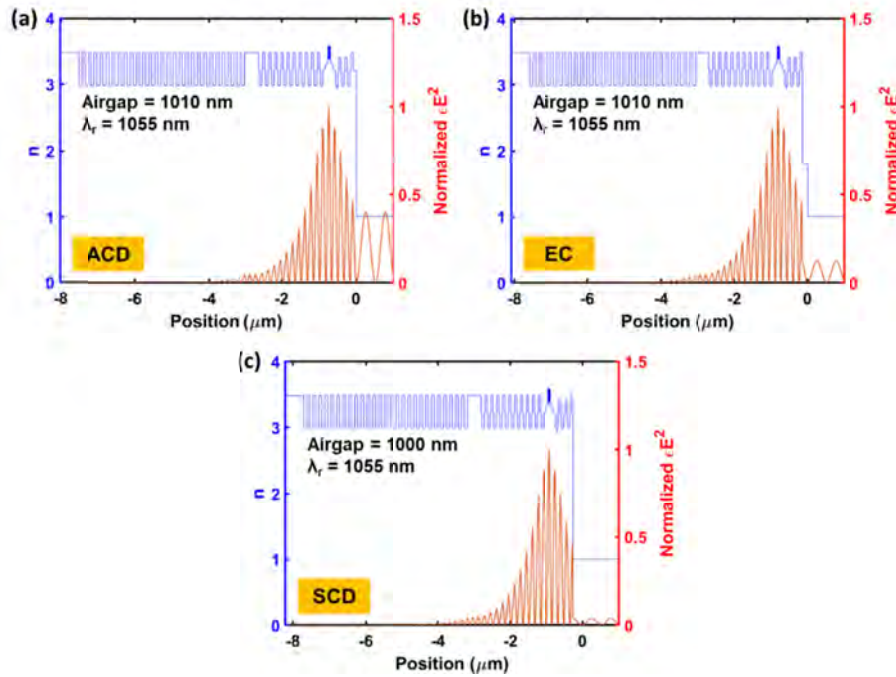


Fig. 4. Longitudinal electric energy density $\epsilon(z)|E(z)|^2$ profiles (red) calculated using the transfer-matrix method at tuning center where $\lambda_r = 1060$ nm for (a) ACD, (b) EC and (c) SCD. The refractive index (blue) for each layer is also plotted for each case to show the simulated structure.

4. Optical confinement

The optical confinement factor is an important parameter to examine since it determines the threshold current density. The real VCSEL structure, described in section one and shown in Fig. 1, is used for this study. The top $\lambda_c/4$ portion of semiconductor is InGaP in the real device (ACD) but is changed to Al_2O_3 in the EC design and air in the SCD device for comparison here. The longitudinal electric energy density $\epsilon(z)|E(z)|^2$ profiles at tuning center wavelength for ACD, EC, and SCD VCSELs are shown in Figs. 4(a), 4(b), and 4(c), respectively. At the tuning center, all three cases show the largest energy density inside the MQW region, which indicates a good field alignment. We indeed observe a relatively large energy distribution in the air cavity for ACD, in contrast to both EC and SCD. This confirms a strong coupling with the air cavity at the tuning center for the ACD case. Since ACD has more energy confined in the air sub-cavity, it should follow that the energy confinement factor for ACD is lower than EC and SCD.

To understand how the tuning impacts the laser threshold, we now calculate the effective cavity length observed from the semiconductor

$$L_{eff}(\lambda_r) = -\frac{\lambda_r^2}{4\pi n_g} \frac{\partial}{\partial \lambda} [\phi_{top}(\lambda) + \phi_{bottom}(\lambda)]_{\lambda=\lambda_r} \quad (1)$$

where $\phi_{top}(\lambda)$ and $\phi_{bottom}(\lambda)$ are reflective phases for the top and bottom mirrors seen by the semiconductor cavity [15]. In this approach, we consider the layers beneath the central quantum well as our bottom effective mirror and the layers above as the top effective mirror. Note that the effective length of the ACD design is the largest for all three designs at the tuning center.

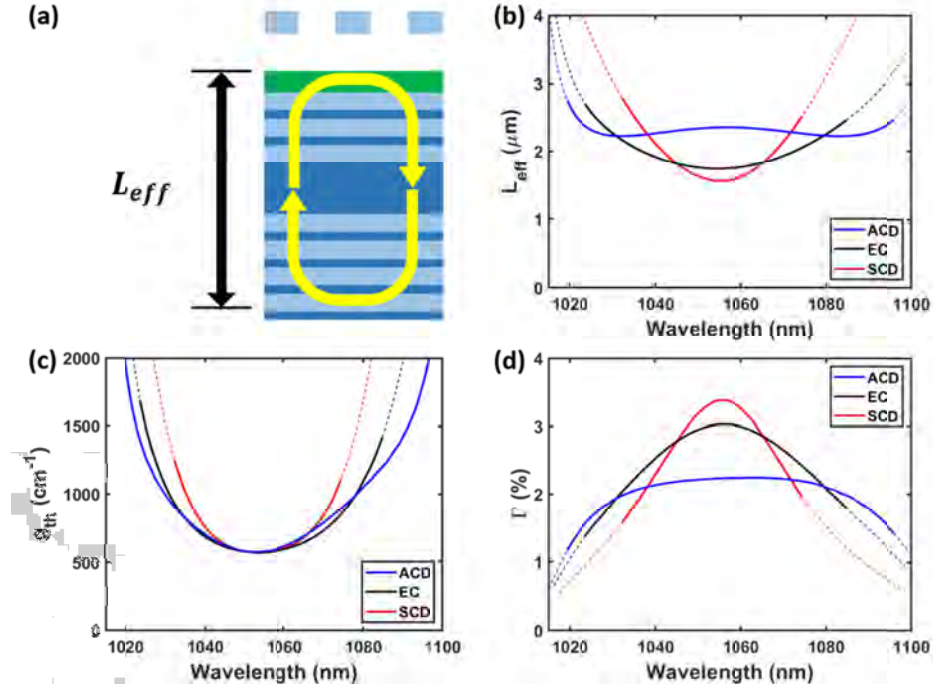


Fig. 5. Effective length is observed from the semiconductor cavity. (b) Total effective length L_{eff} as a function of resonance wavelength for SCD (red), EC (black), and ACD (blue) designs. (c) Threshold material gain g_{th} with uniform material loss $\alpha_i = 20 \text{ cm}^{-1}$ added to all semiconductor layers. (d) Confinement factor calculated with $\Gamma = \alpha/g_{th}$.

However, the effective length for ACD stays relatively constant across the entire tuning range, whereas that of the SCD sharply increases as wavelength deviates from the center wavelength. Indeed, at the edges of the tuning range, the effective lengths of the SCD and EC devices become larger than that of the ACD device.

The threshold material gain is rigorously calculated as described in [11] for all three configurations and plotted in Fig. 5(c). Gain is added to the complex refractive index of the quantum well layers, and 20 cm^{-1} of loss is added to every other semiconductor layer. The transfer-matrix method is used to determine the round-trip gain of the cavity at the resonant wavelength. At threshold, the round-trip gain is equal to one. Since the internal loss is included in the calculation of the mirror reflectivity, the total loss in the cavity is given by

$$\Gamma g_{th} = \alpha = \frac{1}{2L_{eff}} \ln \left(\frac{1}{R_1 R_2} \right) \quad (2)$$

Rearranging Eq. (2) allows the calculation of the VCSEL's longitudinal confinement factor using the simulated threshold gain, effective length, and mirror reflectivities. The confinement factor is plotted as a function of resonant wavelength in Fig. 5(d). The ACD device has the lowest confinement factor of all three cases due to the large portion of electric energy confined in the air. Despite the significantly lower confinement factor of the ACD device, the threshold material gain at the tuning center is only increased by 1% because mirror loss and internal loss are both reduced at the center of the tuning range. Mirror loss is reduced in the ACD device by the higher L_{eff} , while internal loss is reduced by confining more energy in the lossless air gap.

The effective length and confinement factor calculations provide further insight into the threshold gain and FSR of the three designs. The FSR, which is inversely proportional to L_{eff} , is an important parameter at the tuning edge, where neighboring F-P modes may compete for the finite gain provided by the quantum wells. As shown in Fig. 5(b), the ACD design has the smallest effective length and thus the largest FSR at the tuning edge, confirming the trend noted in Fig. 2. The reduced effective length at the tuning edge in the ACD design also results in a higher confinement factor and lower threshold gain. As a result, using this novel ACD design, the threshold gain is not compromised significantly while the tuning range is largely extended.

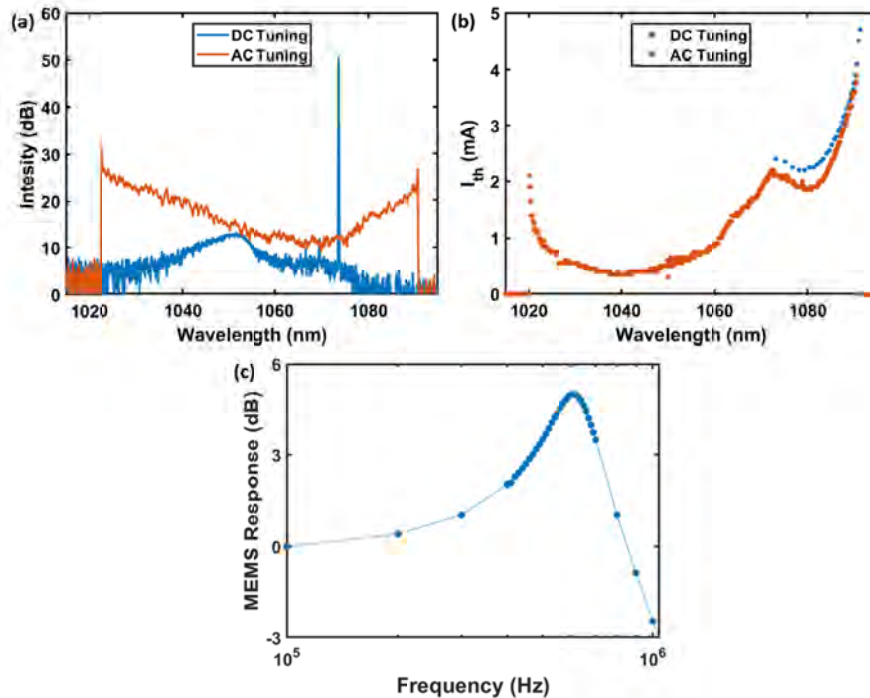


Fig. 6. (a) Measured swept VCSEL spectra for an ACD tunable VCSEL at 4.5 mA current injection under a constant DC bias (blue) and with an additional 550 kHz AC (red) tuning voltage. The swept spectrum covers a range of 68.38 nm, measured at -20 dB from the tuning edge peaks. (b) Threshold current measured with two different techniques. The curve in blue is measured by applying a series of DC tuning biases and measuring the threshold and wavelength at $1.1I_{th}$. The curve in red is measured by applying a DC tuning bias and sweeping the position of the HCG by applying a resonant AC signal, then measuring the emission spectrum at a series of laser drive currents. (c) The MEMS frequency response shows a resonance at 610 kHz and a -3 -dB cutoff at 1.05 MHz.

5. Experimental results

The device shown in Fig. 1 is fabricated using process described in [11]. The GaAs sacrificial layer is removed by selective wet etching to form the 1.32 μm air gap. The SAC region of the actual device uses a design resembling the case shown in Fig. 3(f), with a $\lambda_c/2$ window layer composed of an InGaP etch stop and a GaAs contact layer on top of a $\lambda_c/4$ low-index layer.

Previously, with a combination of thermal, current and electrostatic tuning, single-mode continuous lasing across a 73-nm range was demonstrated [11]. With an optimized MEMS design, we obtain a continuous sweep by applying a DC tuning voltage of 31.5 V plus an AC tuning voltage of 10.0 V_{pp} at the mechanical resonance frequency of 550 kHz, as shown in Fig. 6(a). Resonant excitation of the mechanical structure displaces the mirror further than the equivalent DC voltage, eliminating the need for a tuning voltage high enough to break down the semiconductor junction [16]. The full dynamic tuning range is 68.38 nm, spanning from 1022.46 nm to 1090.84 nm, which is a direct proof of the extended FSR by our ACD design and is close to the calculated tuning range of 76 nm. If the AC voltage is increased to displace the MEMS further, the next Fabry-Perot mode will begin to lase over the same range of wavelengths. This shows that the tuning range is FSR limited and not threshold limited.

The threshold current for each wavelength is determined using the swept spectrum. The DC tuning bias, AC amplitude, and AC frequency are set such that the movement of the mirror traces one period of the tuning curve. A series of DC currents, ranging from 0.1 mA to 4 mA in steps of 0.05 mA, is applied through the laser diode. For each DC current, the emission spectrum is measured. The threshold at each wavelength is then determined by numerically differentiating the spectral intensity with respect to laser diode current and locating the abrupt step corresponding to the threshold. The results of this measurement are shown in Fig. 6(b). For comparison, the threshold current is also measured at a series of DC tuning biases.

The shape of the measured threshold current plotted versus wavelength in Fig. 6(b) deviates from the shape of the simulated threshold material gain curve in Fig. 5(c) in several aspects. First, the minimum threshold is blue-shifted to 1040 nm due to differences in HCG dimensions caused by variation in the lithography and etch processes. The second deviation is the peak at 1075 nm found in both the AC and DC measurements. This peak corresponds to a transition between two transverse modes. Transverse mode suppression is achieved in non-tunable oxide VCSELs by placing an oxide aperture near a longitudinal intensity node of the desired Fabry-Perot mode. In a tunable VCSEL, the position of the oxide layer with respect to the mode changes with wavelength, which can cause different transverse modes to dominate at different wavelengths. In the future, different transverse control mechanisms such as multiple oxide apertures, ion implantation, or buried heterostructure can be used to eliminate higher order transverse modes during tuning. Chirped QWs could also be used to reduce wavelength dependence in threshold current.

6. Conclusion

In summary, we investigate the mechanism behind the ACD configuration's large tuning range improvement over SCD and EC tunable VCSELs, finding that an antiresonance in the semiconductor cavity at the center wavelength is the cause for the high tuning slope and wide FSR. Our measurements of ACD devices confirm our theory of tuning ratio enhancement, demonstrating electrically pumped VCSELs with a high tuning ratio of 6.5% with resonant MEMS tuning at 550 kHz.

References

1. C. J. Chang-Hasnain, "Tunable VCSEL," *IEEE J. Sel. Top. Quantum Electron.* **6**(6), 978–987 (2000).
2. C. J. Chang-Hasnain, J. P. Harbison, C. E. Zah, L. T. Florez, and N. C. Andreadakis, "Continuous wavelength tuning of two-electrode vertical cavity surface emitting lasers," *Electron. Lett.* **27**(11), 1002–1003 (1991).

3. P. R. Berger, N. K. Dutta, K. D. Choquette, G. Hasnain, and N. Chand, "Monolithic Peltier-cooled vertical-cavity surface-emitting lasers," *Appl. Phys. Lett.* **59**(1), 117–119 (1991).
4. L. Frasunkiewicz, T. Czystanowski, H. Thienpont, and K. Panajotov, "Electrically tunable VCSEL with intracavity liquid crystal: Design, optimization, and analysis of polarization- and mode-stability," *Opt. Commun.* **427**, 271–277 (2018).
5. M. S. Wu, E. C. Vail, G. S. Li, W. Yuen, and C. J. Chang-Hasnain, "Tunable micromachined vertical cavity surface emitting laser," *Electron. Lett.* **31**(19), 1671–1672 (1995).
6. M. C. Y. Huang, Y. Zhou, and C. J. Chang-Hasnain, "A nanoelectromechanical tunable laser," *Nat. Photonics* **2**(3), 180–184 (2008).
7. Y. Rao, W. Yang, C. Chase, M. C. Y. Huang, D. P. Worland, S. Khaleghi, M. R. Chitgarha, M. Zivadi, A. E. Willner, and C. J. Chang-Hasnain, "Long-wavelength VCSEL using high contrast grating," *IEEE J. Sel. Top. Quantum Electron.* **19**(4), 1701311 (2013).
8. F. Sugihwo, M. C. Larson, and J. S. Harris, Jr., "Micromachined widely tunable vertical cavity laser diodes," *J. Microelectromech. Syst.* **7**(1), 48–55 (1998).
9. C. Gierl, T. Gründl, K. Zogal, H. A. Davani, C. Grasse, G. Böhm, F. Küppers, P. Meissner, and M.-C. Amann, "Surface micromachined MEMS-tunable VCSELs with wide and fast wavelength tuning," *Electron. Lett.* **47**(22), 1243–1244 (2011).
10. D. D. John, C. B. Burgner, B. Potsaid, M. E. Robertson, B. K. Lee, W. J. Choi, A. E. Cable, J. G. Fujimoto, and V. Jayaraman, "Wideband electrically pumped 1050-nm MEMS-tunable VCSEL for ophthalmic imaging," *J. Lightwave Technol.* **33**(16), 3461–3468 (2015).
11. P. Qiao, K. T. Cook, K. Li, and C. Chang-Hasnain, "Wavelength-Swept VCSELs," *IEEE J. Sel. Top. Quantum Electron.* **23**(6), 1700516 (2017).
12. E. Haglund, J. S. Gustavsson, J. Bengtsson, Å. Haglund, A. Larsson, D. Fattal, W. Sorin, and M. Tan, "Demonstration of post-growth wavelength setting of VCSELs using high-contrast gratings," *Opt. Express* **24**(3), 1999–2005 (2016).
13. I. S. Chung, V. Iakovlev, A. Sirbu, A. Mereuta, A. Caliman, E. Kapon, and J. Mork, "Broadband MEMS-tunable high-index-contrast subwavelength grating long-wavelength VCSEL," *IEEE J. Quantum Electron.* **46**(9), 1245–1253 (2010).
14. P. Qiao, W. Yang, and C. J. Chang-Hasnain, "Recent advances in high-contrast metastructures, metasurfaces, and photonic crystals," *Adv. Opt. Photonics* **10**(1), 180–245 (2018).
15. L. A. Coldren, S. W. Corzine, and M. L. Mašanović, *Diode Lasers and Photonic Integrated Circuits* (John Wiley & Sons, 2012).
16. T. Ansbaek, I. S. Chung, E. S. Semenova, O. Hansen, and K. Yvind, "Resonant MEMS tunable VCSEL," *IEEE J. Sel. Top. Quantum Electron.* **19**(4), 1702306 (2013).

In the experiment, the injection currents to SOA3 and SOA4 are 20 mA. SOA5 and SOA6 are reverse biased with an identical voltage of -3 V. The injection current to SOA1 is set at 24 mA and the injection current to SOA2 is set at 23 mA. The injection currents applied to TC1 and TC2 are 1.5 mA and 2 mA, respectively. By tuning the injection current to PM0 from 2 mA to 0.84 mA, a phase shift from -148° to 143° with a total phase tunable range of 291° for a microwave frequency range from 5 GHz to 20 GHz is realized, as shown in Fig. 5(a). The microwave power variation is controlled small by fixing the injection currents which are applied to SOA1 and SOA2 to make the gain compensate the loss in the resonance cavity. As can be seen, in Fig. 5(b), the microwave power variation is smaller than 5 dB. This power variation can be attributed to the noise of the SOA and thermal noise in the chip. Once the chip is well temperature controlled, the microwave power variation during phase shifting can be suppressed. Moreover, since the MRR used in our experiment is an active device without packaging, the microwave power variation due to environmental changes is relatively high, which can be reduced if the device is well packaged. The bandwidth of the proposed MWP phase shifter is mainly limited by the FSR of the MRR. By reducing the length of the ring cavity, the FSR of the MRR could be increased. Thus, the bandwidth of the proposed MWP phase shifter can be broadened.

IV. CONCLUSION

We have proposed and experimentally demonstrated a continuously tunable MWP phase shifter based on the add-drop type InP/InGaAsP-based MRR. By tuning the optical gain in the MRR, the extinction ratio of the magnitude response at a resonance was decreased to nearly zero, while the large phase shift range was maintained almost unchanged. This unique feature of the MRR is preferable for the implementation of a microwave phase shifter. The proposed phase shifter was experimentally demonstrated. A continuously tunable microwave phase shift over a phase tuning range of 291° from 5 GHz to 20 GHz by tuning the injection current to the PM was implemented. The microwave power variation was controlled as low as 5 dB. The proposed MWP phase shifter is simple and can be expected to be fully integrated on a chip by incorporating the laser source and the PM in the chip. It has great potential for using on integrated system and practical microwave applications.

REFERENCES

- [1] P. Heli, F. Largesse, F. Scotti, G. Serafino, A. Capri, S. Pinna, D. Noori, C. Pori, M. Scaffidi, A. Malacarne, V. Verses, E. Lazzeri, F. Berizzi, and A. Bogoni, "A fully photonics-based coherent radar system," *Nature*, vol. 507, no. 7492, pp. 341-345, Mar. 2014.
- [2] M. H. Alsharif and R. Nordin, "Evolution towards fifth generation (5G) wireless networks: Current trends and challenges in the deployment of millimetre wave, massive MIMO, and small cells," *Telecommun. Syst.*, vol. 64, no. 4, pp. 617-637, Apr. 2017.
- [3] M. Agiwal, A. Roy, and N. Saxena, "Next Generation 5G Wireless Networks: A Comprehensive Survey," *IEEE Commun. Surveys Tuts.*, vol. 18, no. 3, pp. 1617-1655, Feb. 2016.
- [4] J. Yao, "Microwave Photonics," *J. Lightwave Technol.*, vol. 27, no. 3, pp. 314-335, Feb. 2009.
- [5] J. Capmany and D. Novak, "Microwave photonics combines two worlds," *Nature Photon.*, vol. 1, no. 6, pp. 319-330, Jun. 2007.
- [6] R. A. Minasian, E. H. W. Chan, and X. Yi, "Microwave photonic signal processing," *Opt. Express*, vol. 21, no. 19, pp. 22918-22936, Sep. 2013.
- [7] L. R. Chen, "Silicon Photonics for Microwave Photonics Applications," *J. Lightwave Technol.*, vol. 35, no. 4, pp. 824-835, Feb. 2017.
- [8] X. Yi, S. Chew, S. Song, L. Nguyen, and R. Minasian, "Integrated Microwave Photonics for Wideband Signal Processing," *Photonics*, vol. 4, no. 4, pp. 46, Nov. 2017.
- [9] W. Zhang and J. Yao, "Silicon-Based Integrated Microwave Photonics," *IEEE J. Quantum Elect.*, vol. 52, no. 1, pp. 0600412, Jun. 2016.
- [10] Q. Xu, B. Schmidt, S. Pradhan, and M. Lipson, "Micrometre-scale silicon electro-optic modulator," *Nature*, vol. 435, no. 7040, pp. 325-327, May 2005.
- [11] W. Liu, M. Li, R. S. Guzzon, E. J. Norberg, J. S. Parker, M. Lu, L. A. Coldren and J. Yao, "A fully reconfigurable photonic integrated signal processor," *Nature Photon.*, vol. 10, no. 3, pp. 190-195, Feb. 2016.
- [12] J. Capmany, D. Domenech, and P. Munoz, "Silicon graphene waveguide tunable broadband microwave photonics phase shifter," *Opt. Express*, vol. 22, no. 7, pp. 8094-8100, Apr. 2014.
- [13] M. Pu, L. Liu, W. Xue, Y. Ding, L. H. Frandsen, H. Ou, K. Yvind, and J. M. Hvam, "Widely tunable microwave phase shifter based on silicon-on-insulator dual-microring resonator," *Opt. Express*, vol. 18, no. 6, pp. 6172-6182, Mar. 2010.
- [14] X. Liu, C. Sun, B. Xiong, J. Wang, L. Wang, Y. Han, Z. Hao, H. Li, Y. Luo, J. Yan, T. Wei, Y. Zhang, and J. Wang, "Broadband tunable microwave photonic phase shifter with low RF power variation in a high-Q AlN microring," *Opt. Lett.*, vol. 41, no. 15, pp. 3599-3602, Aug. 2016.
- [15] M. Burla, D. Marpaung, L. Zhuang, C. Roeloffzen, M. R. Khan, A. Leinse, M. Hoekman, and R. Heideman, "On-chip CMOS compatible reconfigurable optical delay line with separate carrier tuning for microwave photonic signal processing," *Opt. Express*, vol. 19, no. 15, pp. 21475-21484, Aug. 2011.
- [16] D. G. Rabus, "Integrated Ring Resonators: The Compendium" *Springer Series in Optical Sciences*, no. 4, 2007.
- [17] W. Li, W. Wang, L. Wang, and N. Zhu, "Optical vector network analyzer based on single-sideband modulation and segmental measurement," *IEEE Photon. J.*, vol. 6, no. 2, pp. 1-8, Apr. 2014.
- [18] N. Ehteshami, W. Zhang, and J. Yao, "Optically tunable full 360° microwave photonic phase shifter using three cascaded silicon-on-insulator microring resonators," *Opt. Commun.*, vol. 373, pp. 53-58, Aug. 2016.